

Tailoring Nanoparticles and Quantum Dots for Practical Application

by

Leanne Arlene Milburn

A thesis submitted in partial fulfillment of the requirements for the degree of

**Master of Science**

Department of Chemistry  
**University of Alberta**

© Leanne Arlene Milburn, 2022

## Abstract

Throughout this thesis, methods for tailoring nanoparticles are broadly discussed and demonstrated experimentally. The main objective of this work was to help bridge the gap between fundamental materials science and global concerns by contributing to the development of *functional* nanomaterial systems. First, water-soluble silicon quantum dots were prepared and tested for their ability to detect nitroaromatic compounds in combination with a complementary fluorescent protein to improve the sensitivity of detection. A method for differentiating various nitroaromatic compounds was then targeted because nitro-based explosives and nerve agents both quench silicon quantum dot photoluminescence. This was achieved by introducing a second sensor consisting of a colourimetric enzymatic assay. In combination, the silicon quantum dot and enzymatic sensors yielded the intended outcome of detecting nitroaromatic compounds and providing a diagnosis of their inherent hazard class. Another study described within this thesis involved the preparation of water-soluble carbon nanodots surface-functionalized with redox-active molecules to yield a material that may find application in redox flow batteries. In addition to showing a robust electrochemical response, these amorphous carbon nanodots also display photoluminescence that could prove useful in tracking their movement within the battery.

## **Preface**

Part of this thesis represents a collaboration of ideas and experimentation. The project detailed in Chapter 2 was conceived by Dr. Christopher Jay T. Robidillo (under supervision of Prof. Jonathan Veinot) who performed preliminary experiments (data not shown). I performed all the experiments, data collection, and data processing of the results as presented. Dr. Rochelin Dalangin supplied the fluorescent proteins and assisted in protein quantification.

Chapter 3 is exclusively my original work however special thanks is given to Prof. Bernhard Rieger at the Technical University of Munich for the use of his laboratory space for the presented electrochemical work.

For the entirety of the thesis work, Prof. Jonathan G. C. Veinot was the supervisor and scientific advisor. He additionally assisted in the preparation of this thesis. The Analytical and Instrumentation Lab (Department of Chemistry, University of Alberta) is recognized for performing infrared spectroscopy of the samples presented in this work. The University of Alberta NanoFAB is recognized for its assistance with electron microscopy.

## Acknowledgments

The Natural Sciences and Engineering Research Council of Canada (NSERC) is thanked for providing the funding to support the research herein through a Canada Graduate Scholarships – Master’s program (CGS-M) scholarship. NSERC and the Alberta-Technical University of Munich (ATUMS) program are as well recognized for their sponsorship of the study abroad where research was performed at the Technical University of Munich.

Christopher Jay T. Robidillo is thanked for being my “sense-i” and giving me an entry point into the world of academic research. It was from my enjoyment in working with him as an undergraduate that I felt confident in pursuing graduate studies.

I have greatly enjoyed my time spent with the other Veinot group members, the many office laughs, advice, and outings together. Special thanks to I Teng (Emily) Cheong for braving Germany with me, as well as my friends at the TUM who provided such a wonderful experience.

It was through the enthusiasm of Prof. Jonathan G. C. Veinot (Jon) that I was inspired to pursue experiential learning opportunities during my last years of undergraduate schooling, leading me to view science as I do today. I will be forever grateful to him for encouraging me to make the most of every opportunity available to me, as well as for allowing me to carve my own path.

Last but certainly not least, I thank my family with much love. My parents, Cheryl and Terry, for supporting my academic path and giving me the security and freedom to dream and chase my passions. This has been the greatest gift, and I am lucky to have such open-minded parents. To my brother Eric, as well, for nurturing my interest in materials science with his own zeal for the field and demonstrating how good it feels to finally finish writing a Masters’ thesis.

## Table of Contents

<b>Chapter 1: An Introduction to Functional Nanoparticles</b>	<b>1</b>
1.1 A Historical View of Material Science	2
1.2 Properties of a Quantum Dot	4
1.2.1 Defining a Quantum Dot	4
1.2.2 Band Theory in Semiconductors.	4
1.2.3 Band Structure at the Nano-scale	9
1.2.4 Quantum Size Effects and Photoluminescence	9
1.3 Discovery and Development of Quantum Dots	10
1.3.1 Quantum Dots in Glass	10
1.3.2 Quantum Dots in Liquid	11
1.4 Methods of Tailoring Quantum Dots	11
1.4.1 Modifying QD Properties	11
1.4.1.1 Surface Modification	12
1.4.1.2 Doping	13
1.4.2 Material Choice & Sustainability Considerations	14
1.4.2.1 Toxicity	14
1.4.2.2 Renewable Resources	15
1.4.2.3 Life Cycle Analysis	15
1.4.2.4 Silicon and Carbon	15

1.5	Silicon Quantum Dots.	16
	1.5.1 Silicon Nanomaterials	16
	1.5.1.1 Porous Silicon.	16
	1.5.1.2 Silicon Quantum Dots.	16
	1.5.2 Tailoring and Applying Silicon Quantum Dots.	17
	1.5.2.1 Surface Modification of SiQDs	18
	1.5.2.2 Doping of SiQDs	18
1.6	“Carbon Quantum Dots”	20
	1.6.1 Evolution of Carbon Nanoparticles	20
	1.6.1.1 Fullerenes	20
	1.6.1.2 Graphene Quantum Dots	20
	1.6.1.3 Carbon Quantum Dots	21
	1.6.2 Tailoring and Applying Carbon Quantum Dots.	22
	1.6.2.1 Surface Modification of CQDs	22
	1.6.2.2 Doping of CQDs	23
1.7	Thesis Outline.	23
1.8	References	24
 <b>Chapter 2: Water-Soluble Silicon Quantum Dots as Nitroaromatics Sensors</b>		<b>31</b>
2.1	Introduction	32
2.2	Experimental Details	36
	2.2.1 Reagents and Materials	36
	2.2.2 Thermal Processing of HSQ	37

2.2.3	Preparation of Water-Soluble SiQDs	37
2.2.4	Ratiometric Detection of Explosives using SiQD and FP Mixtures	38
2.2.5	Calculations	39
2.2.6	Enzymatic Detection Assay (Solution and Gel-Encapsulation)	40
2.3	Results and Discussion	41
2.3.1	SiQD Photoluminescence Quenching Induced by NAEs	42
2.3.2	Selectivity Testing of the Enzymatic Acetylcholine Assay in Aqueous Solution	44
2.3.3	Enzymatic Assay Protected in Agarose Gel	45
2.4	Conclusions	48
2.5	References	48
2.6	Appendix	52
<b>Chapter 3: Tailoring Carbon Nanodots for Application to Redox Flow Batteries</b>		<b>53</b>
3.1	Introduction	54
3.2	Experimental Details	57
3.2.1	Reagents and Materials	57
3.2.2	Carbon Nanodot (CND) Synthesis	57
3.2.3	Carbon Nanodot Functionalization (CND@AQCA)	59
3.2.4	Materials Characterization	59
3.2.4.1	Transmission Electron Microscopy	59

3.2.4.2	Infrared Spectroscopy	.	.	.	.	.	.	59
3.2.4.3	X-ray Photoelectron Spectroscopy	.	.	.	.	.	.	60
3.2.4.4	Powder X-ray Diffraction Spectroscopy	.	.	.	.	.	.	60
3.2.4.5	Ultraviolet-Visible Spectroscopy	.	.	.	.	.	.	61
3.2.4.6	Photoluminescence Spectroscopy	.	.	.	.	.	.	61
3.2.5	Electrochemical Characterization	.	.	.	.	.	.	61
3.2.5.1	Cyclic Voltammetry	.	.	.	.	.	.	61
3.2.5.2	Cyclic Voltammetry – Kinetic Studies	.	.	.	.	.	.	62
3.3	Results and Discussion	.	.	.	.	.	.	63
3.3.1	Synthesis and Purification of CND and CND@AQCA	.	.	.	.	.	.	63
3.3.2	Physical and Structural Properties of CND and CND@AQCA	.	.	.	.	.	.	64
3.3.3	Photophysical Properties of the CNDs	.	.	.	.	.	.	69
3.3.4	Electrochemical Performance of CND@AQCA	.	.	.	.	.	.	72
3.3.4.1	Electrochemistry and Surface Attachment	.	.	.	.	.	.	72
3.3.4.2	Electrochemical Kinetics	.	.	.	.	.	.	73
3.3.4.2.1	Reversibility	.	.	.	.	.	.	74
3.3.4.2.2	Cycling Stability	.	.	.	.	.	.	78
3.4	Conclusions	.	.	.	.	.	.	79
3.5	References	.	.	.	.	.	.	80
3.6	Appendix	.	.	.	.	.	.	84

<b>Chapter 4: Conclusions and Future Work</b>	.	.	.	.	.	.	.	.	<b>86</b>
4.1 Thesis Conclusions	.	.	.	.	.	.	.	.	87
4.2 Future Directions	.	.	.	.	.	.	.	.	87
4.3 References	.	.	.	.	.	.	.	.	89
<b>Works Cited</b>	.	.	.	.	.	.	.	.	<b>90</b>

## List of Tables

**Table 1-1** Band gaps ( $E_g$ ) and exciton Bohr radii ( $a_{B,ex}$ ) of common material classes.

**Table 2-1** Calculated  $L_D$  values for the indicated quencher molecules. Analyses were performed for ratiometric sensors using mAmetrine1.2/SiQD and mCerulean3/SiQD combinations.

## List of Figures

- Figure 1-1** Simplified energy diagrams showing the effect of crystal growth on electronic structure, using silicon (Si) as an archetypal material. a) Atomic orbital diagram of the Si atom valence shell, b) molecular orbital diagram of a Si-Si bond, c) band structure formed in a Si quantum dot (SiQD), and d) the bulk Si band structure.  $\Delta E$  denotes a HOMO-LUMO gap and  $E_g$  is a band gap (the use of colour denotes non-equivalent energies). VB, CB, and  $E_F$  are the valence band, conduction band, and Fermi level, respectively.
- Figure 1-2** Energy band diagrams of the electronic classes of materials (conductor, semiconductor, and insulator). VB, CB,  $E_F$ , and  $E_g$  refer to the valence band, conduction band, Fermi level, and band gap, respectively.
- Figure 1-3** The effect of quantum dot particle size on the observed wavelength of photoluminescence in a hypothetical material. Starting from a size where the particle diameter ( $d$ ) is twice the exciton Bohr radius ( $a_{B,ex}$ ), decreasing the diameter results in quantum confinement and tuning of the band gap. The corresponding band structure and band gap ( $E_g$ ) are shown above.
- Figure 2-1** Representative photoluminescence (PL) quenching titration plots showing the dependence of the ratio of the photoluminescence intensities (i.e.,  $I_{FP}/I_{SiQD}$ ) upon excitation at 365 nm. Analyte titrations were performed with TNT (black), DNT (red), and NP (blue) for two ratiometric sensor FP/SiQD combinations: (a) mAmetrine ( $\lambda_{PL,max} = 525$  nm) and (b) mCerulean3 ( $\lambda_{PL,max} = 475$  nm)( $n=4$ ). (c) Photographs of the photoluminescence quenching response of the

mAmetrine/SiQD sensor to TNT exposure, using (i) an excitation source that selectively excites SiQDs, and (ii) a broadband UV source that excites the mAmetrine and SiQD luminophores.

**Figure 2-2** Solution-phase AChE inhibition trials for (a) PX and (b) TNT analytes. Inhibition is evidenced by an impairment of quinoneimine dye formation ( $\lambda_{\text{abs,max}} = 510 \text{ nm}$ ), as monitored over time. Measurements were performed in triplicate ( $n=3$ ), plotting the average and standard deviation.

**Figure 2-3** The gel-stabilized acetylcholine detection assay (a) expressed as the quinoneimine dye ( $\lambda_{\text{abs,max}} = 510 \text{ nm}$ ) formed over time ( $n=3$ ), (b) a visual representation of such, and (c) the absorption spectrum after 50 minutes of development. For triplicate results, the average and standard deviation were plotted.

**Figure 2-A1** Representative photoluminescence spectra of the fluorescent protein/silicon quantum dots sensing solutions, analyzed on the SpectraMax i3X spectrophotometer. a) mAmetrine ( $\lambda_{\text{em,max}} = 525 \text{ nm}$ ) and silicon quantum dots ( $\lambda_{\text{em,max}} = 665 \text{ nm}$ ). b) mCerulean3 ( $\lambda_{\text{em,max}} = 475 \text{ nm}$ ) and silicon quantum dots ( $\lambda_{\text{em,max}} = 665 \text{ nm}$ ).

**Figure 2-A2** Structural representations of the nitroaromatic molecules used in this work. Left to right: 2,4,6-trinitrotoluene (TNT), 2,4-dinitrotoluene (DNT), 4-nitrophenol (NP) and paraoxon (PX).

**Figure 3-1** Schematic of a redox flow battery.

**Figure 3-2** a) Bright-field transmission electron microscopy of bare carbon nanodots using an accelerating voltage of 20 eV. b) Average shifted histogram of measured particle size.

- Figure 3-3** Fourier transform infrared spectroscopy of carbon nanodot (CND) samples. a) The bare CNDs compared to the precursors used— citric acid (CA) and spermidine (SD). b) The bare CNDs with functional group assignment shown. c) Comparison of the bare CNDs to the same sample after surface functionalization with anthraquinone-2-carboxylic acid (AQCA). Bending is denoted by a subscript “b”.
- Figure 3-4** X-ray photoelectron spectroscopy of bare carbon nanodots (CNDs) and those functionalized with anthraquinone-2-carboxylic acid (CND@AQCA). a) Survey spectra and b) elemental composition. Fit high-resolution spectra of the C 1s and N 1s peaks for d) CNDs and e) CND@AQCA.
- Figure 3-5** Powder X-ray diffraction pattern of bare carbon nanodots after background subtraction.
- Figure 3-6** UV/Vis spectroscopic data obtained for aqueous solutions of bare carbon nanodots (CND) and those functionalized with anthraquinone-2-carboxylic acid (CND@AQCA). b) Excitation (ex) and emission (em) maxima for the same solutions. c) Variable excitation wavelength experiments for aqueous CND (c) and CND@AQCA (d) solutions.
- Figure 3-7** a) Cyclic voltammetry (CV) comparing carbon nanodots with (CND@AQCA) or without (CND) anthraquinone-2-carboxylic acid (AQCA) functionalization and a 1 M NaCl<sub>(aq)</sub> electrolyte blank (0.2 V/s scan rate. B) CV comparing CND@AQCA with a saturated AQCA solution physically mixed with bare CNDs (AQCA+CND), and a saturated AQCA solution (1 M NaCl<sub>(aq)</sub> electrolyte for all; 0.1 V/s scan rate).
- Figure 3-8** Cyclic voltammetry (CV) using variable scan rate ( $v$ ) to explore the electrochemical kinetics of carbon nanodots functionalized with anthraquinone-2-carboxylic acid

(CND@AQCA). a)  $v = 0.025 - 0.2$  V/s, b)  $v = 0.2 - 0.3$  V/s, c)  $v = 0.2 - 1.0$  V/s, d)  $1 - 40$  V/s.

**Figure 3-9** Cyclic voltammetry (CV) using variable scan rate ( $v$ ) to explore the electrochemical kinetics of anthraquinone-2-carboxylic acid (AQCA). a)  $v = 0.025 - 0.2$  V/s, b)  $v = 0.2 - 0.4$  V/s, c)  $v = 0.2 - 1.0$  V/s, d)  $1 - 40$  V/s.

**Figure 3-10** The peak anodic ( $i_a$ ) and cathodic ( $i_c$ ) currents measured for free anthraquinone (AQCA) and that bound to carbon nanodots (CND@AQCA). Showing magnitude as a function of the square root of scan rate ( $v$ ) (bottom), with an expansion of the linear region (top, inset).

**Figure 3-11** Cyclic voltammetry of anthraquinone-2-carboxylic acid functionalized carbon nanodots (in 1 M NaCl<sub>(aq)</sub>) run for a total of 250 cycles at 0.1 V/s. b) The peak anodic ( $i_a$ ) and cathodic ( $i_c$ ) currents plotted against cycle number.

**Figure 3-A1** Visual results before and after microwave reactor treatment of the reaction solution.

**Figure 3-A2** Dialysis setup used for purification of the CNDs and CND@AQCA.

**Figure 3-A3** Samples prepared for electrochemical analysis showing the appearance under ambient lighting as well as during exposure to a standard UV flashlight.

**Figure 3-A4** Electrode set-up derived for use with the PalmSens4 potentiostat. Showing the lead attachment (left) and the appearance of the Ag/AgCl reference, graphite counter, and graphite working electrodes (right).

## List of Schemes

- Scheme 2-1** a) Flow chart of the dual sensing platform presented in this work to differentiate nitroaromatic explosives (NAEs) and nerve agents (NANAs). b) Surface-functionalization of SiQDs for water-solubility. c) Assembly of the enzymatic assay involving acetylcholinesterase (AChE), choline oxidase (CO) and horseradish peroxidase (HRP). Presence of a NANA inhibits activity of AChE, preventing dye development.
- Scheme 3-1** A summary of the synthetic procedure targeting redox-active carbon nanodots and the mechanism of redox behaviour.

## List of Symbols, Nomenclature, and Abbreviations

B.C.E.	Before the Common Era
A.D.	Anno Domini
n	Nano ( $10^{-9}$ )
QD	Quantum dot
AO	Atomic orbital
MO	Molecular orbital
CB	Conduction band
VB	Valence band
LUMO	Lowest unoccupied molecular orbital
HOMO	Highest occupied molecular orbital
$E_g$	Band gap energy
eV	Electron volts
$E_F$	Fermi level
$\Delta E$	HOMO-LUMO energy difference
$a_{B,ex}$	Exciton Bohr radius
PL	Photoluminescence
d	Diameter
SiQD	Silicon quantum dot
GQD	Graphene quantum dot
CQD	Carbon quantum dot
CND	Carbon nanodot

CPD	Carbon polymer dot
°C	Degrees Celsius
NAC	Nitroaromatic compound
TNT	2,4,6-Trinitrotoluene
DNT	2,4-Dinitrotoluene
NP	Nitrophenol
PT	Parathion
PX	Paraoxon
HSQ	Hydrogen silsesquioxane
NAE	Nitroaromatic explosive
NANA	Nitroaromatic nerve agent
FP	Fluorescent protein
ACh	Acetylcholine
AChE	Acetylcholinesterase
CO	Choline oxidase
HRP	Horse radish peroxidase
HEPES	2-[4-(2-hydroxyethyl)piperazin-1-yl]ethanesulfonic acid
M <sub>w</sub>	Molecular weight
m	Milli (10 <sup>-3</sup> )
UV	Ultraviolet
MWCO	Molecular weight cut off (in Daltons)
K	Thousand
rpm	Rotations per minute

PEG	Polyethylene glycol
Milli-Q	Ultrapure
FTIR	Fourier transform infrared spectroscopy
XPS	X-ray photoelectron spectroscopy
TEM	Transmission electron microscopy
TGA	Thermogravimetric analysis
$\mu$	Micro ( $10^{-6}$ )
pH	Potential hydrogen
M	Molarity
$L_D$	Minimum detectable concentration
$\lambda$	Wavelength
ex	Excitation
RoA	Ratio of averages
SD	Standard deviation
Ave	Average
$\sigma_o$	Standard deviation of the blank
IUPAC	International Union of Pure and Applied Chemistry
$R^2$	Coefficient of determination
Max	Maximum
au	Arbitrary units
RFB	Redox flow battery
AQ	Anthraquinone
AQCA	Anthraquinone-2-carboxylic acid

NHS	N-hydroxysuccinimide
EDC•HCl	N-(3-dimethylaminopropyl)-N'-ethylcarbodiimide hydrochloride
mol	Mole
g	Gram
k	Kilo ( $10^3$ )
V	Volt
W	Watt
Å	Angstrom ( $10^{-10}$ )
PMMA	Polymethylmethacrylate
$\theta$	Theta (in degrees)
A	Amp
CV	Cyclic voltammetry
@	Core-shell
$\Delta E_p$	Peak-peak separation energy
$\text{cm}^{-1}$	Wavenumber
CA	Citric acid
SD	Spermidine
FWHM	Full width at half maximum
At %	Atomic percentage
PXRD	Powder X-ray diffraction
ex	Excitation
em	Emission
$E_{1/2}$	Half-wave potential

v	Scan rate
i	Current
a	Anodic
c	Cathodic
aq	Aqueous

## **Chapter 1:**

### **An Introduction to Functional Nanoparticles**

## 1.1 A Historical View of Material Science

The history of human civilization has long been defined by the technologies or, synonymously, the materials that reigned as advantageous to survival or economic development. In the Stone Age (2,000,000 – 8,000 years B.C.E.) the need for more plentiful food supplies incentivized the development of tools.<sup>1</sup> Accordingly, ancient humans utilized the available resources and fashioned tools out of rocks, bones, and animal tusks to gather, hunt, prepare food, and protect themselves. The discovery of flintstones, and the soon widespread availability of fire that came along with them, set the stage for a revolution that would allow humans to begin creating materials with unique properties, superior for applications compared to those present in the natural environment. This experimentation with natural materials is considered “alchemy”; an early form of the scientific method that we know and use today.<sup>2</sup> One of the first known examples of material enhancement involved the high-temperature heating of clay/soil mixtures to form hardened, heat-resistant ceramic materials.<sup>1</sup> Not only did these ceramics provide durable containers for cooking and storing food and drink, they also represent the birthplace of the field of ceramics which is active to the present day. In the eras that follow, passing through the Bronze Age (3,150 B.C.E.), the Iron Age (1,200 B.C.E.), and the recent Silicon Age, attempts to understand and tune the properties of materials have allowed scientists to realize applications which give us light (light-emitting diodes), harness electricity (solar cells, piezoelectrics, batteries, supercapacitors), construct sturdy buildings (steel, laminates, composites), and diagnose maladies (sensors/biosensors), among others.<sup>1</sup>

Another example that will bring us closer to the topic at hand is the development of glasses. Glasses are produced in similar ways to ceramics, however, they require higher temperature processing to harden into non-porous, transparent, amorphous materials.<sup>2</sup> The ubiquitous materials we commonly refer to as glasses are based upon silicates (Si, O matrix) or aluminosilicates (Al,

Si, O matrix). Adding small amounts of other compounds during synthesis (a process called “doping”, which we will discuss later) allows the properties of the glass to be modified. For example, adding a boron source (e.g.,  $B_2O_3$ ) increases the thermal shock resistance of glasses used in kitchenware; Pyrex dishes are made of borosilicate glass.<sup>3</sup> As another example, adding transition metal oxides can impart the glass with vibrant colours, which can be seen in the stained-glass windows of churches proliferating from the 12<sup>th</sup> century.<sup>4</sup> Cobalt and iron complexes are perhaps the most common colouring agents. Nano-sized elemental clusters (nanoparticles) can also interact with incident light and thus produce a coloured glass when grown in or embedded into the molten material. The Lycurgus Cup, presumably dating back to the fourth century A.D., appears an opaque green if viewed with reflected light but becomes a rich cherry red when light is transmitted through.<sup>5</sup> The glass has been shown to contain suspended nanoparticles composed of gold and silver, which are responsible for its striking optical properties.

Though nanomaterial utilization can be viewed as having its origins hundreds of years ago, the study of nanomaterials (within the scientific paradigm) is much more recent; dating back to only the 1960s (beginning with silica nanoparticles).<sup>6</sup> Indeed, it was only in 1959 that the theoretical concept of functional, nanoscale technologies was introduced by Richard Feynman.<sup>7</sup> Nanomaterials (or nanostructured materials) are defined as those in which one or more dimensions are of the submicron length, typically less than 100 nm.<sup>8</sup> In this size regime, the material’s chemical and physical properties may change, owing to the fact that there are too many associated atoms to behave distinctly, while too few to behave as a bulk material. Nanomaterials, then, are viewed as being an intermediate between atomic and bulk systems. The phenomenon responsible for producing their unique properties will be discussed in the next section. This will be done

through the lens of one class of nanomaterial – the quantum dot (QD) – as these nanoparticles, and their applications, are the focal point for the remainder of this thesis.

## **1.2 Properties of Quantum Dots**

### ***1.2.1 Defining a Quantum Dot***

“Quantum dot” is a term originally coined for spherical, semiconductor nanoparticles with dimensions smaller than that of the exciton Bohr radius of the bulk material.<sup>9</sup> To understand the properties of quantum dots, it is useful to first consider the properties of bulk semiconductors and the corresponding impact of reducing their particle size to the nanoscale.

### ***1.2.2 Band Theory in Semiconductors***

The electronic properties of semiconductors are intermediate between those of insulators and metals. This can be understood in the context of differences in the band structures of these materials. A band structure emerges when a crystal of an intrinsic semiconductor that is composed of an increasing number of bonded atoms grows to eventually reach the limit of bulk dimensions. The atomic orbitals (AOs) of each pair of atoms interact to form bonding and antibonding molecular orbitals (MOs) (Figure 1-1. a, b).<sup>10</sup> As more atoms are added to the crystal, more MOs are integrated and these similar-energy MOs cluster together to form quasi-continuous energy bands (see Figure 1-1. c, d). It is important to note that the energy levels within a band are similar, not identical, due to the complex perturbations caused by the variable atomic environment experienced by each atom.<sup>11</sup> The highest-energy band formed is referred to as the conduction band (CB) and is empty; the second-highest energy band formed is the valence band (VB) and this is where the valence electrons reside.<sup>10</sup> If the CB and VB overlap, such that valence electrons can

freely access the CB the material is a conductor (Figure 1-2). In the case of a semiconductor, the CB and VB are separated by a small energy difference, the band gap ( $E_g$ ), whereby energy is required to provide substantial access of valence electrons to the CB. An insulator, on the other hand, has an  $E_g$  that is large enough that the thermal energy required to increase electron mobility would compromise the physical stability of the crystal ( $> 3$  or  $4$  eV). Representative  $E_g$  values for each class, including common semiconductors, are shown in Table 1-1. In a pure crystalline material, the Fermi level ( $E_F$ ), which is the energy up to which electrons would reside if the  $E_g$  was not energetically forbidden, lies approximately halfway between the CB and VB (dependent on temperature, among other factors).<sup>8,12</sup>

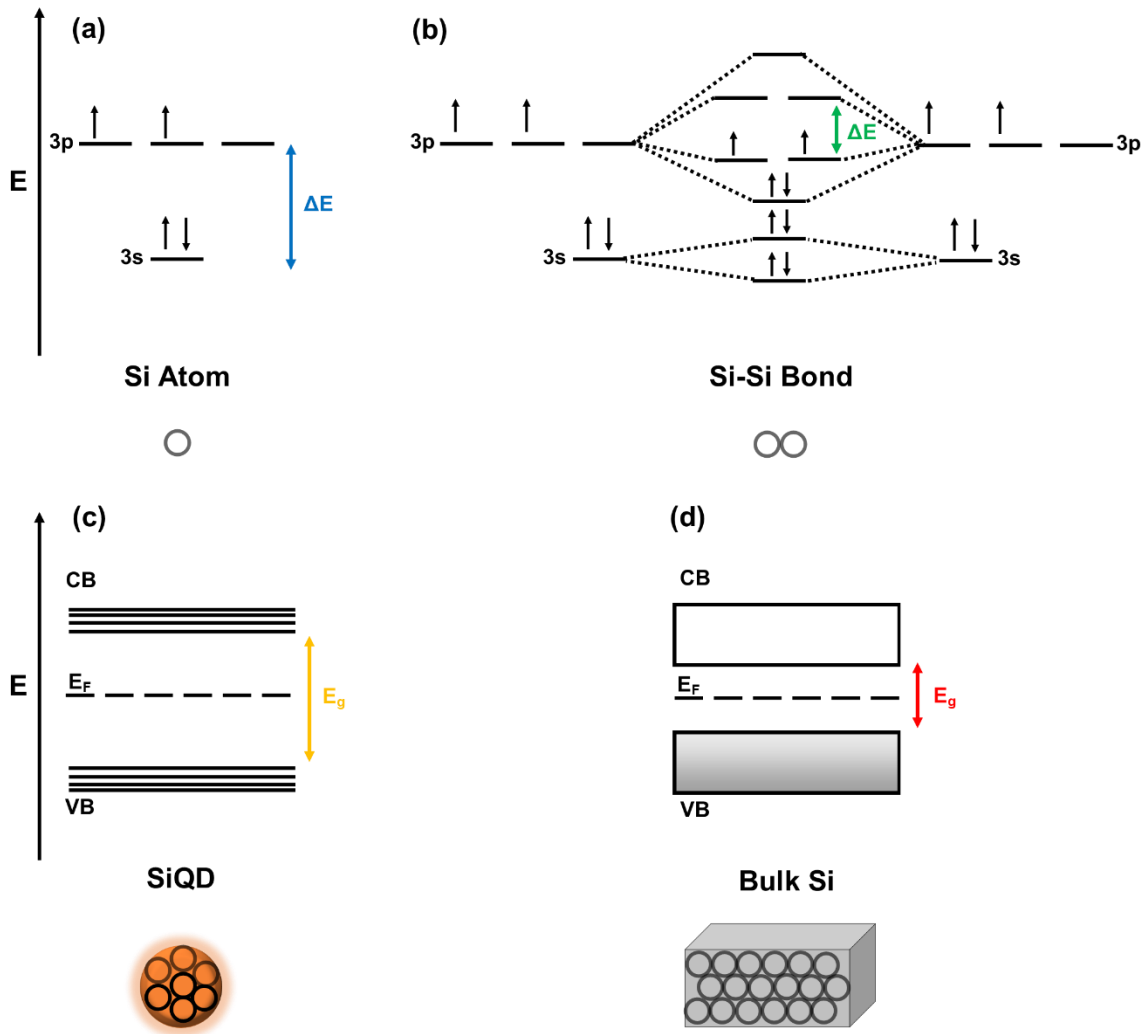


**Figure 1-1.** Simplified energy diagrams showing the effect of crystal growth on electronic structure, using silicon (Si) as an archetypal material. a) Atomic orbital diagram of the Si atom valence shell, b) molecular orbital diagram of a Si-Si bond, c) band structure formed in a Si quantum dot (SiQD), and d) the bulk Si band structure.  $\Delta E$  denotes a HOMO-LUMO gap and  $E_g$  is a band gap (the use of colour denotes non-equivalent energies). VB, CB, and  $E_F$  are the valence band, conduction band, and Fermi level, respectively.

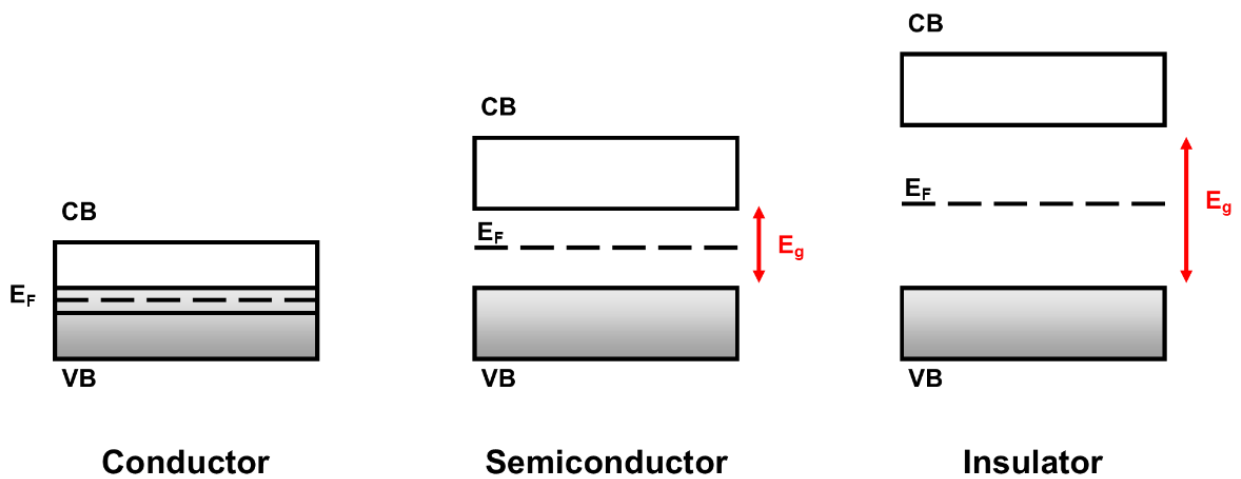


**Figure 1-2.** Energy band diagrams of the electronic classes of materials (conductor, semiconductor, and insulator). VB, CB,  $E_F$ , and  $E_g$  refer to the valence band, conduction band, Fermi level, and band gap, respectively.

**Table 1-1.** Band gaps ( $E_g$ ) and exciton Bohr radii ( $a_{B,ex}$ ) of common material classes.

<b><i>Material Class</i></b>	<b><i>Material</i></b>	<b><i><math>E_g</math> (eV)<sup>11,13,14</sup></i></b>	<b><i><math>a_{B,ex}</math> (nm)<sup>15</sup></i></b>
<i>Conductors</i>	Cu, Mg, Na, etc.	None	
<i>Intrinsic Semiconductors</i>	Si	1.12	3.88
<i>II-VI Semiconductors</i>	Ge	0.67	30.43
	CdS	2.41	1.50
	CdSe	1.74	7.07
	CdTe	1.52	7.14
	ZnS	3.50	2.16
<i>III-V Semiconductors</i>	AlP	2.45	4.62
	GaP	2.22	5.14
	InP	1.35	12.69
<i>IV-VI Semiconductors</i>	PbS	0.41	18.24
<i>Insulators</i>	C (diamond)	5.41	1.68

### ***1.2.3 Band Structure at the Nano-scale***

With a general understanding of the origin of energy bands in materials, it is somewhat intuitive that the  $E_g$  can be modulated by the number of atoms in a very small crystal. Viewed from the perspective of nanomaterials, this concept can be readily extended to using particle size of a QD to tailor  $E_g$ . In a comparatively small particle, there are fewer bonded atoms and fewer MOs, thereby “thinning” the CB and VB and widening the  $E_g$ . In a comparatively large particle, the added MOs “thicken” the bands to create a smaller  $E_g$ . The  $E_g$  dictates how the nanostructure interacts with light and defines material properties such optical as absorption and emission.

### ***1.2.4. Quantum Size Effects and Photoluminescence***

Although the  $E_g$  of a QD can be varied as described above, this does not explain how one might predict the size at which a semiconductor will display size-dependent characteristics. The exciton Bohr radius ( $a_{B,ex}$ ) describes the physical distance that an electron can be displaced from its original position, before coulombic attraction to the remaining positive vacancy (or hole) is lost.<sup>14</sup> In this context, excitons can be viewed as a quasiparticle comprising the negatively charged electron and the positively charged hole.<sup>14</sup> Typical  $a_{B,ex}$  for common semiconductors are summarized in Table 1-1. Quantum confinement effects occur when the particle size is reduced below the  $a_{B,ex}$  because under these conditions the size of the exciton is being spatially confined. This confinement increases the likelihood of excitation (i.e., increased oscillator strength).<sup>14</sup> Subsequently, the numerous relaxation events (recombination of electrons and holes) release a flux of photons bearing an energy equivalent to the  $E_g$  of the QD. This process is called photoluminescence (PL) and is readily observed under ambient conditions. Figure 1-3 provides a depiction of the qualitative relationship between QD size and the observed wavelength of PL.

Potential applications of these tiny luminescent semiconductor particles are vast and include use in light-emitting diodes, photodetectors, photovoltaics, biomedical probes and carriers, catalysis, environmental sensors, and battery technologies.<sup>9</sup> The latter two will be explored in more detail in subsequent chapters.

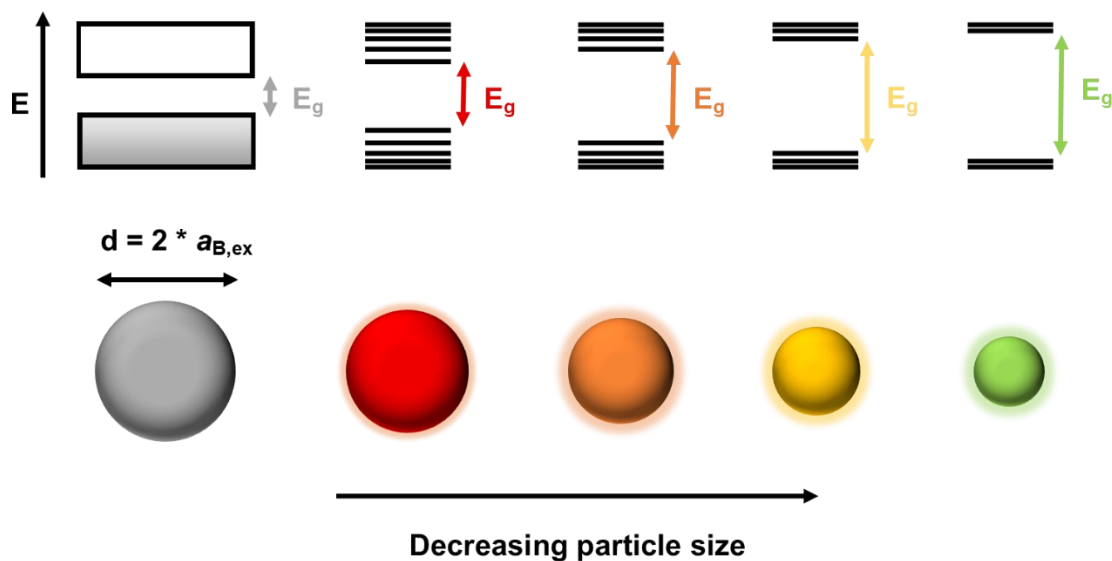


**Figure 1-3.** The effect of quantum dot particle size on the observed wavelength of photoluminescence in a hypothetical material. Starting from a size where the particle diameter ( $d$ ) is twice the exciton Bohr radius ( $a_{B,ex}$ ), decreasing the diameter results in quantum confinement and tuning of the band gap. The corresponding band structure and band gap ( $E_g$ ) are shown above.

## 1.3 Discovery and Development of Quantum Dots

### 1.3.1 Quantum Dots in Glass

With this foundational understanding of the origins of materials science and the fundamental properties of QDs, we now turn the focus of the present discussion to the discovery of QDs. We begin our story with the work of two scientists, Ekimov and Efros. Working at the Russian S. I. Vavilov State Institute and A. F. Ioffe Institute, they were exploring the effects of doping silicate glass with semiconductors.<sup>16</sup> To do this, glass precursors and semiconductor solids

were mixed and heat-treated.<sup>17,18</sup> Decomposition of the semiconductors led to diffusion-limited growth of particles yielding QDs embedded in a silicate glass. During the 1980s, these same researchers successfully demonstrated that CdS, CdSe, CuCl, and CuBr QDs could be grown in molten glass and that with prolonged heating progressively larger particles, eventually reaching bulk dimensions (recognizable by absorbance spectroscopy), were realized.<sup>17</sup>

### ***1.3.2 Quantum Dots in Liquids***

Transitioning away from glass-embedded quantum dots, around the same time period Brus was exploring the behaviour of semiconductor particles suspended in a liquid phase at the American Bell Laboratories.<sup>16</sup> During CdS particle synthesis, he observed size-dependent changes in the absorption spectrum of the colloidal material equivalent to those noted previously for glass-embedded systems. He also noted sized-dependent photoluminescence, using a synthesis developed by Grätzle and coworkers.<sup>20,21</sup> Brus went on to characterize this phenomenon for quantum dots composed of CdSe, ZnS, ZnSe, and PbS. Over time, Brus noted that the apparent particle size of his solvent-borne quantum dots would increase, an observation he attributed to the thermodynamic instability of the colloid, resulting in particle agglomeration.<sup>22</sup> The mechanism of this instability and ways to address it will be described shortly (see Section 1.4.1.1).

## **1.4 Methods of Tailoring Quantum Dots**

### ***1.4.1 Modifying QD Properties***

Properties of QDs that are commonly experimentally manipulated include the absorption and emission maxima, quantum yield or rate of radiative recombination,  $E_g$  or electron donor/acceptor abilities, and colloidal stability/particle solubility. While particle size has already

been noted as an essential parameter in defining the QD optical properties, surface modification and doping are two additional approaches commonly explored to modulate QD characteristics.

#### 1.4.1.1 Surface Modification

Owing to the exceptionally small dimensions of all nanoparticles (including QDs), a disproportionate number of atoms reside on the particle surface.<sup>14</sup> This high density of surface atoms leads to substantial surface reactivity that often necessitates a “capping agent” to be added to reaction mixtures to prevent particle agglomeration. The surface reactivity arises because surface atoms are less likely to have a fully satisfied valence shell owing to the restricted number of nearest neighbours.<sup>14</sup> These “unsatisfied” atoms possess “dangling bonds” which are the sites of heightened reactivity. Surface reconstruction has been observed – whereby the bonding geometries of surface atoms *internally* reorganize to achieve a full valence shell – however the lowest surface energy is achieved when a dangling bond is bonded to an *external* moiety and a near-ideal bonding geometry is preserved. This is the fundamental basis for surface functionalization (also known as surface passivation).

The motivations for functionalizing particles extend beyond preventing particle agglomeration to tailoring material properties of the QD. The aforementioned phenomenon of surface reconstruction yields new electronic states, interrupting the  $E_g$  of the particle and leading to loss (or diminishing) of their PL response.<sup>23</sup> For many applications it is also often desirable to work with QDs in a variety of solvents, with various polarities. Attachment of solubilizing groups to the particle surface provides a straightforward way to tailor the solvent compatibility of QDs. Chemical approaches toward surface functionalization involve assessing the available chemical bonds at the particle surface and selecting a “ligand” with a compatible reactive group (along with an initiator, or forcing conditions, if necessary). It should be noted that surface modification is the

primary method employed in this thesis to tailor nanoparticle properties, although doping will also be discussed for completeness.

#### 1.4.1.2 Doping

When successfully achieved, doping a QD often provides a greater effect on material properties than what is observed for doping the bulk material owing to the already limited number of atoms within the QD.<sup>24</sup> However, the general effect of dopants on QD electronic and optical properties arising from modulation of the free energy carriers (electrons or holes) is independent of particle size. Such modifications result in a shift in the band gap or Fermi level of the material.

Doping involves introducing an “impurity” to a material with the intent of influencing the properties of the material in a specific way. As such, a common method for dopant selection is to choose atoms with a different number of valence electrons than the “host” material atoms.<sup>11</sup> When bonded to the host, the dopant will then have unbonded, free electrons or too few electrons to satisfy the host (viewed as free holes), respectively. In the former case, the free electrons occupy “donor” states which reside just below the CB of the host, effectively increasing the Fermi level. Oppositely, in the latter case, free holes create “acceptor” states near the VB, decreasing the Fermi level. The doped materials are classified as n-type (excess negative charge carriers) or p-type (excess positive charge carriers). As silicon is an *elemental* intrinsic semiconductor and its doping has been extensively studied because of its electronics applications, more detailed information on doping can be found in Section 1.5.2.2.

The thermodynamic stability of a perfectly ordered, pure crystal makes achieving a uniform distribution of dopant atoms non-trivial because the dopant atom is a high energy “point defect” site.<sup>24</sup> Regardless, there are two categories of doping strategies that are used today. Extrinsic doping involves modifying the QD from the outside, for example by subjecting it to a reductant,

electrochemical treatment or suitable surface modification.<sup>25</sup> Intrinsic doping attempts to modify the QD from the inside, either by supplying dopant atoms during particle nucleation/growth or letting dopants diffuse throughout the QD from a concentrated source (dopant core or external solution).<sup>25</sup> A more detailed discussion of doping is beyond the scope of this thesis and the reader is directed to recent topical reviews.<sup>26,27</sup>

### ***1.4.2 Material Choice & Sustainability Considerations***

Before discussing specific material classes of QDs, it is important to consider one additional factor that contributes to the rational design of nanomaterials and is relevant to the work described in this thesis. That is, considering the impact that our proposed materials will have on scientists, producers, consumers, patients, and the environment. The ever-growing field of “*green*” *sustainable chemistry* is dedicated to producing chemicals and materials with these considerations in mind. In light of the far-reaching applications of nanomaterials, it is important that their design must consider more than mere performance and look to safety and environmental sustainability.

#### **1.4.2.1 Toxicity**

Prototypical QDs (primarily CdS, CdSe, and CdTe) and the precursors used to prepare them are well known to pose toxicity risks.<sup>28,29</sup> While this issue can be somewhat mitigated by creating a benign shell around the QDs (e.g., a layer of ZnS), the best solution is to employ less problematic materials. Solvents also play a role in determining the risk associated with a synthesis. Certain solvents (especially organics, such as benzene) are known to be carcinogenic, so intentionally using smaller volumes and safer alternatives when possible are desirable.<sup>30</sup>

#### 1.4.2.2 Renewable Resources

Transitioning to a circular economy necessitates, in a best-case scenario the use of “waste” as a precursor to something else of value. For this reason, turning biomass waste (e.g., egg shells, leaves, fruit peels) into functional nanomaterials has become a popular synthetic strategy.<sup>30,31</sup> In instances where new precursor materials must be sourced, it is important to consider the sociopolitical and environmental impacts of obtaining them.

#### 1.4.2.3 Life Cycle Analysis

Life cycle analysis involves considering the beginning of your chemicals and materials, like we have just discussed, as well as where they will end up after having served their purpose. Failure to do this can lead to global challenges decades later as is well demonstrated by the current crisis of plastic pollution extending from the oceans to our bloodstreams. Research into biodegradable polymers, or those that can be triggered to degrade at their end of life, has exploded.<sup>32</sup>

#### 1.4.2.4 Silicon and Carbon

In the context of the sustainability considerations presented above, it should be noted that the two classes of QDs presented in this thesis (i.e., silicon- and carbon-based) were selected with improved sustainability in mind. Silicon and carbon are both considered to provide QDs with toxicity significantly less than traditional QDs.<sup>33-37</sup> They are also of high natural abundance around the globe (silicon and carbon are the most abundant element in the Earth’s crust and the biosphere, respectively, after oxygen).<sup>38,39</sup> While the presented syntheses could be improved (by reducing energy expenditure, limiting solvent volumes, creating a life cycle assessment, etc.), they are a step forward.

## 1.5 Silicon Quantum Dots

### 1.5.1 Silicon Nanomaterials

#### 1.5.1.1 Porous Silicon

The first documented, *photoluminescent* silicon nanomaterial was porous silicon, published in 1990 (though the structure itself was known as early as 1956).<sup>40,41</sup> Here, the electrochemical and chemical non-homogeneous etching of bulk silicon was pursued to yield an array of crystalline nanowires with diameters small enough to produce quantum confinement.<sup>40</sup> Since bulk silicon is intrinsically a poor emitter owing to its indirect  $E_g$ , harnessing quantum confinement was an essential development to increase the favourability of radiative recombination. Originally, it was thought that reducing the material dimensions to the nanoscale caused a shift to a direct  $E_g$ . Later, it was theorized that the enhanced PL was due to a reduced three-body Auger effect.<sup>23</sup> The uniformity and chemical stability of structures produced by this method were less than ideal to form a full physical understanding of nanostructured silicon.<sup>42</sup> Regardless, this seminal work demonstrated that bright PL was possible, paving the way for materials scientists to begin exploring freestanding silicon quantum dots (SiQDs).

#### 1.5.1.2 Silicon Quantum Dots

The earliest reports of freestanding (i.e., colloidal; suspended in a fluid) SiQDs involved gas-phase syntheses.<sup>43</sup> These methods were developed in an attempt to obtain monodisperse nanoparticles and support the study of the size-dependence of SiQDs optical properties.<sup>44</sup> In 1993 an arc-discharge synthesis yielded a SiQD aerosol (in a flowing argon stream) that was subsequently coupled with a radial differential mobility analyzer to select for SiQDs of narrow size distributions.<sup>44,45</sup> Around the same time, similar aerosols were also being produced by the high-temperature pyrolysis of disilane diluted in helium gas.<sup>46</sup> Exposure to oxygen gas resulted in

a thin SiO<sub>2</sub> layer forming on the SiQD surface. Varied precursor concentrations (controlled by flow rate to the furnace) and size-exclusion chromatography were used to select SiQD size, allowing quantum confinement to be confirmed as the underlying photoluminescence mechanism.<sup>47</sup> Other more recent studies have shown similar results.<sup>48,49</sup>

By 1999, solution-phase syntheses were being reported for growing nanoscale silicon crystals. Typical procedures involved a halogenated silane reacting with a reducing agent (e.g., alkali metal, hydride) under high temperatures and pressures.<sup>50</sup> A method for increasing the size control and monodispersity of the output SiQDs (inspired by other colloidal nanoparticle syntheses) was to incorporate a surfactant into the reaction mixture to template the nanostructures.<sup>51</sup> Size control can also be obtained using sol-gel techniques, where thermal processing solidifies molecular/polymeric silicon-based precursors into a silica matrix with nanocrystalline silicon inclusions.<sup>52,53</sup> In this method, size is controlled by the duration of heating, after which the silica is etched away to yield solution-processable SiQDs.

### ***1.5.2 Tailoring and Applying Silicon Quantum Dots***

Size is arguably the most important parameter in tailoring SiQDs for target applications because of its impact on optical properties. Reliable and tunable emission maxima are paramount for the use of SiQDs as emitters in light-emitting diodes, bioimaging probes, and more. Other parameters, though, expand the range of optical and physical properties and allow SiQDs to be manipulated in a variety of environments. The techniques discussed thus far for preparing SiQDs have primarily focused on the production of pure crystalline silicon (to study quantum confinement) which bears an oxide- or hydride-terminated surface. However, modifications to the bulk and/or the surface of the particle can be used to tailor SiQDs for various applications.

### 1.5.2.1 Surface Modification of SiQDs

As early as 1999, the tunability of the SiQD surface by post-synthetic reactions was being investigated. Much of this work drew inspiration from the seminal works involving porous silicon. For example, SiQDs synthesized by reaction of an alkali silicide and halogenated silanes could produce halogen-terminated SiQDs suitable for reaction with alkyllithium or Grignard reagents.<sup>54</sup> Depending on the nature of the transferred alkyl group, these reactions create a hydrophobic surface layer that imparts the SiQDs with favourable compatibility with organic solvents. Surface functionalization also protects against oxidation, increasing the chemical stability toward ambient conditions. Still, all syntheses and surface modification must be done in inert atmosphere to minimize the impact of oxidation. The nature of the surface groups also influences the observed emission from the SiQD, especially in the case of its oxidation.<sup>55</sup> Hydrogen-terminated SiQDs, such as those produced from sol-gel methods are commonly surface-functionalized with alkyl chains using an alkene precursor in a reaction called hydrosilylation.<sup>51</sup> This approach is very versatile in that molecules of various polarities may be located opposite the C=C bond. When biological applications are being targeted and water-solubility is preferred, alkenylamines, alkenylcarboxylic acids, or alkenylglycols can be used.<sup>56</sup> These surface groups provide hydrophilicity without adversely affecting particle  $E_g$  as can occur when placing electronegative atoms close to the SiQD core.<sup>55</sup> Water-soluble SiQDs are also important for applications such as sensing of water-soluble analytes, biomedicine, and semi-artificial photosynthesis, among others.<sup>57-59</sup>

### 1.5.2.2 Doping of SiQDs

Due to the wide-ranging utilization of doped bulk silicon in the electronics and renewable energy industries, there has been increasing interest in creating doped SiQDs.<sup>60</sup> Based on the

electronic configuration of silicon, which includes four valence electrons, common dopants include boron, aluminum, nitrogen, and phosphorous. The former two are considered p-type dopants as they have one less valence electron than silicon and thus form sites in the crystal that are *relatively* positively charged. Similarly, the latter two form *relatively* negatively charged sites owing to an extra valence electron and are known as n-type dopants. The excess of free charge carriers (holes and electrons, respectively) serves to increase the electrical conductivity of the material.<sup>61</sup>

One of the most interesting applications for doped SiQDs is that of photovoltaics, in which a p-n junction (a physical contact between p- and n-type doped material) is required for directional current flow upon photoexcitation.<sup>62,63</sup> Boron and phosphorous dopants can also be used to modify the absorption spectrum of SiQDs, with especial attention being paid to near- and mid-infrared absorption for potential application in sensing, laser radar transceivers, and alarm systems to name a few.<sup>64-66</sup> Co-doping with both an n- and p-type dopant can be used when both free holes and electrons are desired. For example, boron- and phosphorous-doped SiQDs formed by a sputtering and annealing approach have been applied to photocatalytic water splitting. It is postulated that the co-doped SiQDs display enhanced performance owing to oxidation resistance conferred by the (primarily surface-localized) dopant atoms.<sup>67</sup> Other elements have also been doped into SiQDs, such as iron or manganese to impart magnetism for use in biotherapeutics.<sup>68,69</sup>

## 1.6 “Carbon Quantum Dots”

### 1.6.1 Evolution of Carbon Nanoparticles

#### 1.6.1.1 Fullerenes

Perhaps the earliest synthetic example of a spherical carbon “nanoparticle” was Buckminsterfullerene – a hollow spherical molecule with sixty  $sp^2$  carbon atoms ( $C_{60}$ ) – which possesses a diameter of just over 0.7 nm.<sup>70</sup> The HOMO-LUMO energy gap is around 1.84 eV producing a notable PL after excitation.<sup>71</sup> It is important to note that the optical properties are governed exclusively by molecular energy levels and not by quantum confinement effects. Buckminsterfullerene exists in nature, however, it was discovered in 1985 by mass spectrometry of laser vaporized graphite and synthetic procedures were developed by 1990.<sup>72,73</sup> The pioneering work on fullerene structures by Curl, Kroto, and Smalley was later awarded the Nobel Prize in Chemistry, 1996. Other fullerenes are possible ( $C_n$ ,  $n = 36, 50, 70, 540$ , etc.), though stability is variable and depends on the symmetry and degree of bond angle strain.<sup>74</sup> The excitement generated from the discovery of fullerenes eventually lead to many other forms of carbon being explored, including carbon nanotubes, graphene, and variations of carbon nanoparticles as will be discussed below.

#### 1.6.1.2 Graphene Quantum Dots

Graphene, first isolated in 2004, is a two-dimensional arrangement of  $sp^2$  hybridized carbon atoms which form a highly electronically conductive and mechanically strong sheet.<sup>75</sup> The Nobel Prize in Physics, 2010, was attributed to Geim and Novoselov for their characterization of the unique properties possessed by graphene sheets. Graphene can be present as a single layer, multi-layer, or as an extended stacked structure, more commonly known as graphite. Graphene sheets, owing to their extended  $\pi$ -conjugated structure, lack a bandgap and are therefore not

photoluminescent materials.<sup>76</sup> However, similar to the manufacture of quantum confinement in semiconductor materials, photoluminescence can be obtained by reducing the sheet length to nanoscale dimensions or introducing defect states to electronically isolate sections of the sheet. Both cases yield what are referred to as “graphene quantum dots” (GQDs). The defects themselves may also give rise to photoluminescence, although the mechanisms of this are more complex.<sup>76</sup>

#### 1.6.1.3 Carbon Quantum Dots

Carbon quantum dots (CQDs) were also discovered in 2004, as a photoluminescent by-product of a carbon nanotube synthesis.<sup>77,78</sup> Similar to GQDs, it has been suggested that the photoluminescence of carbon quantum dots (CQDs) may be achieved through defect states at the surface of the particle, involving radiative recombination of trapped electrons and holes (though other theories exist, see below).<sup>76,79</sup> However, instead of the relatively flat geometry of GQDs (only a couple of graphene sheets thick at maximum), CQDs are spherical or pseudospherical particles.<sup>80</sup> The ideal CQD is highly crystallized into layered  $sp^2$  hybridized carbon domains.

If the degree of crystallinity in such a CQD is reduced so that the quantity of  $sp^3$  hybridized carbon (as well as heteroatom dopants) significantly impedes the ordering of  $sp^2$  hybridized domains, turbostratic carbon results. If the  $sp^3$  content is further increased, the particle takes on an amorphous character. In both cases, these particles are no longer considered as CQDs, as the PL properties are no longer easily attributed to the size of the particle, but rather as carbon nanodots (CNDs) or carbon polymer dots (CPDs), which are used synonymously within the literature.<sup>80</sup> For these structures, it is most plausible that embedded molecular fluorophores or other non-crystalline features are responsible for the observed PL. Note that “CND” is used in Chapter 3 to denote the demonstrated amorphous character of the synthesized nanoparticles.

It is worth clarifying that the PL mechanism of carbon nanoparticle systems is complex and still poorly understood. There are several theories- 1) quantum confinement, 2) embedded molecular fluorophores, and 3) surface states- to explain the PL and other optical properties (like excitation-dependent emission) observed.<sup>79</sup> For this reason, the term “carbon quantum dots” is used loosely, as they cannot be considered directly analogous to the semiconductor nanocrystals that we have been discussing previously (e.g., SiQDs) which are known to produce PL by quantum confinement.

### ***1.6.2 Tailoring and Applying Carbon Quantum Dots***

Though CQDs were discovered from “top-down” approaches to carbon nanomaterial generation (e.g., laser vaporization of bulk carbon), today the majority of research is done on “bottom-up” synthetic methods (e.g., hydrothermal processing of molecular precursors) which can easily tailor the CQD properties.<sup>79</sup>

#### **1.6.2.1 Surface Modification of CQDs**

CQDs produced from hydrothermal treatment of precursors at sufficiently high temperatures (>300 °C) are commonly described as core-shell structures where the core is sp<sup>2</sup> carbon and the shell is an sp<sup>3</sup> matrix with numerous hydrophilic functional groups.<sup>81</sup> This accounts for the high water-solubility of CQDs. The precursors chosen for synthesis will determine which surface functional groups are yielded; for example, citric acid/urea-derived CQDs will display carboxylic acid, hydroxyl, and amine groups, among others. As a result, amide coupling and esterification reactions are useful tools to covalently attach organic molecules to the CQD surface.<sup>82</sup> Non-covalent attachments (such as  $\pi$ -stacking with exposed sp<sup>2</sup> carbon domains) are

also possible and especially useful for applications, like drug delivery, where reversibility is desired.

#### 1.6.2.2 Doping of CQDs

Heteroatom doping is common in CQD preparations, primarily with the aim of increasing the PL quantum yield (the efficiency of photon emission).<sup>79</sup> This is commonly done by including an additional precursor in the reaction mixture or selecting a carbon source that already contains heteroatoms (e.g., cysteine for intrinsic nitrogen and sulfur doping). However, post-synthetic surface functionalization with heteroatom-bearing molecules is also possible. Nitrogen doping is a strategy well documented to increase the photoluminescence of CQDs.<sup>80,83,84</sup> It has also been shown that simultaneously incorporating an electron-rich dopant (nitrogen) and an electron-poor dopant (boron), relative to carbon, can further boost the quantum yield.<sup>85</sup> Less commonly, metallic dopants like manganese will be used. Improvements in the CQD optical properties are especially useful for applications such as bioimaging and chemical sensing where detection of PL (or change in PL) is necessary.

### 1.7 Thesis Outline

The present thesis describes the preparation of functionalized SiQDs and CNDs and their application to the fields of chemical sensing and energy storage, respectively. This work was undertaken with the aim of developing functional nanomaterial platforms to facilitate the connection between these fascinating materials and their benefit to pressing societal problems.

In the second chapter, chemical sensing using photoluminescence quenching of SiQDs by target analytes is discussed. We have explored the interaction between SiQDs and nitroaromatic explosives and nerve agents and developed a secondary enzymatic method for differentiating

between these molecules (which quench photoluminescence similarly). This two-fold detection system represents a portable sensor that may be used in airport security and remote environmental monitoring alike.

The third chapter relates to energy storage, specifically introducing the role of nanomaterials in redox flow batteries. It presents a developed method of hydrothermal synthesis of CNDs and post-synthetic functionalization for creation of an electrochemically active product, suitable as an aqueous electrolyte. As CNDs are still a relatively novel research area, extensive materials characterization has been recorded and discussed to promote an understanding of the obtained nanostructures. These efforts revealed that the obtained CNDs possess an amorphous structure with photoluminescence likely arising from embedded molecular fluorophores, and redox behaviour suitable for the intended application.

To conclude the thesis, the progress in driving tailored, functional nanomaterials towards practical application will be summarized and the prospective future directions for both projects will be discussed.

## 1.8 References:

- (1) Sass, S. L. *The Substance of Civilization: Materials and Human History from the Stone Age to the Age of Silicon*, 1<sup>st</sup> ed.; Arcade Publishing, Inc.; 1998.
- (2) Valiulis, A. V. *A History of Materials and Technologies Development*; VGTU Press TECHNIKA; 2014.
- (3) Smedskjaer, M. M.; Mauro, J. C.; Youngman, R. E.; Hogue, C. L.; Potuzak, M.; Yue, Y. Topological Principles of Borosilicate Glass Chemistry. *J. Phys. Chem. B* **2011**, *115*, 12930-12946. DOI: 10.1021/jp208796b
- (4) Capobianco, N.; Hunault, M. O. J. Y.; Balcon-Berry, S.; Galois, L.; Sandron, D.; Calas, G. The *Grande Rose* of the Reims Cathedral: An Eight-Century Perspective on the Colour Management of Medieval Stained Glass. *Sci. Rep.* **2019**, *9*, 3287. DOI: 10.1038/s41598-019-39740-y
- (5) Freestone, I.; Meeks, N.; Sax, M.; Higgitt, C. The Lycurgus Cup – A Roman Nanotechnology. *Gold Bull* **2007**, *40*, 270-277. DOI: 10.1007/BF03215599

- (6) Hochella, M. F.; Mogk, D. W.; Ranville, J.; Allen, I. C.; Luther, G. W.; Marr, L. C.; McGrail, B. P.; Murayama, M.; Qafoku, N. P.; Posso, K. M.; Sahai, N.; Schroeder, P. A.; Vikesland, P.; Westerhoff, P.; Yang, Y. Natural, Incidental, and Engineered Nanomaterials and their Impacts on the Earth system. *Science* **2019**, *363*, 1414. DOI: 10.1126/science.aau8299
- (7) Feynman, R. P. There's Plenty of Room at the Bottom. *Engineering and Science* **1960**, *23* (5), 22-36.
- (8) Schubert, U.; Hüsing, N. *Synthesis of Inorganic Materials*, 2<sup>nd</sup> ed.; Wiley-VCH Verlag GmbH & Co. KGaA, Weinheim; 2005.
- (9) Cotta, M. A. Quantum Dots and Their Applications: What Lies Ahead? *ACS Appl. Nano Mater.* **2020**, *3*, 4920-4924. DOI 10.1021/acsnano.0c01386
- (10) Mittemeijer, E. J. *Fundamentals of Materials Science: The Microstructure-Property Relationship Using Metals as Model Systems*, 2<sup>nd</sup> ed.; Springer Nature Switzerland AG; 2021.
- (11) Callister, W. D.; Rethwisch, D. G. *Materials Science and Engineering: An Introduction*. 9<sup>th</sup> ed.; John Wiley & Sons, Inc.; 2014.
- (12) Kahn, A. Fermi Level, Work Function and Vacuum Level. *Mater. Horiz.* **2016**, *3*, 7-10. DOI: 10.1039/C5MH00160A
- (13) Strehlow, W. H.; Cook, E. L. Compilation of Energy Band Gaps in Elemental and Binary Compound Semiconductors and Insulators. *J. Phys. Chem. Ref. Data* **1973**, *2*, 163. DOI: 10.1063/1.3253115
- (14) Cademartiri, L.; Ozin, G. A. *Concepts of Nanochemistry*. WILEY-VCH Verlag GmbH & Co. KGaA, Weinheim; 2009.
- (15) Geoffrion, L. D.; Guisbiers, G. Quantum Confinement: Size on the Grill! *J. Phys. Chem. Solids* **2020**, *140*, 109320. DOI: 10.1016/j.jpcs.2019.109320
- (16) Efros, A. L.; Brus, L. E. Nanocrystal Quantum Dots: From Discovery to Modern Development. *ACS Nano* **2021**, *15* (4), 6192-6210. DOI: 10.1021/acsnano.1c01399
- (17) Ekimov, A. I.; Efros, A. L.; Onushchenko, A. A. Quantum Size Effect in Semiconductor Microcrystals. *Solid State Commun.* **1985**, *56* (11), 921-924. DOI: 10.1016/S0038-1098(85)80025-9
- (18) Ekimov, A. Growth and Optical Properties of Semiconductor Nanocrystals in a Glassy Matrix. *J. Lumin.* **1996**, *70*, 1-20. DOI: 10.1016/0022-2313(96)00040-3
- (19) Kovalev, D.; Heckler, H.; Polisski, G.; Koch, F. Optical Properties of Si Nanocrystals. *Phys. Stat. Sol.* **1999**, *215*, 871. DOI: 10.1002/(SICI)1521-3951(199910)215:2<871::AID-PSSB871>3.0.CO;2-9
- (20) Rossetti, R.; Brus, L. Electron-Hole Recombination Emission as a Probe of Surface Chemistry in Aqueous CdS Colloids. *J. Phys. Chem.* **1982**, *86*, 4470-4472. DOI: 10.1021/j100220a003
- (21) Kalyanasundaram, K.; Borgarello, E.; Duonghong, D.; Grätzle, M. Cleavage of Water by Visible-Light Irradiation of Colloidal CdS Solutions; Inhibition of Photocorrosion by RuO<sub>2</sub>. *Angew. Chem. Int. Ed. Engl.* **1981**, *20*, 987-988. DOI: 10.1002/anie.198109871

- (22) Rossetti, R.; Nakahara, S.; Brus, L. E. Quantum Size Effects in the Redox Potentials, Resonance Raman Spectra, and Electronic Spectra of CdS Crystallites in Aqueous Solution. *J. Chem. Phys.* **1983**, *79* (2), 1086-1088. DOI: 10.1063/1.445834
- (23) Alivisatos, A. P. Semiconductor Clusters, Nanocrystals, and Quantum Dots. *Science* **1996**, *271*, 933-937. DOI: 10.1126/science.271.5251.933
- (24) Mocatta, D.; Cohen, G.; Schnattner, J.; Millo, O.; Rabani, E.; Banin, U. Heavily Doped Semiconductor Nanocrystal Quantum Dots. *Science* **2011**, *332*, 77-81. DOI: 10.1126/science.1196321
- (25) Makkar, M.; Viswanatha, R. Frontier Challenges in Doping Quantum Dots: Synthesis and Characterization. *RSC Adv.* **2018**, *8*, 22103-22112. DOI: 10.1039/C8RA03530J
- (26) Kou, X.; Jiang, S.; Park, S.-J.; Meng, L.-Y. A Review: Recent Advances in Preparations and Applications of Heteroatom-Doped Carbon Quantum Dots. *Dalton Trans* **2020**, *49*, 6915-6938. DOI: 10.1039/D0DT01004A
- (27) Oliva-Chatelain, B. L.; Ticich, T. M.; Barron, A. R. Doping Silicon Nanocrystals and Quantum Dots. *Nanoscale* **2016**, *8*, 1733-1745. DOI: 10.1039/C5NR04978D
- (28) Meier, M. A. R.; Tam, M. K. C. Shaping Effective Practices for Incorporating Sustainability Assessment in Manuscripts Submitted to *ACS Sustainable Chemistry & Engineering: Biomaterials*. *ACS Sustainable Chem. Eng.* **2021**, *9*, 7400-7042. DOI: 10.1021/acssuschemeng.1c03382
- (29) Derfus, A. M.; Chan, W. C. W.; Bhatia, S. N. Probing the Cytotoxicity of Semiconductor Quantum Dots. *Nano Letters* **2004**, *4* (1), 11-18. DOI: 10.1021/nl0347334
- (30) Murphy, C. J. Sustainability as an Emerging Design Criterion in Nanoparticle Synthesis and Applications. *J. Mater. Chem.* **2008**, *18*, 2173-2176. DOI: 10.1039/b717456j
- (31) Wareing, T. C.; Gentile, P.; Phan, A. N. Biomass-Based Carbon Dots: Current Development and Future Perspectives. *ACS Nano* **2021**, *15*, 15471-15501. DOI: 10.1021/acsnano.1c03886
- (32) Ashe, K. The Steps to Sustainability. *Nat. Chem.* **2022**, *14*, 243-244. DOI: 10.1038/s41557-022-00903-6
- (33) Bhattacharjee, S.; Rietjens, I. M. C. M.; Singh, M. P.; Atkins, T. M.; Purkait, T. K.; Xu, Z.; Regli, S.; Shukaiak, A.; Clark, R. J.; Mitchell, B. S.; Alink, G. M.; Marcelis, A. T. M.; Fink, M. J.; Veinot, J. G. C.; Kauzlarich, S. M.; Zuilhof, H. Cytotoxicity of Surface-Functionalized Silicon and Germanium Nanoparticles: The Dominant Role of Surface Charges. *Nanoscale* **2013**, *5*, 4870-4883. DOI: 10.1039/C3NR34266B
- (34) Kustov, L. M.; Mashkin, P. V.; Zakharov, V. N.; Abramenko, N. B.; Krysanov, E. Y.; Aslanov, L. A.; Peijnenburg, W. Silicon Nanoparticles: Characterization and Toxicity Studies. *Environ. Sci.: Nano* **2018**, *5*, 2945-2951. DOI: 10.1039/C8EN00934A
- (35) Cao, Z.; Peng, F.; Hu, Z.; Chu, B.; Zhong, Y.; Su, Y.; He, S.; He, Y. *In Vitro* Cellular Behaviours and Toxicity Assays of Small-Sized Fluorescent Silicon Nanoparticles. *Nanoscale* **2017**, *9*, 7602-7611. DOI: 10.1039/C7NR00530J

- (36) Wang, K.; Gao, Z.; Gao, G.; Wng, Y.; Shen, G.; Cui, D. Systematic Safety Evaluation on Photoluminescent Carbon Dots. *Nanoscale Res Lett* **2013**, *8*, 122. DOI: 10.1186/1556-276X-8-122
- (37) Havrdova, M.; Hola, K.; Skopalik, J.; Tomankova, K.; Petr, M.; Cepe, K.; Polakova, K.; Tucek, J.; Bourlinoe, A. B.; Zboril, R. Toxicity of Carbon Dots- Effect of Surface Functionalization on the Cell Viability, Reactive Oxygen Species Generation and Cell Cycle. *Carbon* **2016**, *99*, 238-248. DOI: 10.1016/j.carbon.2015.12.027
- (38) Titirici, M.-M.; White, R. J.; Brun, N.; Budarin, V. L.; Su, D. S.; del Monte, F.; Clark, J. H.; MacLachlan, M. J. Sustainable Carbon Materials. *Chem. Soc. Rev.* **2015**, *44*, 250-290. DOI: 10.1039/C4CS00232F
- (39) *Silicon*. <https://www.rsc.org/periodic-table/element/14/silicon> (accessed 2022-05-26)
- (40) Canham, L. T. Silicon Quantum Wire Array Fabrication by Electrochemical and Chemical Dissolution of Wafers. *Appl. Phys. Lett.* **1990**, *57*, 1046. DOI: 10.1063/1.103561
- (41) Uhlir, A. Electrolytic Shaping of Germanium and Silicon. *Bell Syst. Tech. J.* **1956**, *35*, 333. DOI: 10.1002/j.1538-7305.1956.tb02385.x
- (42) Dohnalová, K. ; Gregorkiewicz, T. ; Kúsová, K. Silicon Quantum Dots: Surface Matters. *J. Phys. : Condens. Matter* **2014**, *26*, 173201. DOI: 10.1088/0953-8984/26/17/173201
- (43) Heitmann, J.; Müller, F.; Zacharias, M.; Gösele, U. Silicon Nanocrystals : Size Matters. *Adv. Mater.* **2005**, *17*, 795-803. DOI: 10.1002/adma.200401126
- (44) Camata, R. P.; Atwater, H. A.; Vahala, K. J.; Flagan, R. C. Size Classification of Silicon Nanocrystals. *Appl. Phys. Lett.* **1996**, *68*, 3162. DOI: 10.1063/1.115811
- (45) Saunders, W. A.; Sercel, P. C.; Lee, R. B.; Atwater, H. A.; Vahala, K. J.; Flagan, R. C.; Escorcia-Aparcio, E. J. Synthesis of Luminescent Silicon Clusters by Spark Ablation. *Appl. Phys. Lett.* **1993**, *63*, 1549. DOI: 10.1063/1.110745
- (46) Littau, K. A.; Szajowski, P. J.; Muller, A. J.; Kortan, A. R.; Brus, L. E. A Luminescent Silicon Nanocrystal Colloid via a High-Temperature Aerosol Reaction. *J. Phys. Chem.* **1993**, *97*, 1224-1230. DOI : 10.1021/j100108a019
- (47) Wilson, W. L.; Szajowski, P. F.; Brus, L. E. Quantum Confinement in Size-Selected, Surface-Oxidized Silicon Nanocrystals. *Science* **1993**, *262*, 1242-1244. DOI: 10.1126/science.262.5137.1242
- (48) Ledoux, G.; Gong, J.; Huisken, F.; Guillois, O.; Reynaud, C. Photoluminescence of Size-Separated Silicon Nanocrystals : Confirmation of Quantum Confinement. *Appl. Phys. Lett.* **2002**, *80*, 4834. DOI: 10.1063/1.1485302
- (49) Huisken, F.; Ledoux, G.; Guillois, O.; Reynaud, C. Light-Emitting Silicon Nanocrystals from Laser Pyrolysis. *Adv. Mater.* **2002**, *14*, 1861-1865. DOI: 10.1002/adma.200290021
- (50) Heath, J. R. A Liquid-Solution-Phase Synthesis of Crystalline Silicon. *Science* **1999**, *258*, 1131-1133. DOI: 10.1126/science.258.5085.1131
- (51) McVey, B. F. P.; Tilley, R. D. Solution Synthesis, Optical Properties, and Bioimaging Applications of Silicon Nanocrystals. *Acc. Chem. Res.* **2014**, *47*, 3045-3051. DOI: 10.1021/ar500215v

- (52) Hessel, C. M.; Henderson, E. J.; Veinot, J. G. C. Hydrogen Silsesquioxane: A Molecular Precursor for Nanocrystalline Si–SiO<sub>2</sub> Composites and Freestanding Hydride-Surface-Terminated Silicon Nanoparticles. *Chem. Mater.* **2006**, *18*, 6139–6146. DOI: 10.1021/cm0602803
- (53) Henderson, E. J.; Kelly, J. A.; Veinot, J. G. C. Influence of HSiO<sub>1.5</sub> Sol–Gel Polymer Structure and Composition on the Size and Luminescent Properties of Silicon Nanocrystals. *Chem. Mater.* **2009**, *21*, 5426–5434. DOI: 10.1021/cm902028q
- (54) Yang, C.-S.; Bley, R. A.; Kauzlarich, S. M.; Lee, H. W. H.; Delgado, G. R. Synthesis of Alkyl-Terminated Silicon Nanoclusters by a Solution Route. *J. Am. Chem. Soc.* **1999**, *121* (22), 5191–5195. DOI: 10.1021/ja828509
- (55) Dasog, M.; Yang, Z.; Regli, S.; Atkins, T. M.; Faramus, A.; Singh, M. P.; Muthuswamy, E.; Kauzlarich, S. M.; Tilley, R. D.; Veinot, J. G. C. Chemical Insight into the Origin of Red and Blue Photoluminescence Arising from Freestanding Silicon Nanocrystals. *ACS Nano* **2013**, *7*, 2676–2685. DOI: 10.1021/nm4000644
- (56) Tilley, R. D.; Yamamoto, K. The Microemulsion Synthesis of Hydrophobic and Hydrophilic Silicon Nanocrystals. *Adv. Mater.* **2006**, *18*, 2053–2056. DOI: 10.1002/adma.200600118
- (57) Xu, X.; Ma, S.; Xiao, X.; Zhao, D. The Preparation of High-Quality Water-Soluble Silicon Quantum Dots and their Application in the Detection of Formaldehyde. *RSC Adv.* **2016**, *6*, 98899–98907. DOI: 10.1039/C6RA24654K
- (58) Özbilgin, I. N. G.; Yamazaki, T.; Watanabe, J.; Sun, H.-T.; Hanagata, N.; Shirahata, N. Water-Soluble Silicon Quantum Dots towards Fluorescence-Guided Photothermal Nanotherapy. *Langmuir* **2022**, *38* (17), 5188–5196. DOI: 10.1021/acs.langmuir.1c02326
- (59) Li, Y.; Li, W.; Zhang, H.; Liu, Y.; Ma, L.; Lei, B. Amplified Light Harvesting for Enhancing Italian Lettuce Photosynthesis using Water Soluble Silicon Quantum Dots as Artificial Antennas. *Nanoscale* **2020**, *12*, 155–166. DOI: 10.1039/C9NR08187A
- (60) Milliken, S.; Thiessen, A. N.; Cheong, I. T.; O’Connor, K. M.; Li, Z.; Hooper, R. W.; Robidillo, C. J. T.; Veinot, J. G. C. “Turning the Dials”: Controlling Synthesis, Structure, Composition, and Surface Chemistry to Tailor Silicon Nanoparticle Properties. *Nanoscale* **2021**, *13*, 16379–16404. DOI: 10.1039/D1NR04701A
- (61) Chan, T.-L.; Zhang, S. B.; Chelikowsky, J. R. An Effective One-Particle Theory for Formation Energies in Doping Si Nanostructures. *Appl. Phys. Lett.* **2011**, *98*, 133116. DOI: 10.1063/1.3571552
- (62) Borowik, Ł.; Nguyen-Tran, T.; Roca I Cabarrocas, P.; Mélin, T. Doped Semiconductor Nanocrystal Junctions. *J. Appl. Phys.* **2013**, *114*, 204305. DOI: 10.1063/1.4834516
- (63) Elbersen, R.; Vijselaar, W.; Tiggelaar, R. M.; Gardeniers, H.; Huskens, J. Fabrication and Doping Methods for Silicon Nano- and Micropillar Arrays for Solar-Cell Applications: A Review. *Adv. Mater.* **2015**, *27*, 6781–6796. DOI: 10.1002/pip.2726
- (64) Rowe, D. J.; Jeong, J. S.; Mkhoyan, K. A.; Kortshagen, U. R. Phosphorous-Doped Silicon Nanocrystals Exhibiting Mid-Infrared Localized Surface Plasmon Resonance. *Nano Lett.* **2013**, *13* (3), 1317–1322. DOI: 10.1021/nl4001184

- (65) Zhou, S.; Pi, X.; Ni, Z.; Jiang, Y.; Jin, C.; Delerue, C.; Yang, D.; Nozaki, T. Comparative Study on the Localized Surface Plasmon Resonance of Boron- and Phosphorous-Doped Silicon Nanocrystals. *ACS Nano* **2015**, *9* (1), 378-386. DOI: 10.1021/nn505416r
- (66) Soref, R. Mid-Infrared Photonics in Silicon and Germanium. *Nature Photon* **2010**, *4*, 495-497. DOI: 10.1038/nphoton.2010.171
- (67) Sugimoto, H.; Zhou, H.; Takada, M.; Fushimi, J.; Fujii, M. Visible-Light Driven Photocatalytic Hydrogen Generation by Water-Soluble All-Inorganic Core-Shell Silicon Quantum Dots. *J. Mater. Chem. A* **2020**, *8*, 15789-15794. DOI: 10.1039/D0TA01071E
- (68) Singh, M. P.; Atkins, T. M.; Muthuswamy, E.; Kamali, S.; Tu, C.; Louie, A. Y.; Kauzlarich, S. M. Development of Iron-Doped Silicon Nanoparticles As Bimodal Imaging Agents. *ACS Nano* **2012**, *6*, 5596–5604. DOI: 10.1021/nn301536n
- (69) Tu, C.; Ma, X.; Pantazis, P.; Kauzlarich, S. M.; Louie, A. Y. Paramagnetic, Silicon Quantum Dots for Magnetic Resonance and Two-Photon Imaging of Macrophages. *J. Am. Chem. Soc.* **2010**, *132*, 2016–2023. DOI: 10.1021/ja909303g
- (70) Obodovskiy, I. Chapter 27. Radiation-Chemical Nanotechnologies. In *Radiation: Fundamentals, Applications, Risks, and Safety*; Elsevier B. V., 2019.
- (71) Palewska, K. ; Sworakowski, J. ; Chojnacki, H. A Photoluminescence Study in Fullerenes: Total Luminescence Spectroscopy of C<sub>60</sub> and C<sub>70</sub>. *J. Phys. Chem.* **1993**, *97*, 12167-12172. DOI: 10.1021/j100149a011
- (72) Kroto, H. W. ; Heath, J. R. ; O'Brien, S. C. ; Curl, R. F. ; Smalley, R. E. C<sub>60</sub>: Buckminsterfullerene. *Nature* **1985**, *318*, 162-163. DOI : 10.1038/318162a0
- (73) Haufler, R. E.; Conceicao, J.; Chibante, L. P. F.; Chai, Y.; Byrne, N. E.; Flanagan, S.; Haley, M. M.; O'Brien, S. C.; Pan, C.; Xiao, Z.; Billups, W. E.; Ciufolini M. A.; Hauge, R. H.; Margrave, J. L.; Wilson, L. J.; Curl, R. F.; Smalley, R. E. Efficient Production of C<sub>60</sub> (Buckminsterfullerene), C<sub>60</sub>H<sub>36</sub>, and the Solvated Buckide Ion. *Phys. Chem.* **1990**, *94*, 8634-8636. DOI: 10.1021/j100387a005
- (74) Eletsii, A. V.; Smirnov, B. M. Fullerenes and Carbon Structures. *Phys.-Usp.* **1995**, *38*, 935. DOI: 10.1002/sml.202001295
- (75) Geim, A. K. Graphene: Status and Prospects. *Science* **2009**, *324* (5934), 1530-1534. DOI: 10.1126/science.1158877
- (76) Cao, L.; Mezziani, M. J.; Sahu, S.; Sun, Y.-P. Photoluminescence Properties of Graphene versus Other Carbon Nanomaterials. *Accounts of Chemical Research* **2013**, *46*(1), 171-180. DOI: 10.1021/ar300128j
- (77) Xu, X.; Ray, R.; Gu, Y.; Ploehn, H. J.; Gearheart, L.; Raker, K.; Scrivens, W. A. Electrophoretic Analysis and Purification of Fluorescent Single-Walled Carbon Nanotube Fragments. *J. Am. Chem. Soc.* **2004**, *126*, 12736-12737. DOI 10.1021/ja040082
- (78) Baig, N.; Kammakam, I.; Falath, W. Nanomaterials: A Review of Synthesis Methods, Properties, Recent Progress, and Challenges. *Mater. Adv.* **2021**, *2*, 1821-1871. DOI: 10.1039/D0MA00807A

- (79) Mintz, K. J.; Zhou, Y.; Leblanc, R. M. Recent Developments of Carbon Quantum Dots Regarding their Optical Properties, Photoluminescence Mechanism, and Core Structure. *Nanoscale* **2019**, *11*, 4634-4652. DOI: 10.1039/C8NR10059D
- (80) Feng, T.; Tao, S.; Yue, D.; Zeng, Q.; Chen, W.; Yang, B. Recent Advanced in Energy Conversion Application of Carbon Dots: From Optoelectronic Devices to Electrocatalysis. *Small* **2020**, *16*, 2001295. DOI: 10.1002/sml.202001295
- (81) Zhou, Y.; Mintz, K. J.; Sharma, S. K.; Leblanc, R. M. Carbon Dots: Diverse Preparation, Application, and Perspective in Surface Chemistry. *Langmuir* **2019**, *35*, 9115-9132. DOI: 10.1021/acs.langmuir.9b00595
- (82) Yan, F.; Jiang, Y.; Sun, X.; Bai, Z.; Zhang, Y.; Zhou, X. Surface Modification and Chemical Functionalization of Carbon Dots: A Review. *Microchimica Acta* **2018**, *185*, 424. DOI: 10.1007/s00604-018-2953-9
- (83) Yuan, Y. H.; Liu, Z. X.; Li, R. S.; Zou, H. Z.; Lin, M.; Liu, H.; Huang, C. Z. Synthesis of Nitrogen-Doping Carbon Dots with Different Photoluminescence Properties by Controlling the Surface States. *Nanoscale* **2016**, *8*, 6770-6776. DOI: 10.1039/C6NR00402C
- (84) Wang, J.; Zhang, P.; Huang, C.; Liu, G.; Leung, K. C.-F.; Wang, Y. X. J. High Performance Photoluminescent Carbon Dots for In Vitro and In Vivo Bioimaging: Effect of Nitrogen Doping Ratios. *Langmuir* **2015**, *31*, 8063-8073. DOI: 10.1021/acs.langmuir.5b01875
- (85) Choi, Y.; Kang, B.; Lee, J.; Kim, S.; Kim, G. T.; Kang, H.; Lee, B. R.; Kim, H.; Shim, S.-H.; Lee, G.; Kwon, O.-H.; Kim, B.-S. Integrative Approach toward Uncovering the Origin of Photoluminescence in Dual Heteroatom-Doped Carbon Nanodots. *Chem. Mater.* **2016**, *28* (19), 6840-6847. DOI: 10.1021/acs.chemmater.6b0171

## **Chapter 2:**

### **Water-Soluble Silicon Quantum Dots as Nitroaromatic Sensors**

## 2.1 Introduction

Nitroaromatic compounds (NACs) are molecules comprising at least one aromatic ring bearing at least one nitro (-NO<sub>2</sub>) group. They can be categorized into several classes of hazardous materials: many NACs are high energy materials (or explosives) – examples include 2,4,6-trinitrotoluene (TNT) and 2,4-dinitrotoluene (DNT) – others, like fenitrothion, parathion (PT) and paraoxon (PX) show adverse biological effects and act as nerve agents.<sup>1,2</sup> Beyond the obvious societal threats posed by explosives and nerve agents, these and other NACs are widespread pollutants and can be environmental hazards. For example, NACs can be carcinogens, cytotoxins, endocrine disruptors and/or reproductive toxins for a variety of organisms.<sup>3</sup> Complicating matters, NACs are generally resistant to degradation and accumulate in the environment which consequently increases the likelihood of harm to local populations.<sup>3</sup>

The potential risks noted above highlight the importance of developing cost-effective, sensitive, and selective sensors that differentiate between the different classes of NACs. While modern analytical instrumentation can identify molecular structures with precision, most are costly, lab-based systems that require extensive, specialized training to operate.<sup>4</sup> Small, portable sensors have emerged as an important research area because they can offer rapid, inexpensive, ‘in the field’ NAC detection.<sup>5</sup> Fluorescence-based, on/off sensors are attractive options that rely on energy (or electron) transfer between the active sensing media and the target analyte that results in a detectable modulation of the fluorescence intensity.<sup>6</sup> The electron-withdrawing nature of pendant NO<sub>2</sub> groups on aromatic structural units make NACs electron acceptors (i.e., oxidizing agents) that can predictably quench the photoemission from luminophores. Early work involving silicon nanomaterial-based photoluminescence sensors focused on porous silicon.<sup>7</sup> Sailor *et al.* demonstrated a vapor-phase porous silicon sensor for TNT, DNT and nitrobenzene that showed

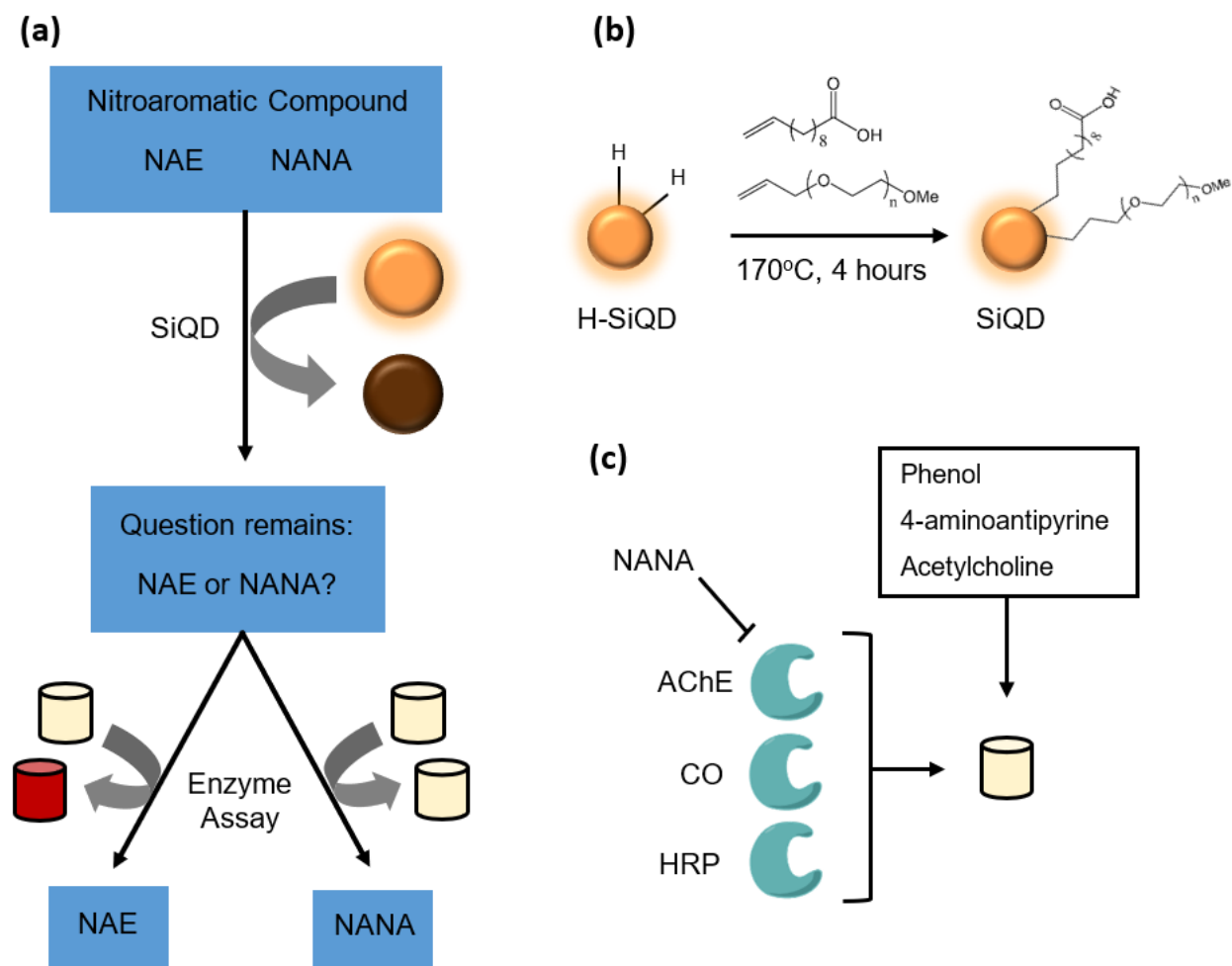
semi-reversible quenching.<sup>8</sup> Subsequently, Germanenko *et al.* demonstrated NAC quenching of isolated, unfunctionalized silicon nanocrystals, or silicon quantum dots (SiQDs), prepared using laser ablation.<sup>9</sup> Drawing on this and other foundational work involving porous silicon and SiQDs, we demonstrated that functionalized, *organic solvent-soluble* SiQDs obtained from thermally-induced disproportionation of hydrogen silsesquioxane (HSQ) provided probes for detecting nitroaromatic explosives (NAEs). Next, we showed that *water-soluble* SiQDs prepared similarly could detect nitroaromatic nerve agents (NANAs; PX and PT). In both cases, the luminescent SiQD probes were interfaced with standard filter paper to provide a convenient strip sensor platform.<sup>2,10</sup> In the case of the water-soluble SiQDs, we further extended our study by combining the SiQD photoluminescence response with the persistent (i.e., non-quenched) luminescence of fluorescent proteins (FPs) to afford a sensitive, ratiometric sensor.<sup>2</sup> To see the distinct photoluminescence peaks for the SiQDs and the FPs used in the present work, refer to Figure 2-A1 in the Appendix.

The obvious chemical similarities of NAEs and NANAs (Figure 2-A2, Appendix) make differentiating these hazardous chemical classes non-trivial as well as an important outstanding challenge. Typical approaches toward distinguishing these chemically similar molecules involve creating detection arrays comprised of complementary sensing species that are subsequently tested against the same analyte; this approach provides a ‘fingerprint’ used to identify specific analytes.<sup>11-13</sup> Such fingerprinting systems are often complicated and require computer processing infrastructure to evaluate output data. Herein, we demonstrate a sensing platform that differentiates NAEs from NANAs using straightforward visible inspection (Scheme 2-1a). To achieve this important advance, we have exploited the complementary virtues of materials chemistry and biochemistry and, simultaneously, expand the scope of our water-soluble SiQD/FP

sensor (see SiQD surface tailoring in Scheme 2-1b) by demonstrating NAE sensitivity. Subsequently, to distinguish NAEs from NANAs, we constructed a literature-inspired enzymatic acetylcholine detection assay that exploits the Trinder reaction to generate a readily detected red quinoneimine dye.<sup>14</sup>

Enzymes are highly specialized protein catalysts that exploit hydrogen-bonding as well as hydrophobic interactions at their active sites to engage targets with exceptionally high selectivity. In the past, enzymes have been combined and/or interfaced with nanomaterials to afford detection of microbes,<sup>15-17</sup> glucose,<sup>18,19</sup> and nerve agents.<sup>2, 20-22</sup> To our knowledge, no examples have demonstrated the capacity to differentiate closely related analytes like the noted subclasses of NACs (e.g., NAEs and NANAs). For our application, acetylcholinesterase was the enzyme of interest because it is inhibited by NANAs (Scheme 2-1c). This allowed us to devise an enzyme-based sensor for use alongside our SiQD/FP sensor— the combination of these two sensing motifs provides clear differentiation between NAEs and NANAs.

**Scheme 2-1.** a) Flow chart of the dual sensing platform presented in this work to differentiate nitroaromatic explosives (NAEs) and nerve agents (NANAs). b) Surface-functionalization of SiQDs for water-solubility. c) Assembly of the enzymatic assay involving acetylcholinesterase (AChE), choline oxidase (CO) and horseradish peroxidase (HRP). Presence of a NANA inhibits activity of AChE, preventing dye development.



## 2.2 Experimental Details

### 2.2.1 Reagents and Materials

The following reagents were obtained from the suppliers listed and used as received unless otherwise indicated. Hydrogen silsesquioxane (HSQ, in methyl isobutyl ketone; Fox-17, Dow Corning) and aqueous electronics grade hydrofluoric acid (HF, 49 %, J.T. Baker) were used for silicon quantum dot (SiQD) synthesis. 10-undecenoic acid ( $M_w = 184.28 \text{ g mol}^{-1}$ ,  $\rho = 0.912 \text{ g mL}^{-1}$ ) and allyloxy poly(ethylene oxide) methyl ester (9-12 units of ethylene oxide,  $M_w \sim 250 \text{ g mol}^{-1}$ ,  $\rho = 1.04 \text{ g mL}^{-1}$ , Gelest) were used for SiQD functionalization. mAmetrine and mCerulean3 (Campbell Group, University of Alberta), 4-(2-hydroxyethyl)-1-piperazineethanesulfonic acid (HEPES buffer; Millipore-Sigma) were added for the ratiometric SiQD/fluorescent protein (FP) sensor. 2,4,6-trinitrotoluene (TNT;  $M_w = 227.13 \text{ g mol}^{-1}$ , in acetonitrile; Millipore-Sigma), 2,4-dinitrotoluene (DNT;  $M_w = 182.13 \text{ g mol}^{-1}$ , in acetonitrile; Millipore-Sigma), 4-nitrophenol (NP;  $M_w = 139.11 \text{ g mol}^{-1}$ ; BDH) and paraoxon (Millipore-Sigma) were tested as analytes. Phenol ( $M_w = 94.11 \text{ g mol}^{-1}$ ), acetylcholine chloride ( $M_w = 181.66 \text{ g mol}^{-1}$ ), 4-aminoantipyrine ( $M_w = 203.24 \text{ g mol}^{-1}$ ), acetylcholinesterase from *Electrophorus electricus* (AChE; lyophilized powder, 222 U  $\text{mg}^{-1}$ ), choline oxidase from *Alcaligenes sp.* (CO; lyophilized powder, 10 U  $\text{mg}^{-1}$ ) and peroxidase from horseradish (HRP; lyophilized powder, 327 U  $\text{mg}^{-1}$ ) formed the enzymatic sensor. These materials (all from Millipore-Sigma) were dissolved in HEPES buffer (pH 7, 0.1 M) to the specified concentrations below. All solvents used were reagent grade.

### 2.2.2 Thermal Processing of HSQ

An oxide composite containing silicon nanodomains was prepared from HSQ using established literature procedures.<sup>23</sup> Briefly, HSQ powder was transferred to a quartz boat and heated in a standard tube furnace (1 h, 1100 °C, atmospheric composition: 5 % H<sub>2</sub> : 95 % Ar). After cooling to room temperature, the amber product obtained from the thermal processing step was annealed (1 h, 1200 °C) in flowing argon to provide a brown/black composite containing nanocrystalline silicon domains with approximate dimensions of 6 nm. Following mechanical grinding, the composite appeared light brown.

### 2.2.3 Preparation of Water-Soluble SiQDs

0.300 g of the 6 nm Si/SiO<sub>x</sub> composite was etched for 90 minutes in a mixture of 3 mL each 49 % HF, 100 % ethanol, and deionized water. **Caution!** *Hydrofluoric acid is highly corrosive and care should be taken to avoid skin contact or inhalation of vapours.* The resulting hydrogen-terminated SiQDs were extracted into ~10 mL of toluene which was transferred to test tubes and the solid was isolated upon centrifugation (3000 rpm, 10 minutes). Subsequently, activated molecular sieves were added (to remove trace water) and the SiQDs were resuspended in fresh toluene. After transferring the suspension of H-SiQDs to dry test tubes, the centrifugation was repeated, followed by decanting off the clear, colourless supernatant. The SiQDs were subsequently redispersed in 2 mL of 10-undecenoic acid, transferred to an Ar-filled Schlenk flask and 6 mL allyloxy poly(ethylene oxide) methyl ether was added. The reaction mixture was heated with stirring to 170 °C for 4 hours. At completion, the resultant transparent product mixture displayed characteristic red/orange photoluminescence upon exposure to a standard UV flashlight.

After cooling to room temperature, deionized water (10 mL) and hexanes (10 mL) were added and the mixture was transferred to a separatory funnel. After shaking, the organic layer was removed and discarded. 10 mL of fresh hexanes were added to the separatory funnel, the extraction repeated once more, and the aqueous phase transferred to dialysis tubing (12K MWCO). The aqueous solution was dialyzed twice each against 95% ethanol and deionized water (30 mins for each step) followed by four rounds of centrifugal ultrafiltration (30K MWCO filter, 5000 rpm, 30 mins each). Once the filtrate from the ultrafiltration was free of blue photoluminescence (arising from the PEG), upon exposure to UV light, the particles were resuspended in 2 mL of Milli-Q water. The resulting aqueous stock suspension of functionalized SiQDs showed characteristic red/orange photoluminescence upon excitation with a standard UV flashlight. The resulting functionalized SiQDs were characterized using FTIR, XPS, TEM, TGA, ultraviolet, and photoluminescence spectroscopy using standard methods. This data has been reported elsewhere.<sup>24</sup>

#### ***2.2.4 Ratiometric Detection of Explosives using SiQD and FP Mixtures***

The stock suspension of water-soluble SiQDs obtained from the synthesis/purification procedure was diluted with deionized water by 10 × (v:v). Tests were performed using a standard 96-well plate; each well was charged with 10 μL SiQDs (i.e., 2.54 mg Si/mL suspension), 10 μL of the FP solution of choice (i.e., mAmetrine<sup>25</sup> or mCerulean<sup>326</sup>; 0.405 μg mL<sup>-1</sup> stock solutions in 20 mM HEPES buffer, pH 7.0) and a predetermined quantity of target analyte (i.e., TNT, DNT, or NP), ranging from 2.5 - 40 μg mL<sup>-1</sup>. ***Caution!*** Nitroaromatics may be explosive, flammable, and damaging to human health. Store in a cool place away from ignition sources and work with low concentrations when possible. Analyte concentrations were subsequently converted to molarity to

allow for direct comparison. HEPES buffer (20 mM, pH 7.0) was added to each well to realize a total final volume of 100  $\mu$ L. Each experiment included a blank (no analyte), from which to calculate the  $L_D$ . All measurements were performed in quadruplicate. Photoluminescence spectra were acquired using a SpectraMax i3x ( $\lambda_{ex} = 365$  nm, scan range = 395 - 850 nm, 2 nm step size). The output was saved as a text file and subsequently processed in Microsoft Excel 2016. The fluorescence intensities ( $I_{SiQD}$  and  $I_{FP}$ ) corresponding to the photoluminescence maxima for the SiQDs ( $\lambda_{PL} = 665$  nm) and mAmetrine ( $\lambda_{PL} = 525$  nm) or mCerulean3 ( $\lambda_{PL} = 475$  nm) were selected for analysis. The ratiometric data were assembled using a ratio of averages (RoA) approach; averaging the quadruplicate data and taking the ratio ( $I_{FP}/I_{SiQD}$ ) of the averages for each concentration of analyte in question. The standard deviation was subsequently calculated using Equation 2-1. The ratiometric data were plotted in Origin 2021 and evaluated using linear regression. The  $L_D$  was calculated from the resulting linear equation using Equation 2-2.

### 2.2.5 Calculations

**Equation 2-1.** *Standard deviation of RoA, SD* = 
$$\sqrt{\left(\frac{SD_{I,FP}}{Ave_{I,FP}}\right)^2 + \left(\frac{SD_{I,SiQD}}{Ave_{I,SiQD}}\right)^2}$$

where:

$SD_{I,FP}$  = standard deviation of the photoluminescence intensity at FP emission maximum

$Ave_{I,FP}$  = average photoluminescence intensity at the FP emission maximum

$SD_{I,SiQD}$  = standard deviation of the photoluminescence intensity at the SiQD emission maximum

$Ave_{I,SiQD}$  = average photoluminescence intensity at the SiQD emission maximum

**Equation 2-2.**<sup>27</sup> IUPAC minimum detectable concentration,  $L_D = \frac{3.29\sigma_0}{A}$

where:

$\sigma_0$  = standard deviation of the blank

A = slope of the titration curve,  $F(x) = B + Ax$

**Table 2-1.** Calculated  $L_D$  values for the indicated quencher molecules. Analyses were performed for ratiometric sensors using mAmetrine1.2/SiQD and mCerulean3/SiQD combinations.

	$L_D$ of Analyte Quencher ( $\mu\text{M}$ )	
	mAmetrine/SiQD	mCerulean3/SiQD
Target Analyte		
TNT	1.86	4.00
DNT	4.67	3.65
NP	64.2	10.6

### 2.2.6 Enzymatic Detection Assay (Solution and Gel-Encapsulation)

Agarose powder (0.04 g) and HEPES buffer (1.6 mL, 0.1 M, pH 7.0) were combined and stirred in a beaker followed by heating on a hot plate (~200 °C) to reach a rolling boil. The beaker was stirred again and transferred to a separate hot plate that was preheated to 50 °C. Once cooled to 50 °C, 4-aminoantipyrine (200  $\mu\text{L}$ , 85 mM), phenol (200  $\mu\text{L}$ , 440 mM), HRP (50  $\mu\text{L}$ , 665

U/mL), CO (100  $\mu$ L, 38.1 U/mL), and AChE (50  $\mu$ L, 1.57 U/mL) were added. After stirring thoroughly, 200  $\mu$ L of the gel mixture was pipetted into each well of a 96-well plate and cooled for  $\sim$ 10 minutes at 4  $^{\circ}$ C. Subsequently, 10  $\mu$ L aliquots (i.e., final concentration of 5  $\mu$ M) of analytes of interest (i.e., PX, TNT, DNT, NP) were placed onto the top of the gel and equilibrated for 5 minutes. Initial absorbance readings were acquired using a BioTek Epoch 2 after which, ACh (20  $\mu$ L, 5.4 mM) was added and measurements were taken at 5 minute intervals up to 30 minutes followed by every 10 minutes thereafter until a total time of 60 minutes elapsed. The experiments were performed in triplicate, with the results averaged and plotted in Origin 2021. Precise enzyme concentrations were determined using the Implen Nanophotometer P360.

## **2.3 Results and Discussion**

### ***2.3.1 SiQD Photoluminescence Quenching Induced by NAEs***

Evaluation of the SiQD/FP combinations in the presence of dilute NAE solutions (i.e., TNT, DNT and 4-nitrophenol (NP)) was performed using a Molecular Devices SpectraMaxi3x photoluminescence spectrometer (Figure 2-1). By evaluating the photoluminescence quenching of the mixtures, we determined that the SiQD photoluminescence decreases linearly with increasing TNT, DNT and NP concentrations. We also tracked quenching ratiometrically by evaluating the ratio of the SiQD and FP emissions (Figures 2-1a,b). As expected, the magnitude of the quenching response qualitatively correlates with the number of NO<sub>2</sub> functional groups bonded to the aromatic ring of the analyte. These results were independent of the FP used. A visual representation of the ratiometric quenching can be seen in Figure 2-1c. Using the linear plots and a standard IUPAC equation (Equation 2-2), the average detection limits ( $L_D$ ) for the NAE were determined to be 1.9,

3.7, and 10.6  $\mu\text{M}$  for TNT, DNT, and NP, respectively, depending on the SiQD/FP pairing (Table 2-1). The present  $L_D$  values are modest when compared with those achieved using other fluorescence quenching systems;<sup>28</sup> this performance has previously been attributed to limited interaction between the SiQD surface and the NAE analyte and its optimization is the subject of an ongoing investigation.<sup>29</sup>

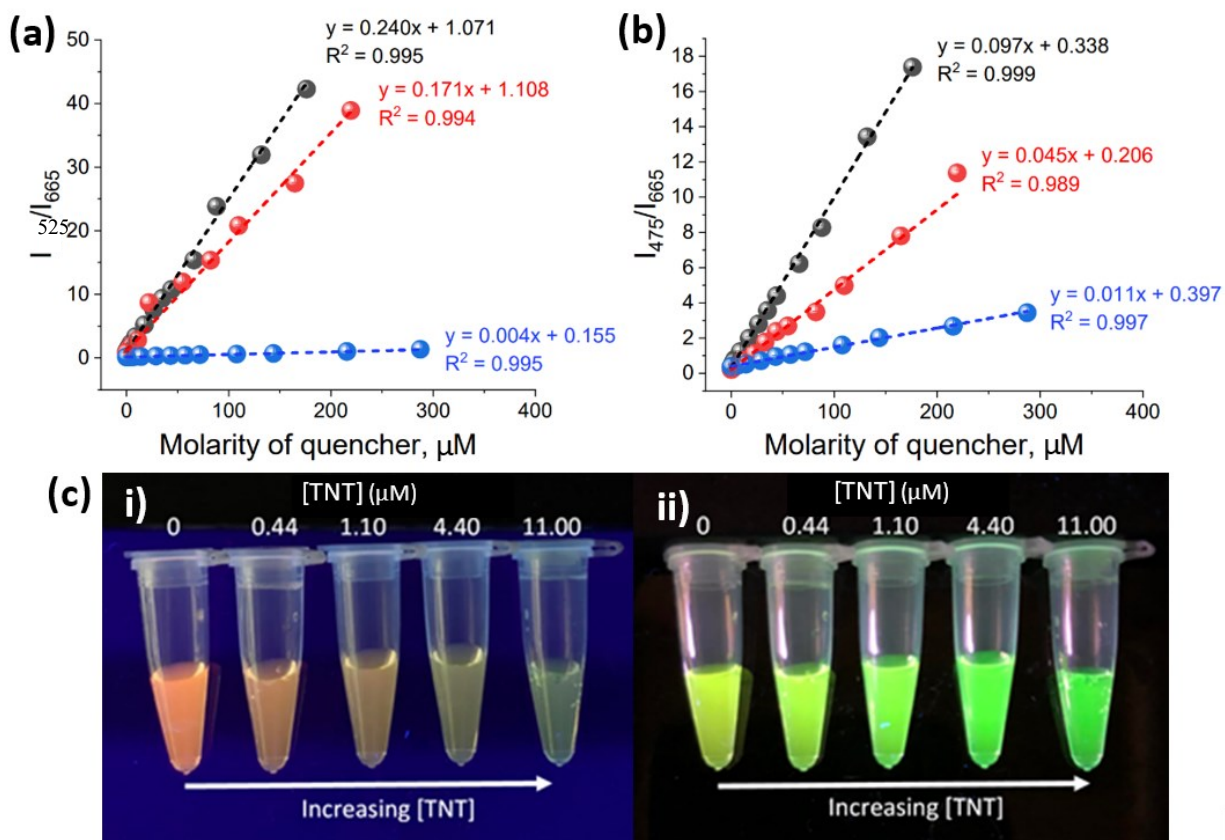


**Figure 2-1.** Representative photoluminescence (PL) quenching titration plots showing the dependence of the ratio of the photoluminescence intensities (i.e.,  $I_{\text{FP}}/I_{\text{SiQD}}$ ) upon excitation at 365 nm. Analyte titrations were performed with TNT (black), DNT (red), and NP (blue) for two ratiometric sensor FP/SiQD combinations: (a) mAmetrine ( $\lambda_{\text{PL,max}} = 525$  nm) and (b) mCerulean3 ( $\lambda_{\text{PL,max}} = 475$  nm)( $n=4$ ). (c) Photographs of the photoluminescence quenching response of the mAmetrine/SiQD sensor to TNT exposure, using (i) an excitation source that selectively excites SiQDs, and (ii) a broadband UV source that excites the mAmetrine and SiQD luminophores.

### 2.3.2 Selectivity Testing of the Enzymatic Acetylcholine Assay in Aqueous Solution

Having demonstrated that the  $L_D$  of NAEs was consistent with that previously reported for NANAs using the *same* SiQD/FP system ( $4.9 \mu\text{M}$  for PX),<sup>2</sup> we sought to design and incorporate the NANA-specific enzymatic assay to provide a secondary test to differentiate unknown nitroaromatics. Constructing the acetylcholine detection assay (See Section 2.2.6 for details) in-solution verified that PX inhibited AChE activity and, thus, the formation of the red quinoneimine dye. In contrast, TNT did not influence AChE activity and the red quinoneimine dye formed. Clearly, visual detection of the appearance of the characteristic red colour of the dye provides differentiation of TNT from PX and, by extension, NAEs from NANAs. To gain insight into the rapidity with which NAEs and NANA can be detected and differentiated, quinoneimine dye development was temporally tracked in the presence of PX and TNT (Figure 2-2). We note that the AChE population utilized in the present study can be saturated at an analyte concentration of  $5 \mu\text{M}$  so this concentration was used for all subsequent trials (Figure 2-2a). In solution phase, the development time necessary to visually distinguish  $5 \mu\text{M}$  PX samples from the control (PX  $0 \mu\text{M}$ ) is 5 minutes. For context, this response time is approximately twice as fast as most recently reported colourimetric detection systems.<sup>30-32</sup> Of important note, and as expected, TNT did not show statistically significant inhibition (Figure 2-2b).

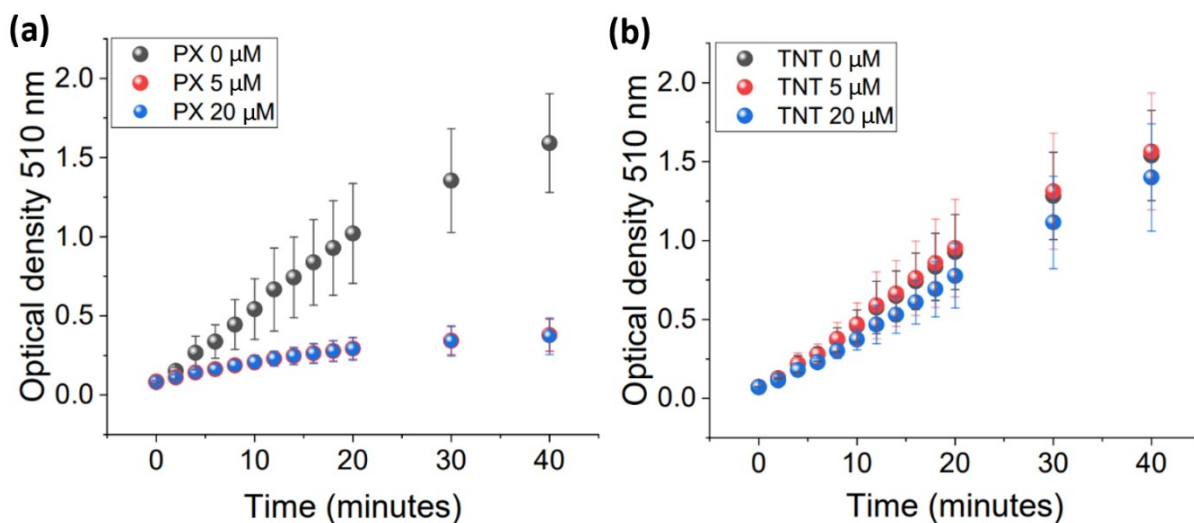


**Figure 2-2.** Solution-phase AChE inhibition trials for (a) PX and (b) TNT analytes. Inhibition is evidenced by an impairment of quinoneimine dye formation ( $\lambda_{\text{abs,max}} = 510 \text{ nm}$ ), as monitored over time. Measurements were performed in triplicate ( $n=3$ ), plotting the average and standard deviation.

### 2.3.3 Enzymatic Assay Protected in Agarose Gel

Recognizing the well-documented instability of enzymes under ambient conditions,<sup>33</sup> we chose to address this potential limitation by immobilizing the aforementioned enzymes in an agarose gel. Our data indicate that the performance of the AChE detection assay in an agarose gel is near-identical to its performance in solution. TNT, DNT and NP behaved similarly, having no effect on the quinoneimine dye development, while PX effectively inhibited dye formation (Figure 2-3a,b). Importantly, the absorption spectrum after gel development highlights the selectivity of our approach and confirms that the increase in absorption at 510 nm can be solely attributed to the formation of the quinoneimine dye (Figure 2-3c). The only notable difference from the solution-

based assay, which we attribute to the increased viscosity of the gel medium, is that gel-encapsulation slowed the dye development and extended the time necessary for visual differentiation of PX and TNT to approximately 10 minutes. Furthermore, the added stability provided by the gel scaffold increases the longevity and portability of the assay and is expected to facilitate effective field deployment.

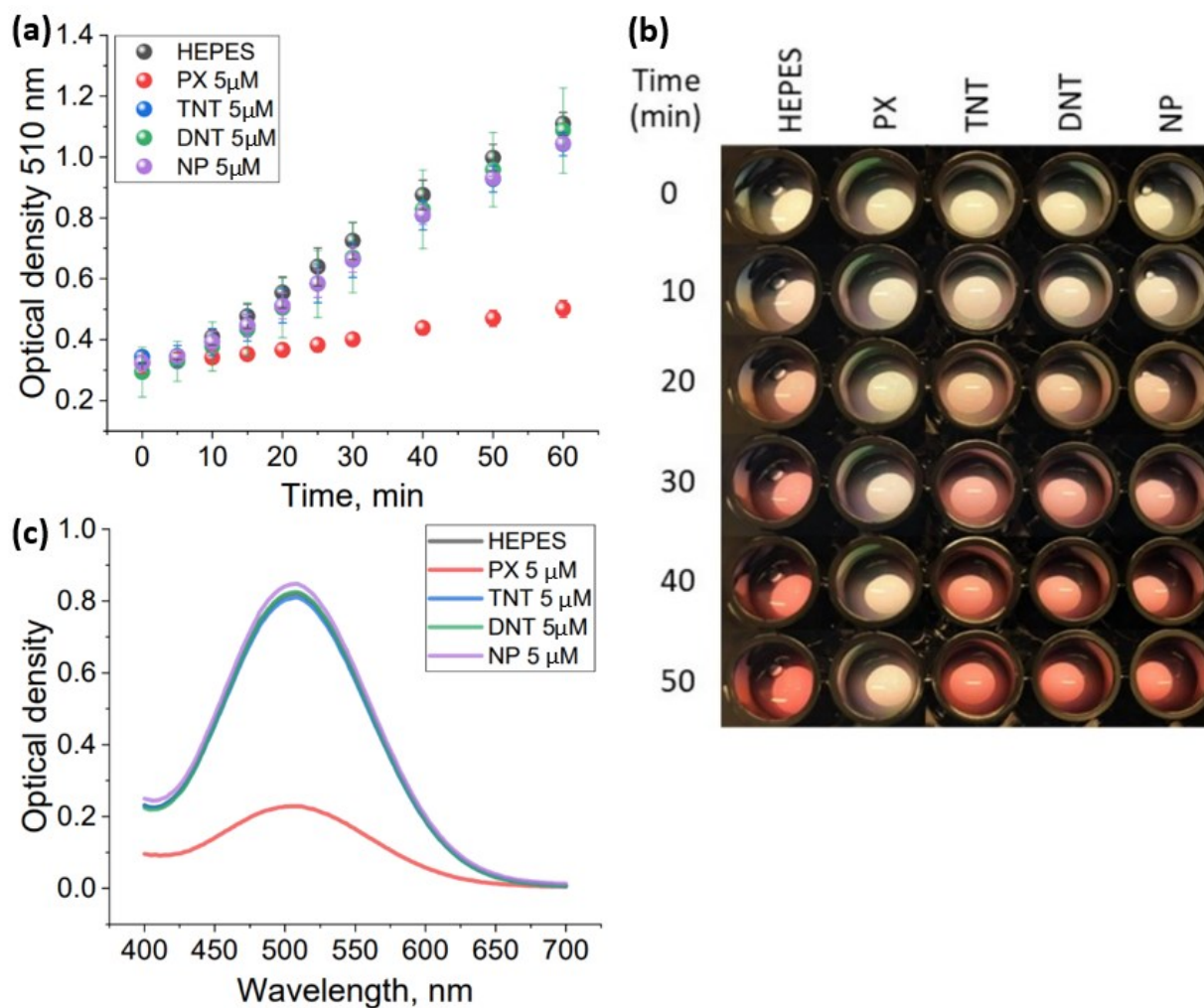


**Figure 2-3.** The gel-stabilized acetylcholine detection assay (a) expressed as the quinoneimine dye ( $\lambda_{\text{abs,max}} = 510 \text{ nm}$ ) formed over time ( $n=3$ ), (b) a visual representation of such, and (c) the absorption spectrum after 50 minutes of development. For triplicate results, the average and standard deviation were plotted.

## 2.4 Conclusions

To summarize, we have confirmed that our aqueous SiQD/FP photoluminescence-based sensor is sensitive to NAEs such as TNT, DNT and NP. Further, a secondary, colourimetric enzymatic assay was employed to obtain accurate and timely differentiation of hazardous nitroaromatic explosives from chemically similar nerve agents. The photoluminescent sensor responds immediately to indicate the presence of a nitroaromatic molecule and the colourimetric sensor provides a diagnosis of the hazard class (NAE or NANA) of the analyte within 5-10 minutes. This proof-of-concept work demonstrates the advantage introduced by combining sensing motifs from across disciplines— thus providing a portable sensing system capable of visually differentiating nitroaromatic molecules.

## 2.5 References

- (1) Tan, C.; Nasir, M. Z. M.; Ambrosi, A.; Pumera, M. 3D Printed Electrodes for Detection of Nitroaromatic Explosives and Nerve Agents. *Anal. Chem.* **2017**, *89* (17), 8995-9001. DOI: 10.1021/acs.analchem.7b01614
- (2) Robidillo, C. J. T.; Wandelt, S.; Dalangin, R.; Zhang, L.; Yu, H.; Meldrum, A.; Campbell, R. E.; Veinot, J. G. C. Ratiometric Detection of Nerve Agents by Coupling Complementary Properties of Silicon-Based Quantum Dots and Green Fluorescent Protein. *ACS Appl. Mater. Interfaces* **2019**, *11*, 33478-33488. DOI: 10.1021/acsami.9b10996
- (3) Tiwari, J.; Tarale, P.; Sivanesan, S.; Bafana, A. Environmental Persistence, Hazard, and Mitigation Challenges of Nitroaromatic Compounds. *Environ. Sci. Pollut. Res.* **2019**, *26*, 28650-28667. DOI: 10.1007/s11356-019-06043-8
- (4) Moore, D. S. Instrumentation for Trace Detection of High Explosives. *Rev. Sci. Instrum.* **2004**, *75*, 2499-2512. DOI: 10.1063/1.1771493
- (5) Germain, M. E.; Knapp, M. J. Optical Explosives Detection: From Color Changes to Fluorescence Turn-on. *Chem. Soc. Rev.* **2009**, *38*, 2543-2555. DOI: 10.1039/B809631G
- (6) Gonzalez, C. M.; Veinot, J. G. C. Silicon Nanocrystals for the Development of Sensing Platforms. *J. Mater. Chem. C* **2016**, *4*, 4863. DOI: 10.1039/C6TC01159D

- (7) Sailor, M. J.; Wu, E. C. Photoluminescence-Based Sensing with Porous Silicon Films, Microparticles, and Nanoparticles. *Adv. Funct. Mater.* **2009**, *19*, 3195-3208. DOI: 10.1002/adfm.200900535
- (8) Content, S.; Trogler, W. C.; Sailor, M. J. Detection of Nitrobenzene, DNT, and TNT Vapors by Quenching of Porous Silicon Photoluminescence. *Chem. - Eur. J.* **2000**, *6*, 2205-2213. DOI: 10.1002/1521-3765(20000616)6:12<2205::AID-CHEM2205>3.0.CO;2-A
- (9) Germanenko, I. N.; Li, S.; Samy El-Shall, M. Decay Dynamics and Quenching of Photoluminescence from Silicon Nanocrystals by Aromatic Nitro Compounds. *J. Phys. Chem. B* **2001**, *105*, 59-66. DOI: 10.1021/jp002340c
- (10) Gonzalez, C. M.; Iqbal, M.; Dasog, M.; Piercey, D. G.; Lockwood, R.; Klapoetke, T. M.; Veinot, J. G. C. Detection of High-Energy Compounds using Photoluminescent Silicon Nanocrystal Paper Based Sensors. *Nanoscale* **2014**, *6*, 2608-2612. DOI: 10.1039/C3NR06271F
- (11) Askim, J. R.; Mahmoudi, M.; Suslick, K. S. Optical Sensor Arrays for Chemical Sensing: The Optoelectronic Nose. *Chem. Soc. Rev.* **2013**, *42*, 8649. DOI: 10.1039/C3CS60179J
- (12) Hughes, A. D.; Glenn, I. C.; Patrick, A. D.; Ellington, A.; Anslyn, E. V. A Pattern Recognition Based Fluorescence Quenching Assay for the Detection and Identification of Explosive Analytes. *Chem. - Eur. J.* **2008**, *14*, 1822-1827. DOI: 10.1002/chem.200701546
- (13) Behera, P.; Mohanty, A.; De, M. Functionalized Fluorescent Nanodots for Discrimination of Nitroaromatic Compounds. *ACS Appl. Nano Mater.* **2020**, *3*, 2846-2856. DOI: 10.1021/acsanm.0c00132
- (14) Kang, H. R.; Kang, K. C.; Newby, J. G.; Lee, J. H. Fieldable Flow Injection Analysis System with 1,1'-oxalyldiimidazole Chemiluminescence Detection Capable of Quantifying Acetylcholine. *Anal. Methods* **2011**, *3*, 374-379. DOI: 10.1039/C0AY00440E
- (15) Miranda, O. R.; Li, X.; Garcia-Gonzalez, L.; Zhu, Z. J.; Bunz, U. H. F.; Rotello, V. M. Colorimetric Bacteria Sensing using a Supramolecular Enzyme-Nanoparticle Biosensor. *J. Am. Chem. Soc.* **2011**, *133* (25), 9650-9653. DOI: 10.1021/ja2021729
- (16) Chen, J.; Jiang, Z.; Ackerman, J. D.; Yazdani, M.; Hou, S.; Nugen, S. R.; Rotello, V. M. Electrochemical Nanoparticle-Enzyme Sensors for Screening Bacterial Contamination in Drinking Water. *Analyst* **2015**, *140*, 4991-4996. DOI: 10.1039/C5AN00637F
- (17) Duncan, B.; Le, N. D. B.; Alexander, C.; Gupta, A.; Tonga, G. Y.; Yazdani, M.; Landis, R. F.; Wang, L. S.; Yan, B.; Burmaoglu, S.; Li, X.; Rotello, V. M. Sensing by Smell: Nanoparticle-Enzyme Sensors for Rapid and Sensitive Detection of Bacteria with Olfactory Output. *ACS Nano* **2017**, *11*, 5339-5343. DOI: 10.021/acsnano.7b00822
- (18) Rossi, L. M.; Quach, A. D.; Rosenzweig, Z. Glucose Oxidase-Magnetite Nanoparticle Bioconjugate for Glucose Sensing. *Anal. Bioanal. Chem.* **2004**, *380*, 606-613. DOI: 10.1007/s00216-004-2770-3
- (19) Tian, K.; Siegel, G.; Tiwari, A. Enzymatic Glucose Sensor Based on Au Nanoparticle and Plant-Like ZnO Film Modified Electrode. *Mat. Sci. Eng. C* **2015**, *46*, 548-552. DOI: 10.1016/j.msec.2014.10.064

- (20) Pardo-Yissar, V.; Katz, E.; Wasserman, J.; Willner, I. Acetylcholine Esterase-Labeled CdS Nanoparticles on Electrodes: Photoelectrochemical Sensing of the Enzyme Inhibitors. *J. Am. Chem. Soc.* **2003**, *125* (3), 622-623. DOI: 10.1021/ja028922k
- (21) Simonian, A. L.; Good, T. A.; Wang, S. S.; Wild, J. R. Nanoparticle-Based Optical Biosensors for the Direct Detection of Organophosphate Chemical Warfare Agents and Pesticides. *Anal. Chim. Acta* **2005**, *534* (1), 69-77. DOI: 10.1016/j.aca.2004.06.056
- (22) Luckham, R. E.; Brennan, J. D. Bioactive Paper Dipstick Sensors for Acetylcholinesterase Inhibitors Based on Sol-gel/Enzyme/Gold Nanoparticle Composites. *Analyst* **2010**, *135*, 2028-2035. DOI: 10.1039/C0AN00283F
- (23) Clark, R. J.; Aghajamali, M.; Gonzalez, C. M.; Hadidi, L.; Islam, M. A.; Javadi, M.; Mobarok, M. H.; Purkait, T. K.; Robidillo, C. J. T.; Sinenikov, R.; Thiessen, A. N.; Washington, J.; Yu, H.; Veinot, J. G. C. From Hydrogen Silsesquioxane to Functionalized Silicon Nanocrystals. *Chem. Mater.* **2017**, *29*, 80-89. DOI: 10.1021/acs.chemmater.6b02667
- (24) Robidillo, C. J. T.; Islam, M. A.; Aghajamali, M.; Faramus, A.; Sinenikov, R.; Zhang, X.; Boekhoven, J.; Veinot, J. G. C. Functional Bioinorganic Hybrids from Enzymes and Luminescent Silicon-Based Nanoparticles. *Langmuir* **2018**, *34*, 6556-6569. DOI: 10.1021/acs.langmuir.8b01119
- (25) Ding, Y.; Ai, H.-W.; Hoi, H.; Campbell, R. E. Förster Resonance Energy Transfer-Based Biosensors for Multiparameter Ratiometric Imaging of Ca<sup>2+</sup> Dynamics and Caspase-3 Activity in Single Cells. *Anal. Chem.* **2011**, *83* (24), 9687-9693. DOI: 10.1021/ac202595g
- (26) Markwardt, M. L.; Kremers, G.-J.; Kraft, C. A.; Ray, K.; Cranfill, P. J. C.; Wilson, K. A.; Day, R. N.; Wachter, R. M.; Davidson, M. W.; Rizzo, M. A. An Improved Cerulean Fluorescent Protein with Enhanced Brightness and Reduced Reversible Photoswitching. *PLoS ONE* **2011**, *6* (3), e17896. DOI: 10.1371/journal.pone.0017896
- (27) International Union of Pure and Applied Chemistry. Chapter 18.4.3.7: Detection and Quantification Capabilities. In *Compendium of Analytical Nomenclature, Definitive Rules 1997*, 4<sup>th</sup> ed.; Lengyel, T., Inczedy, J., Ure, A.M., Eds. [https://media.iupac.org/publications/analytical\\_compendium/](https://media.iupac.org/publications/analytical_compendium/) (accessed 07-02-2019)
- (28) Ban, R.; Zheng, F.; Zhang, J. A Highly Sensitive Fluorescence Assay for 2,4,6-Trinitrotoluene using Amine-Capped Silicon Quantum Dots as a Probe. *Anal. Methods* **2015**, *7*, 1732-1737. DOI: 10.1039/C4AY02729A
- (29) Zhang, L.; Han, Y.; Zhu, J.; Zhai, Y.; Dong, S. Simple and Sensitive Fluorescent and Electrochemical Trinitrotoluene Sensors Based on Aqueous Carbon Dots. *Anal. Chem.* **2015**, *87* (4), 2033-2036. DOI: 10.1021/ac5043686
- (30) Hu, T.; Sang, W.; Chen, K.; Gu, H.; Ni, Z.; Liu, S. Simple and Sensitive Colorimetric Detection of a Trace Amount of 2,4,6-Trinitrotoluene (TNT) with QD Multilayer-Modified Microchannel Assays. *Mater. Chem. Front.* **2019**, *3*, 193. DOI: 10.1039/C8QM00430G
- (31) Milligan, K.; Shand, N. C.; Graham, D.; Faulds, K. Detection of Multiple Nitroaromatic Explosives via Formation of a Janowsky Complex and SERS. *Anal. Chem.* **2020**, *92*, 3253-3261. DOI: 10.1021/acs.analchem.9b05062

(32) Xie, X.; Xu, W.; Liu, X. Improving Colorimetric Assays through Protein Enzyme-Assisted Gold Nanoparticle Amplification. *Acc. Chem. Rev.* **2012**, *45* (9), 1511-1520. DOI: 10.1021/ar300044j

(33) Chapman, R.; Stenzel, M. H. All Wrapped up: Stabilization of Enzymes within Single Enzyme Nanoparticles. *J. Am. Chem. Soc.* **2019**, *141* (7), 2754-2769. DOI: 10.1021/jacs.8b10338

## 2.6 Appendix

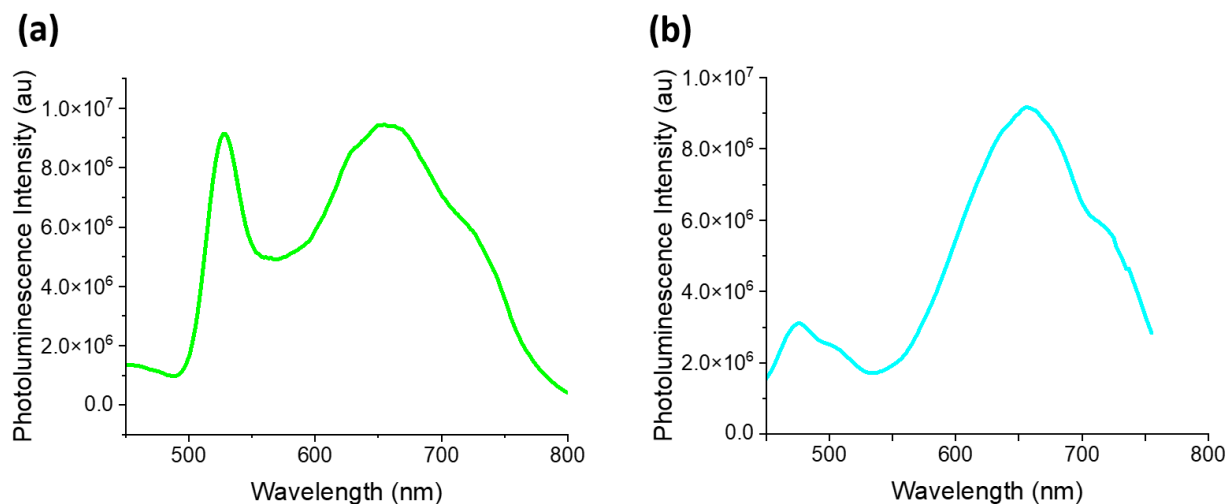


**Figure 2-A1.** Representative photoluminescence spectra of the fluorescent protein/silicon quantum dots sensing solutions, analyzed on the SpectraMax i3X spectrophotometer. a) mAmetrine ( $\lambda_{em,max} = 525$  nm) and silicon quantum dots ( $\lambda_{em,max} = 665$  nm). b) mCerulean3 ( $\lambda_{em,max} = 475$  nm) and silicon quantum dots ( $\lambda_{em,max} = 665$  nm).

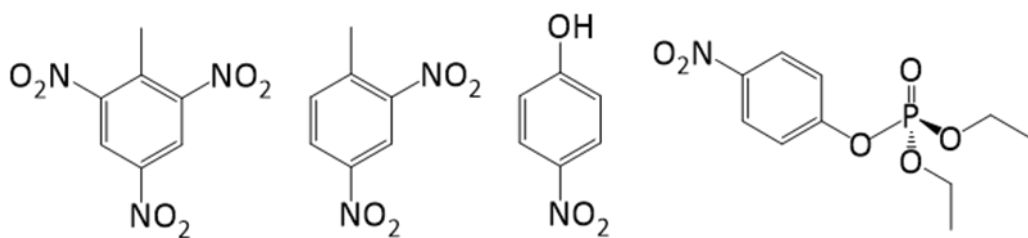


**Figure 2-A2.** Structural representations of the nitroaromatic molecules used in this work. Left to right: 2,4,6-trinitrotoluene (TNT), 2,4-dinitrotoluene (DNT), 4-nitrophenol (NP) and paraoxon (PX).

## **Chapter 3:**

### **Tailoring Carbon Nanodots for Application to Redox Flow Batteries**

### 3.1 Introduction

The scientific journalist Stephanie Pain put it perfectly when she said that “[t]he story of human progress – from nomadic hunter-gatherer to smartphone-wielding urbanite – is the story of energy”.<sup>1</sup> The drive of humankind for a continually increasing standard of living relies on our ability to turn the resources accessible to us into useable energy. This is demonstrated by the historical exploitation of coal, oil, and natural gas, however, consumption of these fossil fuels has polluted our Earth to the point of alarm.<sup>1</sup> The flourishing field of clean (non-fossil fuel) energy *production* technologies (e.g., solar cells) will not only help curb our impact on the Earth’s ecosystems but will improve global health by reducing inhalable pollution from fossil fuel burning.<sup>2</sup> Their potential, however, remains limited (e.g., by the intermittency of sunlight) without parallel advancement in energy *storage* technologies.

Battery technologies that are compatible with large- or “grid”-scale energy storage differ greatly from those used for consumer electronics and electric vehicles. They must be highly cost-efficient, have a reliable performance over very long lifetimes, and be derived from environmentally conscious abundant materials.<sup>3</sup> Redox flow batteries (RFBs) are a promising technology with the potential to address these considerations. They

embody a straightforward design: mobile liquid electrolytes performing redox chemistry at associated electrodes to generate electricity within an external circuit (Figure 3-1). The electrolytes – catholyte and anolyte – contain dissolved redox-active molecules that may be

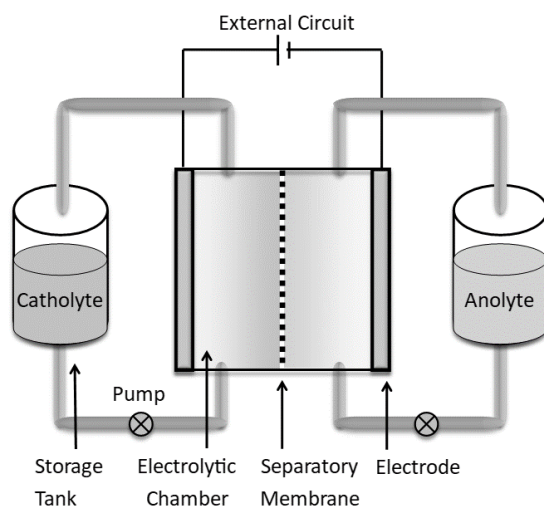


**Figure 3-1.** Schematic of a redox flow battery.

inorganic or organic. In recent years, the latter has been receiving attention due to the high availability, sustainability, and low cost of these materials.<sup>4</sup> A central issue in current RFB systems is the efficacy of the separatory membrane.<sup>5,6</sup> Highly selective membranes are cost-prohibitive while inexpensive membranes fail to prevent leaking of redox molecules (termed “species cross-over”) into the adjacent electrolyte chamber. This is undesirable as the catholyte and anolyte can react and lower the energy capacity of the RFB over time. To favour marketability, researchers have attached organic redox molecules to comparatively large polymer backbones/scaffolds to prevent their permeation through inexpensive membranes. Examples of this approach generally fall into three categories: redox-active oligomers,<sup>7,8</sup> redox-active polymers,<sup>9,10</sup> and redox-active cross-linked polymer nanoparticles.<sup>11,12</sup> Notably, surface-functionalized nanoparticles have not yet been introduced into this paradigm.

Carbon nanodots (CNDs) are pseudo-spherical, nanoscale particles primarily composed of carbon that are typically soluble in water owing to their abundant hydrogen-bonding surface functional groups. They offer ease of synthesis, tunable size, and display photoluminescence that can provide tracking of their localization in the RFB. They may also bypass some drawbacks of the aforementioned polymers, which increase the electrolyte viscosity through chain entanglement – slowing diffusion to the electrodes.<sup>10</sup> CNDs are synthesized using a variety of techniques including arc discharge, laser ablation, or electrochemical etching of a bulk carbon (top-down approaches), as well as pyrolysis, hydrothermal treatment, and templated methods (bottom-up approaches).<sup>13</sup> Importantly, these syntheses include inexpensive precursors and methods, and yield CNDs that are environmentally benign and even biocompatible (in comparison to the common, toxic semiconductor nanoparticle alternatives).<sup>13</sup> Bottom-up solution-phase syntheses are favourable for allowing precise control over the final composition of the CNDs, with greater

uniformity and tunable surface functionalities.<sup>14</sup> Exploiting CNDs (and similar carbon nanoparticles) for energy applications has thus far involved utilizing CNDs as light harvesters and redox-active components in photocatalytic systems.<sup>15-19</sup> Though they have been finding widespread application in emerging battery technologies, within the framework of redox-flow batteries CNDs have thus far been confined to electrode design and modification.<sup>20-22</sup> Synthesizing CNDs through hydrothermal treatment of a carbon source and a diamine is a well-established procedure that has been suggested to yield amine-capped CNDs, where the inherent nitrogen-doping favourably impacts the photoluminescence properties of the particles.<sup>23</sup> Primary amine surface groups provide optimal locations to chemically modify the surface of the CNDs using mild conditions like those found for amide coupling. Anthraquinones (AQs) are well-characterized redox-active molecules that are currently under scrutiny as promising aqueous redox-flow battery electrolyte materials.<sup>24-26</sup> However, finding methods of increasing the water-solubility of AQs is crucial to practical implementation.

Herein, we report a microwave reactor-mediated hydrothermal synthesis of CNDs from citric acid and spermidine, the product of which we have characterized by materials and electrochemical methods. Post-synthesis functionalization with anthraquinone-2-carboxylic acid yielded CNDs demonstrating well-defined electrochemistry in 1.0 M NaCl solution and stability over 250 cycles, suggesting that this material may prove a valuable anolyte for aqueous organic redox flow batteries. This represents not only remediation of the issue of membrane permeability by free electrolyte components (i.e., bare AQs) but simultaneously serves to increase AQ solubility in aqueous solution.

## 3.2 Experimental Details

### 3.2.1 Reagents and Materials

All reagents were obtained from Millipore Sigma and used as received unless otherwise indicated. Citric acid monohydrate ( $M_w = 210.14 \text{ g mol}^{-1}$ ), spermidine ( $M_w = 145.25 \text{ g mol}^{-1}$ ,  $\rho = 0.925 \text{ g mL}^{-1}$ ), anthraquinone-2-carboxylic acid (AQCA;  $M_w = 252.22 \text{ g mol}^{-1}$ ), N-hydroxysuccinimide (NHS;  $M_w = 115.09 \text{ g mol}^{-1}$ ) and N-(3-dimethylaminopropyl)-N'-ethylcarbodiimide hydrochloride (EDC•HCl;  $M_w = 191.70 \text{ g mol}^{-1}$ ) were used for the synthesis of the functionalized CNDs. MilliQ water (mQH<sub>2</sub>O; < 18.2 M $\Omega$ .cm; from Millipore Direct-Q<sub>3</sub>) was used as the sole reaction solvent, while standard deionized water (diH<sub>2</sub>O) was used for dialysis steps. Filter papers– VWR medium-fine (5-13  $\mu\text{m}$  pore size) and Millipore GVMP hydrophilic 0.22  $\mu\text{m}$  pore size– and dialysis tubing– Sigma-Aldrich 9 mm flat width, MWCO 2000 benzoylated dialysis tubing– were used for purification.

For electrochemistry, the following additional supplies were required: sodium chloride (NaCl;  $M_w = 58.44 \text{ g mol}^{-1}$ ; Fisher Scientific), sodium hydroxide (NaOH;  $M_w = 40.00 \text{ g mol}^{-1}$ ), silver wire (0.5 mm; Premion®, Alfa Aesar), 4 mm diameter glass tube, plastic shrink wrap, 3 mm diameter porous frits, 2 mm diameter glassy carbon working electrode, a 2 mm diameter glassy carbon rod counter electrode and alumina grit polishing paper (Siawat). mQH<sub>2</sub>O was again used here for all experimentation.

### 3.2.2 Carbon Nanodot (CND) Synthesis

Bare CNDs were synthesized using a modified literature procedure.<sup>27</sup> Briefly, this method will be detailed. All manipulations were done under ambient conditions. To a microwave tube,

1.051 g of citric acid monohydrate (5.00 mmol) and 1.0 mL of mQH<sub>2</sub>O were added and dissolved by stirring. 767  $\mu$ L of spermidine (4.88 mmol) were added dropwise (exothermic processes occur) with rapid stirring, resulting in a light yellow/orange solution. (**Caution!** *Spermidine is corrosive and care should be taken to avoid exposure to skin or eyes.*) After cooling, the tube was capped and placed into the microwave reactor (CEM Discover SP) for reaction. The vessel was pre-stirred for 30 seconds then heated to 210 °C (200 W, 26.0 bar, high stirring) for 3 minutes. (**Caution!** *Heating a pressurized vessel poses an explosion risk. Do not attempt to override safety features on the microwave system.*) Afterward, the solution appeared deep, opaque brown with strong blue photoluminescence upon exposure to a standard UV flashlight. The cap was removed in a fume hood and the solution was diluted with 1.0 mL of mQH<sub>2</sub>O and gravity filtered through coarse grain filter paper into an Erlenmeyer flask, rinsing with minimal mQH<sub>2</sub>O. Next, this solution was vacuum filtered through a frit equipped with a hydrophilic 0.2  $\mu$ m filter, rinsing with minimal (1-2 mL) mQH<sub>2</sub>O. The filtrate was finally transferred to small diameter dialysis tubing (MWCO 2000) and dialyzed against diH<sub>2</sub>O in a large (4 L) beaker with stirring for 8 days, changing the dialysate once a day and qualitatively tracking the photoluminescence in the discarded dialysate (none seen by the final day). The purified solution was transferred to a Falcon tube, frozen in a -70 °C freezer, and placed on a lyophilizer (ZiRBUS VaCo 5-II-D) for 3 days. Once completely dry, the powder was massed (0.336 g) and the mass yield was determined to be 19.7%. In the solid-state, the dark brown powder displayed yellow photoluminescence, while redispersion in water restored the blue photoluminescence. This procedure was repeated to obtain more material for the subsequent reaction.

### ***3.2.3 Carbon Nanodot Functionalization (CND@AQCA)***

To a round-bottom flask equipped with a stir bar, AQCA (252.2 mg; 0.05 mmol) and NHS (230.2 mg; 0.10 mmol) were added and dispersed in 50 mL mQH<sub>2</sub>O. Submerging the flask in an ice-water bath reduced the solution temperature to ~5 °C. EDC•HCl (383.4 mg; 0.10 mmol) was added and stirred cold for 20 mins yielding activated carboxylic acid moieties. Carbon nanodot powder (500 mg; from Section 3.2.2) was massed and fully dissolved in 50 mL mQH<sub>2</sub>O. This solution was added to the cold round bottom flask containing activated carboxylic acid and the ice bath removed to allow the reaction mixture to warm to room temperature as it was stirred for 12 hours. The solution was then vacuum filtered to remove insoluble, unreacted AQCA. The filtrate was transferred to dialysis tubing (2000 MWCO) and dialyzed against diH<sub>2</sub>O for 2 days (dialysate changed twice a day) to remove coupling reagents and dissolved, unreacted AQCA. The purified solution was transferred into Falcon tubes and lyophilized for 3 days. The dry powder was weighed to obtain a mass yield of 0.218 g; 43.6% with respect to the original mass of carbon nanodots.

### ***3.2.4 Materials Characterization***

#### ***3.2.4.1 Transmission Electron Microscopy***

Transmission electron microscopy (TEM) samples, prepared by dispersing the material in question in deionized water and drop-casting on a carbon-coated copper grid, were imaged using a JEOL JEM-ARM200CF S/TEM. The beam was set to an energy of 20 kV. An average shifted histogram was obtained using an online tool by Buriak and coworkers.<sup>28</sup>

#### ***3.2.4.2 Infrared Spectroscopy***

Fourier transform infrared spectroscopy (FTIR) was performed using a Thermo Nicolet 8700 FTIR Spectrometer (Thermo Fischer, USA). The lyophilized powder samples were mixed with potassium bromide powder and pressed into a pellet. Baseline correction was performed. The raw data were plotted using Origin 2021.

#### 3.2.4.3 X-ray Photoelectron Spectroscopy

X-ray photoelectron (XP) data were obtained using a PHI 5000 Versa Probe III X-Ray Photoelectron Spectrometer equipped with a monochromatic Al K $\alpha$  source (50 W; 200  $\mu$ m spot size). The lyophilized powder samples were redispersed in deionized water, drop-cast onto copper foil, and allowed to dry naturally at ambient. Survey spectra were measured with a pass energy of 280 eV while high-resolution spectra used a beam energy of 55 eV. Charge neutralization was employed when necessary. Spectra were processed using CasaXPS and calibrated such that the most intense C 1s emission was set to 284.8 eV. It should be noted that the quality of this data could be improved (e.g., by subtracting a background scan to account for adventitious C contamination, using an internal standard for calibration). Subsequently, the survey spectrum was quantified and the high-resolution C 1s and N 1s spectra were fit with a Shirley-type background.

#### 3.2.4.4 Powder X-ray Diffraction Spectroscopy

Powder X-ray diffraction (PXRD) data were acquired using a Bruker AXS D8 Advance equipped a Cu K $\alpha$  X-ray source (1.5418 Å) and a Bragg-Brentano geometry. The lyophilized sample powder was lightly ground (agate mortar and pestle) to homogenize and placed on a zero-background silicon wafer supported on a PMMA sample holder. The experiment was set to the

following conditions: 15 min run time,  $2\theta = 5-90^\circ$ ,  $0.019677^\circ$  step size, 0.02 s exposure time, 40 kV voltage, and 40 mA current. The raw data were processed using Origin 2021.

#### 3.2.4.5 Ultraviolet-Visible Spectroscopy

Steady-state ultraviolet-visible (UV/Vis) absorption spectra were collected on a Perkin Elmer Lambda 2 Spectrometer under ambient conditions. All samples were measured in  $\text{diH}_2\text{O}$ , using a 1 cm quartz cuvette and continuous background correction (of a solvent blank) using a two-beam configuration. The raw data were plotted using Origin 2021.

#### 3.2.4.6 Photoluminescence Spectroscopy

Photoluminescence (PL) spectra were acquired using a Varian Cary Eclipse Fluorescence Spectrometer. All samples were measured in  $\text{diH}_2\text{O}$ , using a 1 cm quartz cuvette. The excitation wavelength was varied and noted in the presented figures. The raw data were plotted using Origin 2021.

### ***3.2.5 Electrochemical Characterization***

#### 3.2.5.1 Cyclic Voltammetry

A PalmSens4 Benchtop potentiostat (and PSTrace software) was used for all electrochemical measurements. For cyclic voltammetry (CV) studies, a three-electrode cell was utilized, equipped with a  $d = 2$  mm glassy carbon working electrode,  $d = 2$  mm glassy carbon rod counter electrode, and a silver/silver chloride (Ag/AgCl) reference electrode. This reference electrode was assembled as follows: to a narrow glass tube equipped with a porous frit, 3 M  $\text{NaCl}_{(\text{aq})}$  solution was added (ensuring no bubbles), and a length of silver wire just greater than

the length of the glass tube was inserted into the solution. The reference electrode was placed frit-side down, into a vial of 3 M NaCl<sub>(aq)</sub> to equilibrate prior to use and in between uses. The working electrode was cleaned regularly with wetted alumina polishing paper, and blanks were run in between trials to ensure the electrode remained free of contamination. See Appendix A for the experimental setup. For CV experiments, a 5 mg/mL solution of the bare CND or CND@AQCA was prepared in 1 M NaCl<sub>(aq)</sub> (prepared with mQH<sub>2</sub>O) electrolyte. The solutions were pH corrected with 0.1 M NaOH<sub>(aq)</sub> to pH = 7.0. Experiments were run with the following parameters unless otherwise noted: scan cycle 0.0 V → -1.0 V → 1.0 V → 0.0 V, step size of 0.01 V, scan rate 0.1 V/s, 5 scans (where the fifth was used as representative). Optimization studies relating to electrolyte concentration and pH of CND@AQCA test solutions were performed (data not shown).

### 3.2.5.2 Cyclic Voltammetry – Kinetics Studies

A best practices protocol was followed to assess the electron transfer kinetics of the CND@AQCA sample (prepared above).<sup>29</sup> Briefly, CV was performed at variable scan rates (0.025 – 40 V/s and the redox peak separation ( $\Delta E_p$ ) was calculated according to Equation 3-1 (peak positions determined as ‘local maxima’ using Origin 2021). Cycling stability was then assessed by running cyclic voltammetry for 250 cycles and measuring the change in peak current.

**Equation 3-1.** 
$$\Delta E_p = E_{p,a} - E_{p,c}$$

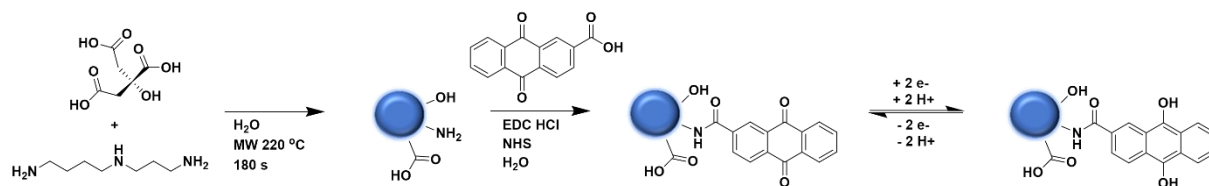
Where  $E_{p,a}$  and  $E_{p,c}$  are the anodic and cathodic peak potentials respectively

### 3.3 Results and Discussion

#### 3.3.1 Synthesis and Purification of CND and CND@AQCA

To realize redox-active CNDs, it was first necessary to develop a synthesis method. In this case, a two-step approach was chosen to allow the CND synthesis and their subsequent functionalization (with anthraquinone-2-carboxylic acid; AQCA). Citric acid and spermidine, both containing multiple reactive functional groups, were selected to facilitate formation of a cross-linked intermediate *en route* to CNDs (Scheme 3-1). CNDs incorporating citrate and spermidine have been previously reported as an anti-bacterial material, however, to our knowledge they have not been applied/explored in other contexts (e.g., energy storage).<sup>30,31</sup> Dialysis and lyophilization were used to purify and isolate CNDs as a powder in a yield of 19.7% by weight. This synthesis method yielded CNDs rich in primary amine surface groups (*vide infra*) that facilitate post-synthesis surface functionalization through an amide coupling reaction with anthraquinone (AQ). AQs have been demonstrated to modulate CND redox potentials when integrated into the bulk but, thus far, we have not identified examples involving only surface modification.<sup>32</sup> AQCA was selected as it is a well-documented redox centre bearing a functional group suitable for an amide coupling reaction with the CND surface. A summary of the synthesis procedure and conceptual redox activity of the final product is shown in Scheme 3-1.

**Scheme 3-1.** A summary of the synthetic procedure targeting redox-active carbon nanodots and the mechanism of redox behaviour.



### 3.3.2 Physical and Structural Properties of CND and CND@AQCA

The successful acquisition of nanoparticles was confirmed using bright field TEM. A distinct population of CNDs was observed possessing an average size of  $12.8 \pm 2.3$  nm (Figure 3-2). This product was then compared to its precursors using FTIR to confirm that the anticipated chemical reaction had taken place and to characterize the functional groups present on the surface and bulk of the bare CNDs. This analysis (Figure 3-3a) verifies that structural changes have occurred as evidenced by the emergence of an O-H stretching absorption ( $3437\text{ cm}^{-1}$ ). The peak arrangement of the spectrum is also congruent with previously reported literature of similar syntheses.<sup>33</sup>

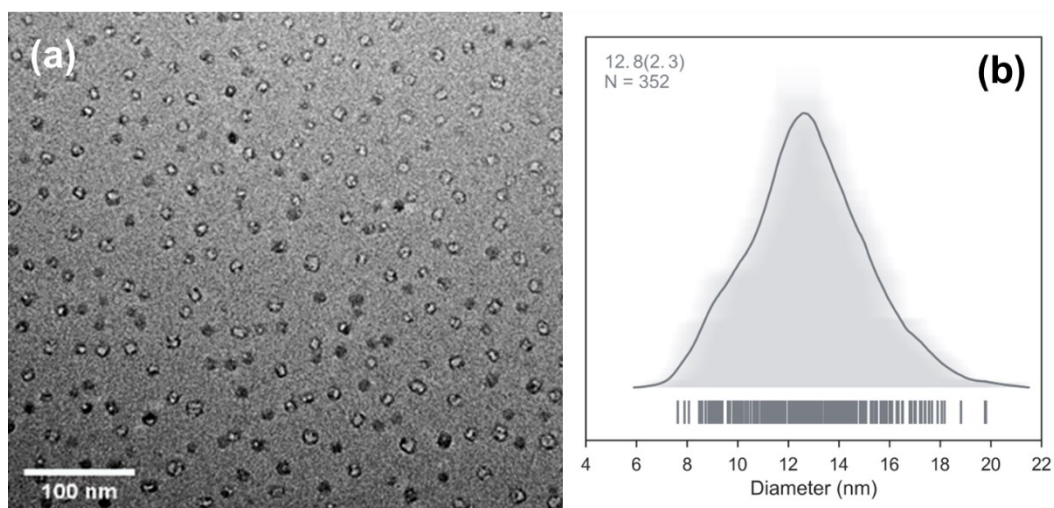


**Figure 3-2.** a) Bright-field transmission electron microscopy of bare carbon nanodots using an accelerating voltage of 20 eV. b) Average shifted histogram of measured particle size.

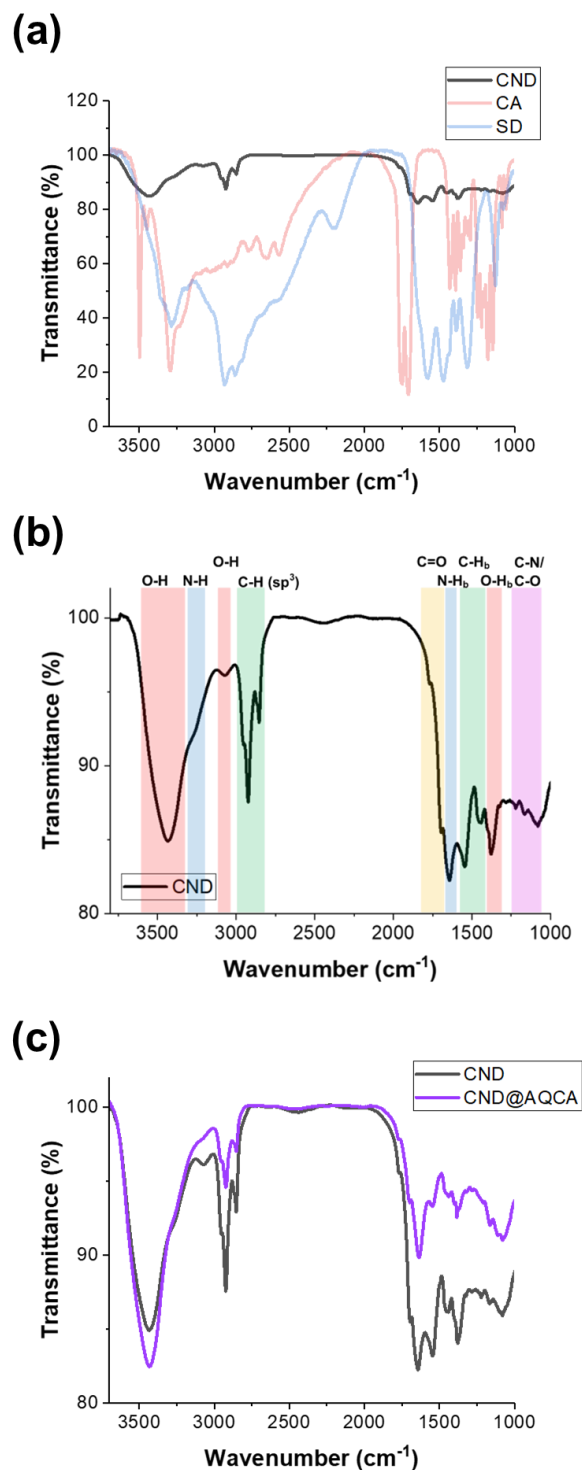


**Figure 3-3.** Fourier transform infrared spectroscopy of carbon nanodot (CND) samples. a) The bare CNDs compared to the precursors used- citric acid (CA) and spermidine (SD). b) The bare CNDs with functional group assignment shown. c) Comparison of the bare CNDs to the same sample after surface functionalization with anthraquinone-2-carboxylic acid (AQCA). Bending is denoted by a subscript “b”.

Other structural features can also be observed which characterize the CNDs. Weak absorptions associated with carboxylic acid functionalities are evidenced by characteristic C=O ( $1767\text{ cm}^{-1}$ ) and O=C-OH ( $3072\text{ cm}^{-1}$ ) stretching frequencies. The spectrum of CNDs also shows a shoulder on the broad alcohol-based feature consistent with N-H amine/amide stretching ( $\sim 3280\text{ cm}^{-1}$ ) (Figure 3-3b). We also note N-H bending ( $1643\text{ cm}^{-1}$ ) and O=C-NH<sub>2</sub> stretching ( $1695\text{ cm}^{-1}$ ) frequencies that would result from the incorporation of spermidine. These data lead to two important conclusions. First, the CNDs likely contain accessible, surface primary amines (as well as carboxylic acids and hydroxyl groups), that provide platforms for post-synthesis modification. Second, the CNDs contain amide groups that likely arise from straightforward condensation of carboxylic acids (citric acid) and amines (spermidine). The FTIR spectrum of CND@AQCA appears largely the same as that for CND, owing to the lack of unique functionalities (Figure 3-3c).

XPS results are consistent with the spectral features noted in the FTIR spectra with the appearance of C, O, and N based emissions (Figure 3-4a). H, which is known to be present based on FTIR results, cannot be detected by XPS and thus is neglected in the following compositional analysis. The presence of Cu is due to the foil support and Si is a common contaminant in our laboratory environment. The composition is similar for both nanodot samples, with a C:O:N ratio of 73:16:11 for CNDs and 75:19:6 for CND@AQCA (Figure 3-4b). Though the role of adventitious C contamination cannot be discounted in explaining the increased C and O content in CND@AQCA, this result is consistent with functionalization of the CND surface by a molecule exclusively containing C and O. C 1s high-resolution spectra display a series of fit emissions corresponding to C bonded to an electronegative atom. For CND these peaks have energies of 284.8 eV (C-C/C-H), 285.8 eV (C-O/C-N), and 287.8 eV (C=O/N-C=O) and were assigned based

upon recent literature (Figure 3-4c).<sup>34,35</sup> For  $\text{CND@AQCA}$ , the same assignments were made for peaks at 284.8 eV, 286.0 eV and 288.1 eV (Figure 3-4d). Owing to the resolution limit of XPS, meaningful distinctions cannot be made between O and N attachments to C here. N 1s high-resolution spectra provide a more detailed picture, confirming the presence of nitrogenous species in CND and  $\text{CND@AQCA}$  (Figure 3-4c,d).

Fitting revealed components for CND at 399.3, 400.1, and 401.3 eV, that we assign to primary amines ( $\text{C-NH}_2$ ), amides ( $\text{N-C=O}$ ), and graphitic N, respectively.<sup>36</sup> Similarly,  $\text{CND@AQCA}$  had contributions at 399.3, 400.0, and 401.2 eV consistent with the same oxidation states noted for the CNDs. However, closer inspection reveals that the relative proportion of primary amines has decreased in the functionalized samples (i.e.,  $\text{CND@AQCA}$ ), while the amide contribution has increased; this is consistent with successful functionalization. The graphitic N content also suggests slight carbonization within the core of the CNDs, although a defined  $\text{sp}^2$  C peak was not identified in the C 1s spectrum.

Given the ambiguous evidence of graphitic ( $\text{sp}^2$  C) domains seen in XPS, PXRD was performed to interrogate the physical structure of CNDs. PXRD shows a broad reflection at 19.2 degrees consistent with an amorphous arrangement of carbon atoms (Figure 3-5). This diffraction angle (corresponding to a lattice spacing of 4.62 Å) and likely relates to the (002) plane of graphite. However, the significant shift to lower angles and broadening compared to pristine, hexagonal graphite (26.6 degrees) indicates the graphitic planes are significantly distorted and suggests the present carbonaceous material is highly disordered.<sup>37</sup> In other words, the CNDs represent an amorphous structure, similar to previously reported CND structures.<sup>38,39</sup> The relative absence of the (100) reflection of graphite (which should appear at ~43.5 degrees) further confirms that the degree of carbonization in the CNDs is minimal, consistent with the

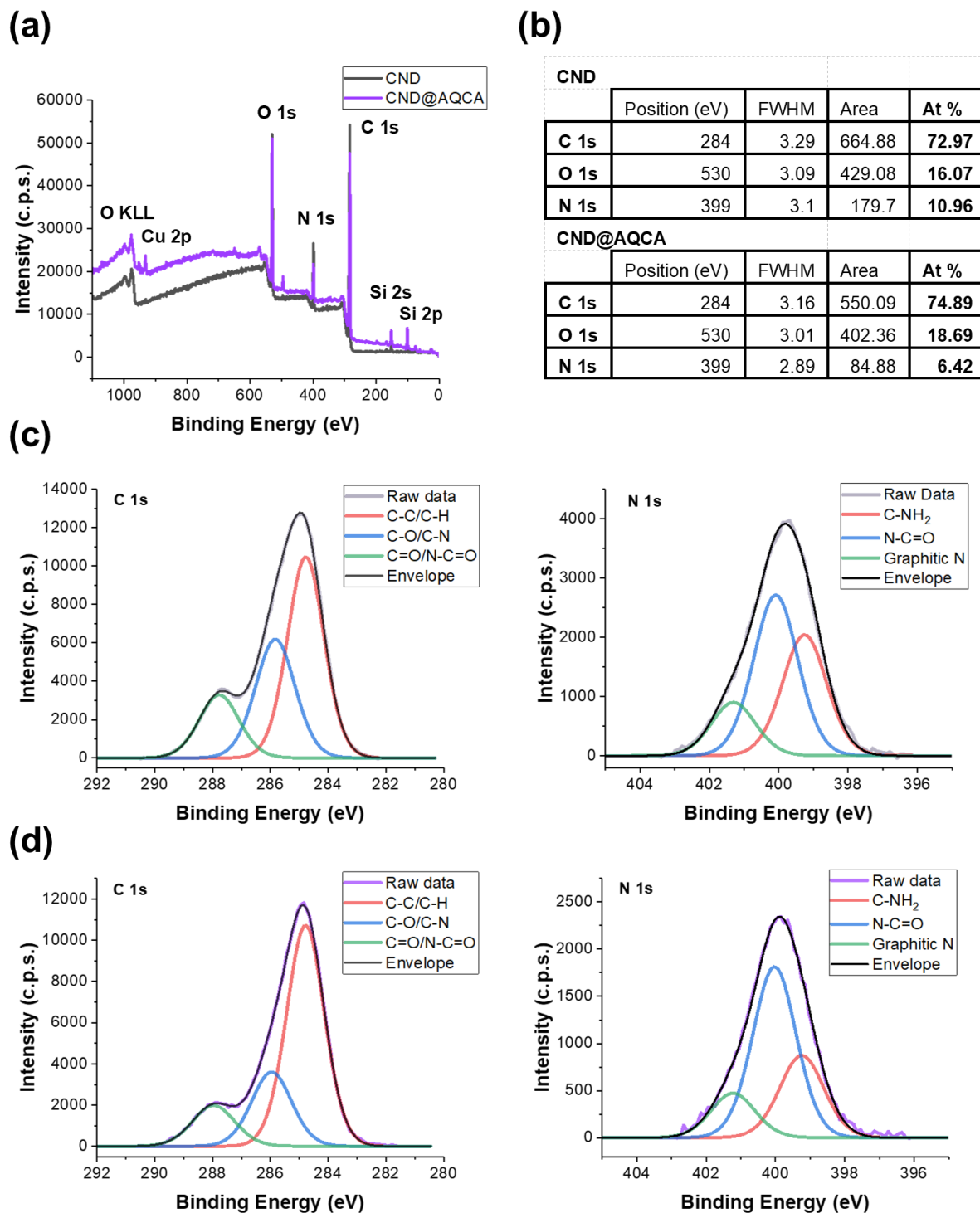


**Figure 3-4.** X-ray photoelectron spectroscopy of bare carbon nanodots (CNDs) and those functionalized with anthraquinone-2-carboxylic acid (CND@AQCA). a) Survey spectra and b) elemental composition. Fit high-resolution spectra of the C 1s and N 1s peaks for d) CNDs and e) CND@AQCA.

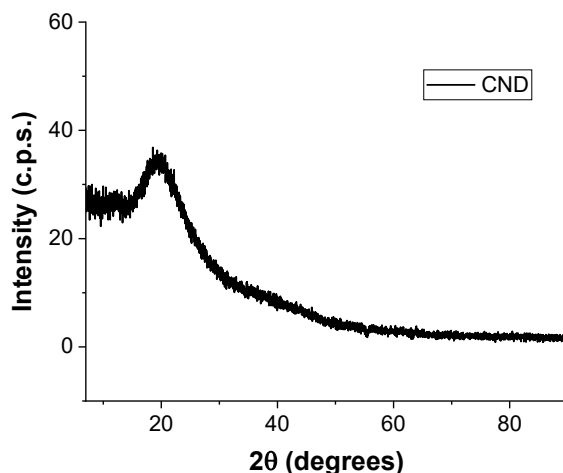


**Figure 3-5.** Powder X-ray diffraction pattern of bare carbon nanodots after background subtraction.

low-temperature processing method used.<sup>40</sup> PXRD was not performed for CND@AQCA as surface functionalization should not impact the internal structure of the CNDs.

It should be noted that nuclear magnetic resonance (NMR) experiments were performed in an attempt to gain further information about the structure of the CNDs and CND@AQCA, however initial experiments were inconclusive (data not shown). As NMR has been recently documented as a key technique for characterizing CNDs and their purity, future investigations will be performed.<sup>41</sup>

### ***3.3.3 Photophysical Properties of the CNDs***

To further characterize the CND and CND@AQCA samples, and gain insight into their photophysical properties, absorption (UV/Vis) and photoluminescence spectroscopy were performed. Both samples display absorption features at 255 nm and 346 nm that we attribute to  $\pi$ - $\pi^*$  transitions of graphitic (C=C) inclusions and  $n$ - $\pi^*$  transitions of carbonyl (C=O) or possibly imine (C=N) functionalities (Figure 3-6a).<sup>33</sup> Both also show a shoulder (~380 nm) on the 346 nm

feature that tails off into the visible region of the spectrum, giving the solution a vibrant yellow colour. Uniquely, CND@AQCA shows a series of peaks (252, 258, 265, 271 nm) superimposed onto the 255 nm peak that we attributed to the vibrational fine structure of the aromatic rings in AQ.

Upon excitation with UV light, aqueous solutions of CND and CND@AQCA produce intense, blue photoluminescence. Photoluminescence spectroscopy was used to probe the emission and it was found that surface functionalization did not impact the emissive behaviour of CNDs. Both sample solutions produced showed an excitation maximum of 376 nm and an emission maximum of 455 nm (Figure 3-6b). As discussed in the literature, the broad emission peaks and excitation-wavelength-dependent behaviour of CNDs suggest photoluminescence is due to a wide range of excitable sites.<sup>42</sup> These may include embedded fluorophores, such as graphene-like domains and nitrogen-containing heterocycles, and surface defect states.<sup>33</sup> Here, excitation-wavelength-dependence is clearly seen (Figure 3-6c,d). The presence of embedded fluorophores (or even “subfluorophores” such as C=O, C=N or N=O) is unsurprising given the amorphous structure of the CNDs which excludes the possibility of photoluminescence due to a particle band gap, as in the case of semiconductor quantum dots.<sup>33</sup>

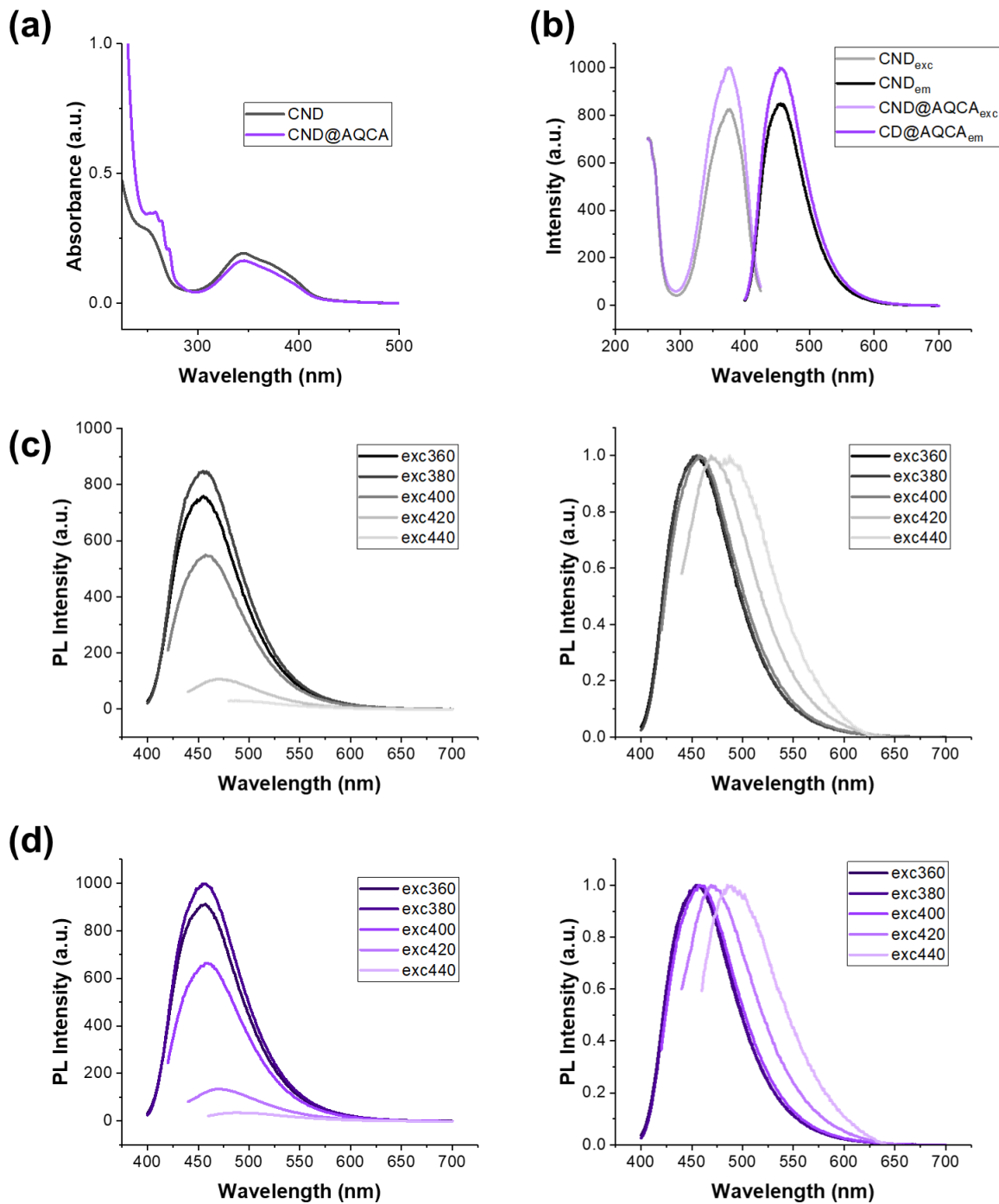


**Figure 3-6.** a) UV/Vis spectroscopic data obtained for aqueous solutions of bare carbon nanodots (CND) and those functionalized with anthraquinone-2-carboxylic acid (CND@AQCA). b) Excitation (ex) and emission (em) maxima for the same solutions. c) Variable excitation wavelength experiments for aqueous CND (c) and CND@AQCA (d) solutions.

### 3.3.4 Electrochemical Performance of *CND@AQCA*

#### 3.3.4.1 Electrochemistry and Surface Attachment

With previous data suggesting a successful surface attachment of AQCA to the CND surface, electrochemical measurements were performed to confirm the imbued redox activity and further interrogate the nature of the attachment. Figure 3-7a shows *CND@AQCA* (5 mg/mL; 1 M NaCl<sub>(aq)</sub>) displays a reduction/oxidation couple while the solvent/electrolyte (1 M NaCl<sub>(aq)</sub>) blank and the bare CNDs (5 mg/mL; 1 M NaCl<sub>(aq)</sub>) did not show this activity. Due to the aqueous solvent, negative potentials induce H<sub>2(g)</sub> evolution, and positive potentials induce O<sub>2(g)</sub> evolution, yielding a potential window of roughly -0.9 – 0.7 V vs. Ag/AgCl (-0.7 – 0.8 V vs. SHE). Within this window, the relevant redox pair is found at a half-wave potential ( $E_{1/2}$ ) of -0.495 V vs. Ag/AgCl.

To investigate the impact of surface attachment on the AQ redox centre, comparative CV was performed. Running a saturated, aqueous solution of AQCA yielded an  $E_{1/2} = -0.589$  V in agreement with literature values (Figure 3-7b).<sup>43,44</sup> This represents a shift of -0.094 V compared to *CND@AQCA*, suggesting surface attachment does slightly change the redox potentials of the AQ electrochemical centre. However, this result alone cannot elucidate information on the mode of association between the CND and AQCA (i.e., covalent bonding or physisorption). Therefore, another solution was tested in which CNDs were added to the saturated AQCA solution (AQCA+CND) and physisorption would be the only interactive force between CNDs and AQCA. This test revealed that physisorption can modulate the peak potentials of AQCA, with AQCA+CND measuring an  $E_{1/2}$  of -0.479 V (Figure 3-7b). Despite displaying a  $E_{1/2}$  similar to AQCA+CND (-0.495 V vs. -0.479 V), *CND@AQCA* also has a peak current significantly higher

than the physisorbed sample ( $i_c = 3.89 \mu\text{A}$  vs.  $2.38 \mu\text{A}$ ). This supports the conclusion that covalent bonding has successfully attached AQCA to the particle surface as the peak current is proportional to the quantity of accessible redox centres. Therefore, covalent attachment has allowed AQCA to exceed its solubility limit, though a small population of physisorbed AQCA cannot be ruled out.

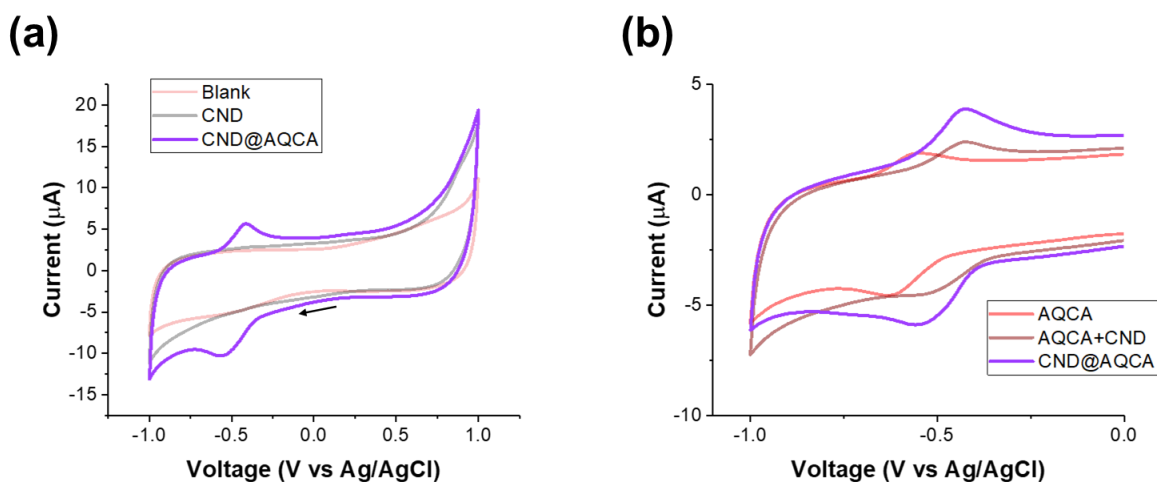


**Figure 3-7.** a) Cyclic voltammetry (CV) comparing carbon nanodots with (CND@AQCA) or without (CND) anthraquinone-2-carboxylic acid (AQCA) functionalization and 1 M NaCl<sub>(aq)</sub> electrolyte blank (0.2 V/s scan rate). b) CV comparing CND@AQCA with a saturated AQCA solution physically mixed with bare CNDs (AQCA+CND), and a saturated AQCA solution (1 M NaCl<sub>(aq)</sub> electrolyte for all; 0.1 V/s scan rate).

### 3.3.4.2 Electrochemical Kinetics

Regarding the intended application of these nanodots as electrolyte materials in redox flow batteries, it is also essential to interrogate the kinetics of electron transfer. As described in a recent review by Buriak and coworkers, there are two primary characteristics that may be probed through cyclic voltammetry: reversibility and diffusion.<sup>29</sup> The former will be explored in the following

subsection and, as will become apparent, the latter will be a future topic of study for the present system.

#### 3.3.4.2.1 Reversibility

At low scan rates (i.e., 0.025 V/s), CND@AQCA has a peak separation ( $\Delta E_p$ ; see Experimental for calculations) of 120 mV (Figure 3-8). Nernstian behaviour for a two-electron process is defined as  $\Delta E_p = 29.5$  mV, however deviation from this value is not uncommon in aqueous organic redox flow battery literature. For example, 9,10-anthraquinone-2,7-disulfonic acid at 1 mM has a reported  $\Delta E_p$  of 34 mV in 1 M sulfuric acid electrolyte.<sup>24</sup> At higher concentrations of active material, though, the  $\Delta E_p$  can increase by nearly 3x for the same AQ (50 mM,  $\Delta E_p > 100$  mV).<sup>45</sup> The mechanism proposed for this is self-dimerization. This effect is less in neutral electrolytes, however, given that the present study is working at the solubility limit of AQCA in water it is not unreasonable that intermolecular attractions may impact electrochemical performance. In fact, the same  $\Delta E_p$  (120 mV) is seen for free AQCA at 0.025 mV/s (Figure 3-9) suggesting the slowed electron transfer is independent of the influence from attachment to the CNDs. It should also be noted that initial attempts at electrochemical impedance spectroscopy were unsuccessful – the Ohmic drop at the electrode interface cannot be compensated for which may have inflated the recorded  $\Delta E_p$  values.<sup>29</sup>

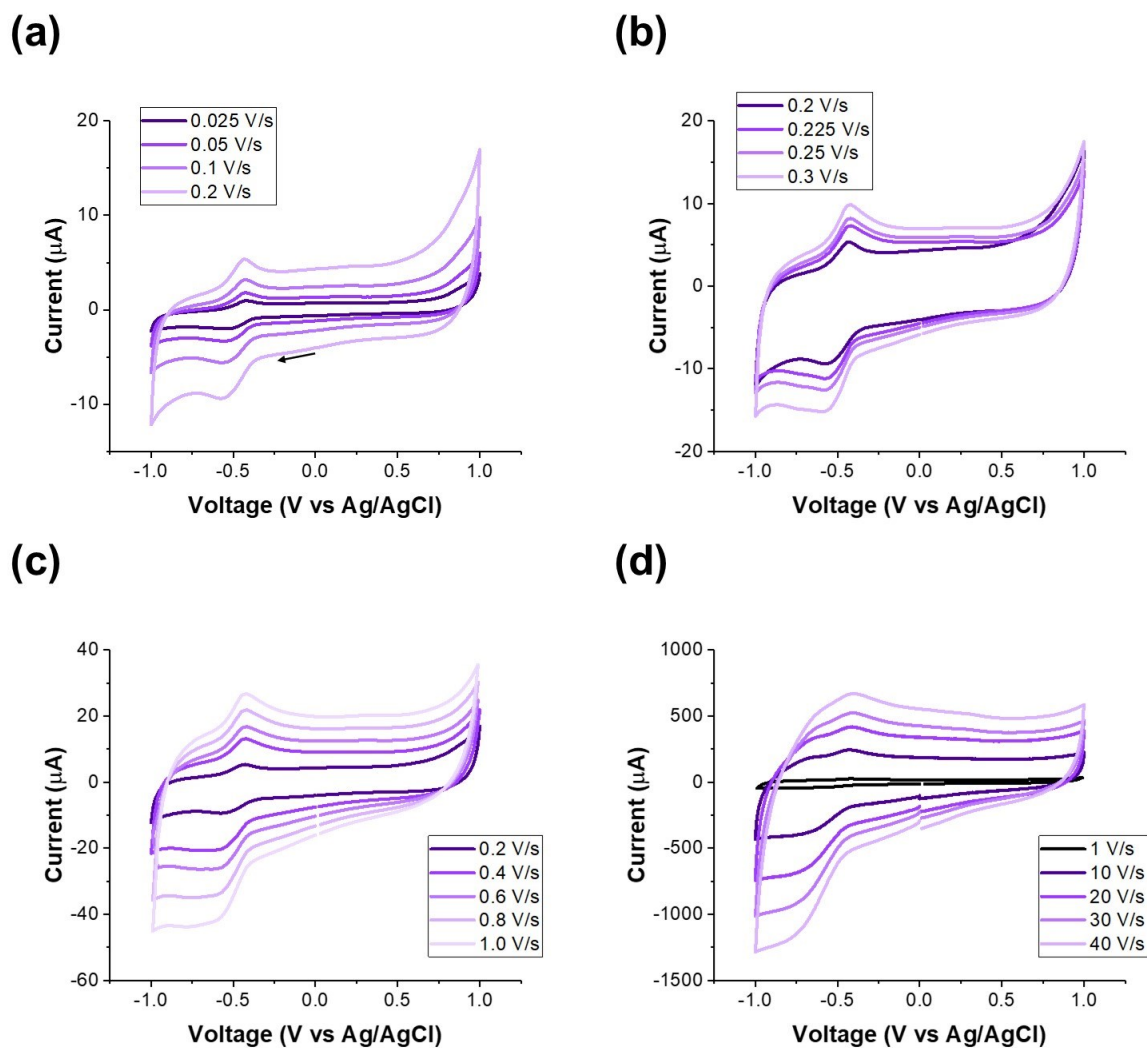
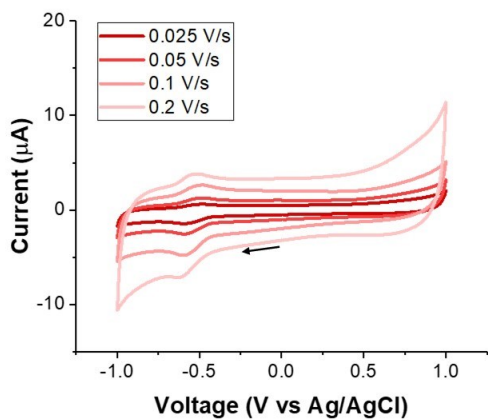
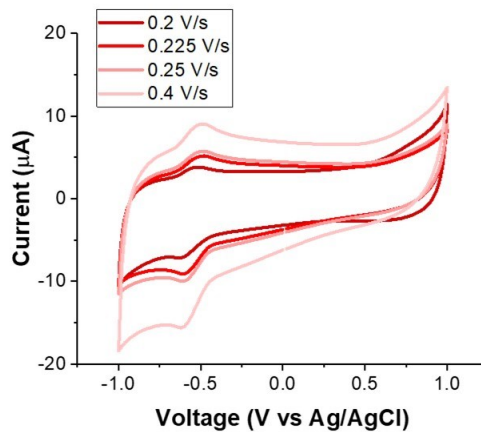


**Figure 3-8.** Cyclic voltammetry (CV) using variable scan rate ( $v$ ) to explore the electrochemical kinetics of carbon nanodots functionalized with anthraquinone-2-carboxylic acid (CND@AQCA). a)  $v = 0.025 - 0.2$  V/s, b)  $v = 0.2 - 0.3$  V/s, c)  $v = 0.2 - 1.0$  V/s, d)  $1 - 40$  V/s.

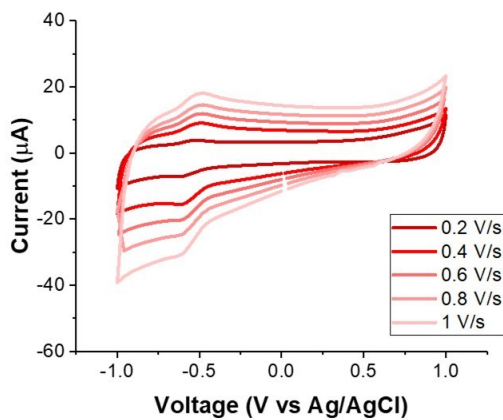
(a)



(b)



(c)



(d)

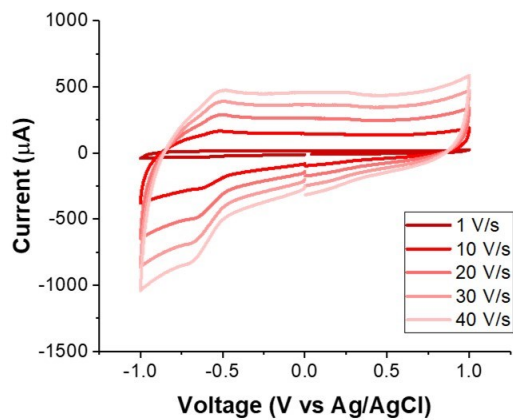


**Figure 3-9.** Cyclic voltammetry (CV) using variable scan rate ( $v$ ) to explore the electrochemical kinetics of anthraquinone-2-carboxylic acid (AQCA). a)  $v = 0.025 - 0.2$  V/s, b)  $v = 0.2 - 0.4$  V/s, c)  $v = 0.2 - 1.0$  V/s, d)  $1 - 40$  V/s.

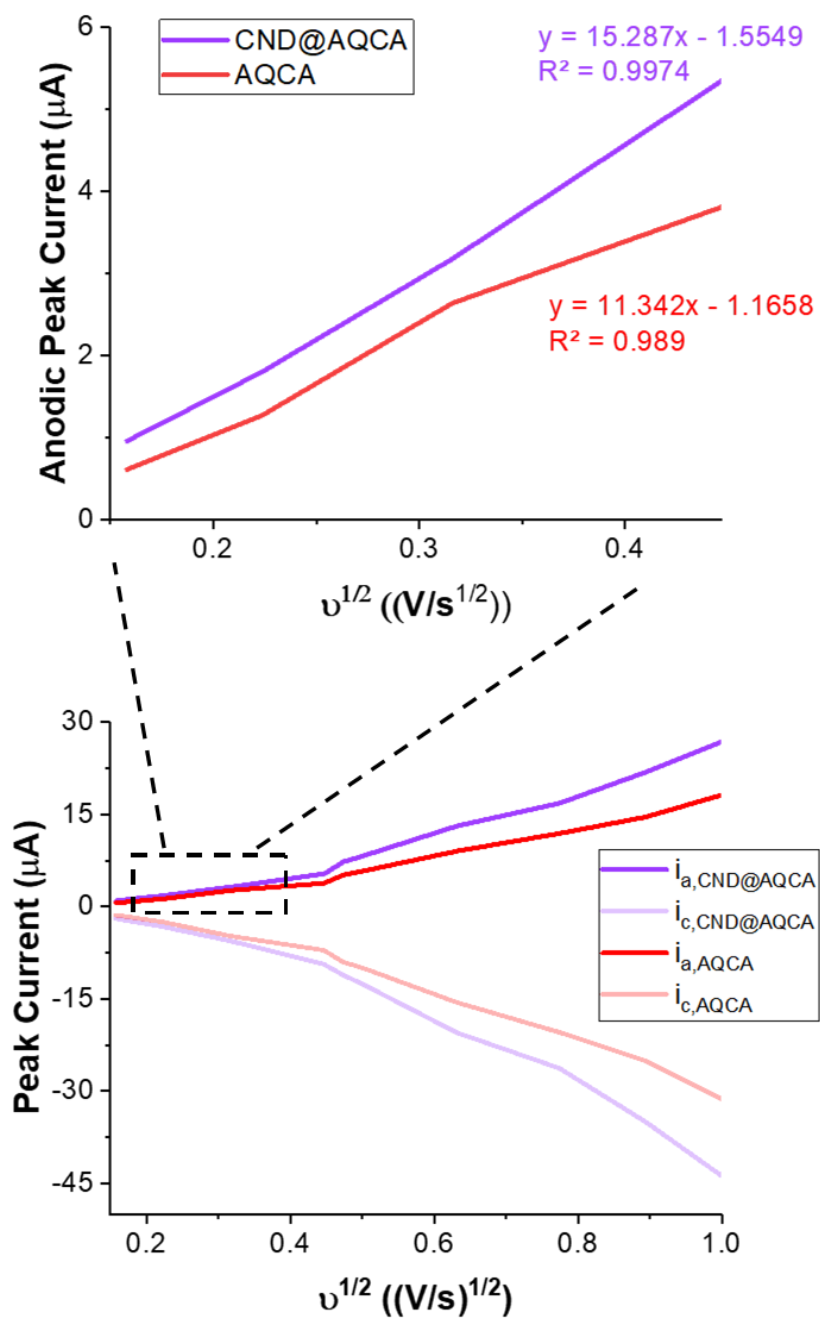


**Figure 3-10.** The peak anodic ( $i_a$ ) and cathodic ( $i_c$ ) currents measured for free anthraquinone (AQCA) and that bound to carbon nanodots (CND@AQCA). Showing magnitude as a function of the square root of scan rate ( $v$ ) (bottom), with an expansion of the linear region (top, inset).

Plotting the peak current ( $i$ ) as a function of the square root of the scan rate, both AQCA and CND@AQCA display non-linear behaviour (Figure 3-10). This, and the previous observation of a non-Nernstian  $\Delta E_p$ , are congruent with quasi-reversible electrochemical kinetics. The lower scan rate region (where diffusion limitations are negligible) is highly linear for CND@AQCA and nearly linear for AQCA suggesting favourable behaviour at scan rates up to 0.4 V/s (Figure 3-10 inset). However, above this value, the non-linearity represents a complex mix of electron transfer kinetics and diffusion limitations. At all scan rates it was noted that the current for CND@AQCA was greater than that for AQCA alone, again supporting that surface functionalization increased the aqueous concentration of AQ moieties.

In summary, the free and CND-bound AQCA appear to demonstrate quasi-reversible electrochemical kinetics and it is the nature of the AQ in the chosen conditions that appears to be limiting the performance of the hybrid as a redox-flow battery material— not the attachment. Therefore, improvements in this system may be achieved by choosing an AQ with more robust behaviour in aqueous solvents.

#### 3.3.4.2.2 Cycling Stability

Lastly, cycling trials were conducted to analyze the cycling stability of CND@AQCA. Within 250 cycles the redox activity was sustained without loss of features or emergence of undesirable features (Figure 3-11a). Within 50 cycles the CV curves had equilibrated and, after 250 cycles, a capacity retention of 70.7% was measured from the plotting of peak current per cycle (Figure 3-11b).

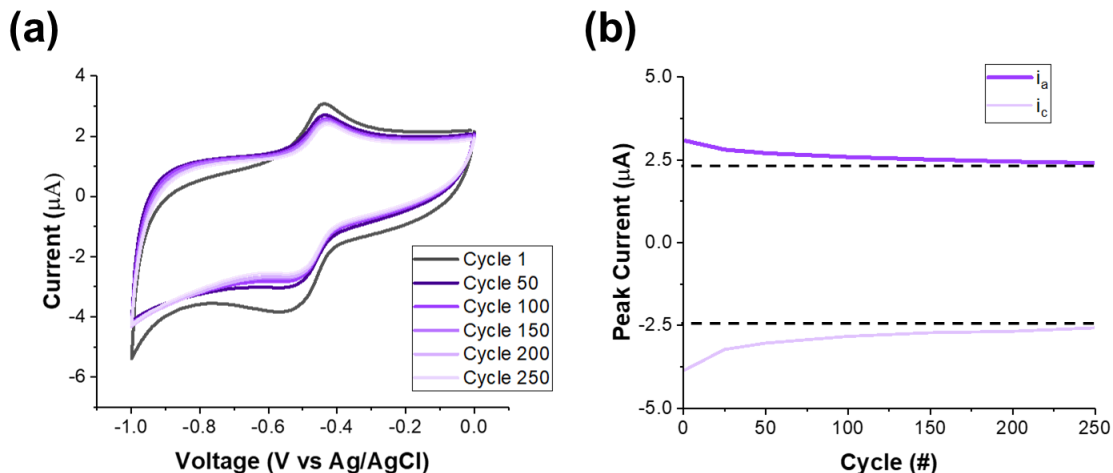


**Figure 3-11.** a) Cyclic voltammetry of anthraquinone-2-carboxylic acid functionalized carbon nanodots (in 1 M NaCl<sub>(aq)</sub>) run for a total of 250 cycles at 0.1 V/s. b) The peak anodic ( $i_a$ ) and cathodic ( $i_c$ ) currents plotted against cycle number.

### 3.4 Conclusions

In conclusion, CNDs have been synthesized through a quick, straightforward microwave reactor-based method to yield well-defined particles suitable for subsequent surface functionalization with AQCA. The product displays the expected features through materials characterization evidencing a primarily amorphous particle with high incorporation of O and N functional groups and photoluminescence arising from small aromatic domains and incorporated organic fluorophores. The functionalized particles display largely the same material properties as the bare ones, however, electrochemistry reveals their imbued redox activity. CND@AQCA shows more impressive peak currents than free AQCA, with behaviour that is stable over 250 cycles, suggesting that the CND is acting as a water solubilizing platform to increase the accessible concentration of AQCA at the electrode. Though the presented data is preliminary, with further study it may be that CND@AQCA or similar redox functionalized CNDs will prove useful materials for redox flow battery electrolytes.

### 3.5 References

- (1) Pain, S. Power Through the Ages. *Nature* **2017**, *551*, S134-S137. DOI: 10.1038/d41586-017-07506-z
- (2) *United Nations Sustainable Development Goal 7*. <https://unstats.un.org/sdgs/report/2021/goal-07/> (accessed 2021-09-21)
- (3) Gür, T. M. Review of Electrical Energy Storage Technologies, Materials and Systems: Challenges and Prospects for Large-Scale Grid Storage. *Energy Environ. Sci.* **2018**, *11*, 2696. DOI: 10.1039/c8ee01419a
- (4) Winsberg, J.; Hagemann, T.; Janoschka, T.; Hager, M. D.; Schubert, U. S. Redox-Flow Batteries: From Metals to Organic Redox-Active Materials. *Angew. Chem. Int. Ed.* **2017**, *56* (3), 686–711. DOI: 10.1002/anie.201604925
- (5) Darling, R. M.; Weber, A. Z.; Tucker, M. C.; Perry, M. L. The Influence of Electric Field on Crossover in Redox-Flow Batteries. *J. Electrochem. Soc.* **2016**, *163* (1), A5014. DOI: 10.1149/2.0031601jes
- (6) Ding, Y.; Zhang, C.; Zhang, L.; Zhou, Y.; Yu, G. Pathways to Widespread Applications: Development of Redox Flow Batteries Based on New Chemistries. *Chem* **2019**, *5* (8), 1964–1987. DOI: 10.1016/j.chempr.2019.05.010
- (7) Baran, M. J.; Braten, M. N.; Montoto, E. C.; Gossage, Z. T.; Ma L.; Chénard, E.; Moore, J. S.; Rodríguez-López, J.; Helms, B. A. Designing Redox-Active Oligomers for Crossover-Free, Nonaqueous Redox-Flow Batteries with High Volumetric Energy Density. *Chem. Mater.* **2018**, *30* (11), 3861–3866. DOI: 10.1021/acs/chemmater.8b01318
- (8) Hendriks, K. H.; Robinson, S. G.; Braten, M. N.; Sevov, C. S.; Helms, B. A.; Sigman, M. S.; Minter, S. D.; Sanford, M. S. High-Performance Oligomeric Catholytes for Effective Macromolecular Separation in Nonaqueous Redox Flow Batteries. *ACS Cent. Sci.* **2018**, *4*, 189–196. DOI: 10.1021/acs.chemmater.8b01318
- (9) Hagemann, T.; Winsberg, J.; Grube, M.; Nischang, I.; Janoschka, T.; Martin, N.; Hager, M. D.; Schubert, U. S. An Aqueous All-Organic Redox-Flow Battery Employing a (2,2,6,6-Tetramethylpiperidin-1-yl)oxyl-Containing Polymer as Catholyte and Dimethyl Viologen Dichloride as Anolyte. *J. Power Sources* **2018**, *379*, 546–554. DOI: 10.1016/j.jpowsour.2017.09.007
- (10) Janoschka, T.; Martin, N.; Martin, U.; Friebe, C.; Morgenstern, S.; Hiller, H.; Hager, M. D.; Schubert, U. S. An Aqueous, Polymer-Based Redox-Flow Battery using Non-Corrosive, Safe, Low-Cost Materials. *Nature* **2015**, *527*, 78–81. DOI: 10.1038/nature15746
- (11) Hatakeyama-Sato, K.; Nagano, T.; Noguchi, S.; Sugai, Y.; Du, J.; Nishide, H.; Oyaizu, K. Hydrophilic Organic Redox-Active Polymer Nanoparticles for Higher Energy Density Flow Batteries. *ACS Appl. Polym. Mater.* **2019**, *1*, 188–196. DOI: 10.1021/acsapm.8b00074
- (12) Montoto, E. C.; Nagarjuna, G.; Hui, J.; Burgess, M.; Sekerak, N. M.; Hernández-Burgos, K.; Wei, T.-S.; Kneer, M.; Grolman, J.; Cheng, K. J.; Lewis, J. A.; Moore, J. S. Rodríguez-López,

J. Redox Active Colloids as Discrete Energy Storage Carriers. *J. Am. Chem. Soc.* **2016**, *138* (40), 13230–13237. DOI: 10.1021/jacs.6b06365

(13) Xiao, L.; Sun, H. Novel Properties and Applications of Carbon Nanodots. *Nanoscale Horiz.* **2018**, *3*, 565. DOI: 10.1039/c8nh00106e

(14) Đorđević, L.; Arcudi, F.; Cacioppo, M.; Prato, M. A Multifunctional Chemical Toolbox to Engineer Carbon Dots for Biomedical and Energy Applications. *Nature Nanotechnology* **2022**, *17*, 112-130. DOI: 10.1038/s41565-021-01051-7

(15) Rigodanza, F.; Đorđević, L.; Arcudi, F.; Prato, M. Customizing the Electrochemical Properties of Carbon Nanodots by Using Quinones in Bottom-Up Synthesis. *Angew. Chem.* **2018**, *57* (18), 5062-5067. DOI: 10.1002/anie.201801707

(16) Martindale, B. C.; Hutton, G. A. M.; Caputo, C. A.; Reisner, E. Solar Hydrogen Production Using Carbon Quantum Dots and a Molecular Nickel Catalyst. *J. Am. Chem. Soc.* **2015**, *137*, 6018-6025. DOI: 10.1021/jacs.5b01650

(17) Hutton, G. A. M.; Martindale, B. C. M.; Reisner, E. Carbon Dots as Photosensitizers for Solar-Driven Catalysis. *Chem. Soc. Rev.* **2017**, *46*, 6111. DOI: 10.1039/c7cs00235a

(18) Achilleos, D. S.; Kasap, H.; Reisner, E. Photocatalytic Hydrogen Generation Coupled to Pollutant Utilization using Carbon Dots Produced from Biomass. *Green Chem.* **2020**, *22*, 2831. DOI: 10.1039/d0gc00318b

(19) Achilleos, D. S.; Yang, W.; Kasap, H.; Savateev, A.; Markushyna, Y.; Durrant, J. R.; Reisner, E. Solar Reforming of Biomass with Homogeneous Carbon Dots. *Angew. Chem. Int. Ed.* **2020**, *59*, 18184-18188. DOI: 10.1002/anie.202008217

(20) Guo, R.; Li, L.; Wang, B.; Xiang, Y.; Zou, G.; Zhu, Y.; Hou, H.; Ji, X. Functionalized Carbon Dots for Advanced Batteries. *Energy Storage Materials* **2021**, *37*, 8-39. DOI: 10.1016/j.ensm.2021.01.020

(21) Zhou, Y.; Liu, L.; Shen, L.; Wu, L.; Yu, L.; Liang, F.; Xi, J. Carbon Dots Promoted Vanadium Flow Batteries for All-Climate Energy Storage. *Chem. Commun.* **2017**, *52*, 7565-7568. DOI: 10.1039/c7cc00691h

(22) Kim, K. J.; Park, M.-S.; Kim, Y.-J.; Kim, J. H.; Dou, S. X.; Skyllas-Kazacos, M. A Technology Review of Electrodes and Reaction Mechanisms in Vanadium Redox Flow Batteries. *J. Mater. Chem. A* **2015**, *3*, 16913-16933. DOI: 10.1039/c5ta02613j

(23) Arcudi, F.; Đorđević, L.; Prato, M. Synthesis, Separation, and Characterization of Small and Highly Fluorescent Nitrogen-Doped Carbon NanoDots. *Angew. Chem.* **2016**, *128*, 2147-2152. DOI: 10.1002/anie.201510158

(24) Huskinson, B.; Marshak, M. P.; Suh, C.; Er, S.; Gerhardt, M. R.; Galvin, C. J.; Chen, X.; Aspuru-Guzik, A.; Gordon, R. G.; Aziz, M. J. A Metal-Free Organic-Inorganic Aqueous Flow Battery. *Nature* **2014**, *505*, 195-198. DOI: 10.1038/nature12909

(25) Jing, Y.; Fell, E. M.; Wu, M.; Jin, S.; Ji, Y.; Pollack, D. A.; Tang, Z.; Ding, D.; Bahari, M.; Goulet, M.-A.; Tsukamoto, T.; Gordon, R. G.; Aziz, M. J. Anthraquinone Flow Battery Reactants with Nonhydrolyzable Water-Solubilizing Chains Introduced via a Generic Cross-Coupling Method. *ACS Energy Lett.* **2022**, *7* (1), 226-235. DOI: 10.1021/acseenergylett.1c02504

- (26) Wu, M.; Bahari, M.; Fell, E. M.; Gordon, R. G.; Aziz, M. J. High-Performance Anthraquinone with Potentially Low Cost for Aqueous Redox Flow Batteries. *J. Mater. Chem. A* **2021**, *9*, 26709-26716. DOI: 10.1039/D1TA08900E
- (27) Đorđević, L.; Arcudi, F.; Prato, M. Preparation, Functionalization and Characterization of Engineered Carbon Nanodots. *Nat Protoc* **2019**, *14*, 2931-2953. DOI: 10.1038/s41596-019-0207-x
- (28) Anderson, S. L.; Lubber, E. J.; Olsen, B. C.; Buriak, J. M. Substance over Subjectivity: Moving Beyond the Histogram. *Chem. Mater.* **2016**, *28*, 5973-5975. DOI: 10.1021/acs.chemmater.6b03430
- (29) Wang, H.; Sayed, S. Y.; Lubber, E. J.; Olsen, B. C.; Shirurkar, S. M.; Venkatakrisnan, S.; Tefashe, U. M.; Farquhar, A. K.; Smotkin, E. S.; McCreery, R. L.; Buriak, J. M. Redox Flow Batteries: How to Determine Electrochemical Kinetic Parameters. *ACS Nano* **2020**, *14*, 2575-2584. DOI: 10.1021/acsnano.0c01281
- (30) Jian, H.-J.; Wu, R.-S.; Lin, T.Y.; Li, Y.-J.; Lin, H.-J.; Harroun, S. G.; Lai, J.-Y.; Huang, C.-C. Super-Cationic Carbon Quantum Dots Synthesized from Spermidine as an Eye Drop Formulation for Topical Treatment of Bacterial Keratitis. *ACS Nano* **2017**, *11*, 6703-6716. DOI: 10.1021/acsnano.7b01023
- (31) Li, Y.-J.; Harroun, S. G.; Su, Y.-C.; Huang, C.-F.; Unnikrishnan, B.; Lin, H.-J.; Lin, C.-H.; Huang, C.-C. Synthesis of Self-Assembled Spermidine-Carbon Quantum Dots Effective against Multidrug-Resistant Bacteria. *Advanced Healthcare Materials* **2016**, *5* (19), 2545-2554. DOI: 10.1002/adhm.201600297
- (32) Rigodanza, F.; Đorđević, L.; Arcudi, F.; Prato, M. Customizing the Electrochemical Properties of Carbon Nanodots by Using Quinones in Bottom-Up Synthesis. *Angew. Chem.* **2018**, *57*, 5062-5067. DOI: 10.1002/anie.201801707
- (33) Schneider, J.; Reckmeier, C. J.; Xiong, Y.; von Seckendorff, M.; Suscha, A. S.; Kasák, P.; Rogach, A. L. Molecular Fluorescence in Citric Acid-Based Carbon Dots. *J. Phys. Chem. C* **2107**, *121* (3), 2014-2022. DOI: 10.1021/acs.jpcc.6b12519
- (34) Morgan, D. J. Comments on the XPS Analysis of Carbon Materials. *C* **2021**, *7*, 51. DOI: 10.3390/c7030051
- (35) Gengenbach, T. R.; Major, G. H.; Linford, M. R.; Easton, C. D. Practical Guides for X-Ray Photoelectron Spectroscopy (XPS): Interpreting the Carbon 1s Spectrum. *J. Vac. Sci. Technol. A* **2021**, *39*, 013204. DOI: 10.1116/6.0000682
- (36) Yadav, R. M.; Li, Z.; Zhang, T.; Sahin, O.; Roy, S.; Gao, G.; Guo, H.; Vajtai, R.; Wang, L.; Ajayan, P. M.; Wu, J. Amine-Functionalized Carbon Nanodot Electrocatalysts Converting Carbon Dioxide to Methane. *Adv. Mater.* **2022**, *34*, 2105690. DOI: 10.1002/adma.202105690
- (37) Li, Z. Q.; Lu, C.J.; Xia, Z. P.; Zhou, Y.; Luo, Z. X-Ray Diffraction Patterns of Graphitic and Turbostratic Carbon. *Carbon* **2007**, *45* (8), 1686-1695. DOI: 10.1016/j.carbon.2007.03.038
- (38) Bourlinos, A. B; Stassinopoulos, A.; Anglos, D; Zboril, R.; Karakassides, M.; Giannelis, E. P. Surface Functionalized Carbogenic Quantum Dots. *Small* **2008**, *4*, 455-458. DOI: 10.1002/smll.200700578

- (39) Huang, X.; Yang, L.; Hao, S.; Zheng, B.; Yan, L.; Qu, F.; Asiri, A. M.; Sun, X. N-Doped Carbon Dots: A Metal-Free Co-Catalyst on Hematite Nanorod Arrays toward Efficient Photoelectrochemical Water Oxidation. *Inorg. Chem. Front.* **2017**, *4*, 537. DOI: 10.1039/C6QI00517A
- (40) Chen, T.; Pan, L.; Loh, T. A. J.; Chua, D. H. C.; Yao, Y.; Chen, Q.; Li, D.; Qin, W.; Sun, Z. Porous Nitrogen-Doped Carbon Microspheres as Anode Materials for Lithium Ion Batteries. *Dalton Trans.* **2014**, *43*, 14931. DOI: 10.1039/c4dt01223b
- (41) Bartolomei, B.; Bogo, A.; Amato, F.; Ragazzon, G.; Prato, M. Nuclear Magnetic Resonance Reveals Molecular Species in Carbon Nanodot Samples Disclosing Flaws. *Angew. Chem. Int. Ed.* **2022**, *61*, e202200038. DOI: 10.1002/anie.202200038
- (42) Siddique, A. B.; Pramanick, A. K.; Chatterjee, S.; Ray, M. Amorphous Carbon Dots and their Remarkable Ability to Detect 2,4,6-Trinitrophenol. *Scientific Reports* **2018**, *8*, 9770. DOI: 10.1038/s41598-018-28021-9
- (43) Haque, M. A.; Rahman, M. M.; Susan, M. A. B. H.; Aqueous Electrochemistry of Anthraquinone and Its Correlation with the Dissolved States of a Cationic Surfactant. *J Solution Chem* **2011**, *40*, 861-875. DOI: 10.1007/s10953-011-9690-6
- (44) Quan, M.; Sanchez, D.; Wasylkiw, M. F.; Smith, D. K. Voltammetry of Quinones in Unbuffered Aqueous Solution: Reassessing the Roles of Proton Transfer and Hydrogen Bonding in the Aqueous Electrochemistry of Quinones. *J. Am. Chem. Soc.* **2007**, *129*, 12847-12856. DOI: 10.1021/ja0743083
- (45) Carney, T. J.; Collins, S. J.; Moore, J. S.; Brushett, F. R. Concentration-Dependent Dimerization of Anthraquinone Disulfonic Acid and Its Impact on Charge Storage. *Chem. Mater.* **2017**, *29*, 4801-4810. DOI: 10.1021/acs.chemmater.7b00616

### 3.6 Appendix



**Figure 3-A1.** Visual results before and after microwave reactor treatment of the reaction solution.



**Figure 3-A2.** Dialysis setup used for purification of the CNDs and CND@AQCA.

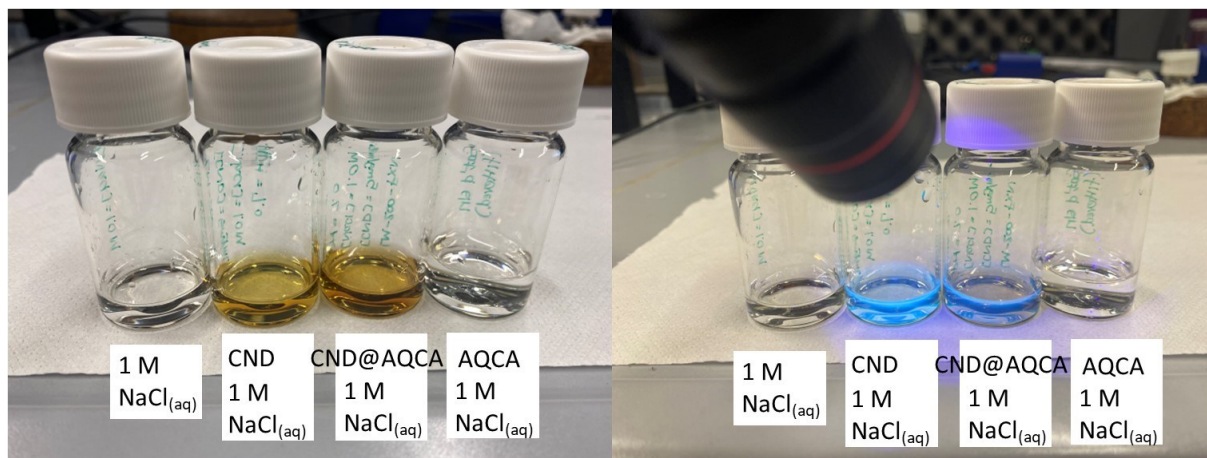


**Figure 3-A3.** Samples prepared for electrochemical analysis showing the appearance under ambient lighting as well as during exposure to a standard UV flashlight.



**Figure 3-A4.** Electrode set-up derived for use with the PalmSens4 potentiostat. Showing the lead attachment (left) and the appearance of the Ag/AgCl reference, graphite counter, and graphite working electrodes (right).

## **Chapter 4:**

### **Conclusions & Future Work**

## 4.1 Thesis Conclusions

Throughout this thesis the tailoring of quantum dots (QDs) and related photoluminescent particles (like carbon nanodots, CNDs) toward specific applications has been explored. In Chapter 1 a general foundation for understanding materials science, the evolution of QDs, and their properties was established.

In Chapter 2, silicon quantum dots (SiQDs) were discussed in the context of nitroaromatic sensing. It was shown that SiQDs can be rendered water-soluble by surface functionalization with carboxylic acid and polyethylene oxide moieties and the photoluminescence (PL) of these SiQDs can be quenched on exposure to various nitrotoluenes explosives. Additionally, pairing the SiQD sensor with an enzymatic sensor can allow for differentiation of explosives from chemically similar nerve agents.

Chapter 3 then turns to CNDs tailored by surface functionalization with anthraquinones. This imbues the nanodots with redox activity suitable for use in battery applications. Owing to the relatively young field of CNDs, extensive materials characterization was performed to elucidate their structural and optical properties. Anticipating the utilization of the functionalized CNDs as potential redox flow battery electrolytes, electrochemical experiments were detailed to investigate the redox reactions, kinetics, and cycling stability of the materials.

## 4.2 Future Directions

The fields of SiQDs and CNDs will undoubtedly continue expanding into the future, as the drive for sustainable, easily renewable, and affordable materials establishes itself within the economy. The technological applications discussed in this thesis represent a contribution to the

scope of possibilities for these materials, however, improvements remain to be made which will better suit the material to our modern needs and values.

In light of the work done towards SiQD/enzyme tandem sensors (Chapter 2) it would be useful to expand the scope of this system to differentiate various other chemically similar hazardous chemicals. Additionally, acknowledging that natural enzymes are inherently unstable at room temperature (and only marginally stabilized by gel-encapsulation), it may prove advantageous to investigate “nanozymes”, or synthetic nanomaterial mimics of enzymes that can be tailored to provide the same response but with increased stability.<sup>1-3</sup> Finally, considering the shift in our consumer environment towards a circular economy (where products are built to be recycled), further investigation is needed to probe the possibility of a multi-use sensing system. This may be achieved by, for instance, immobilizing the sensor components onto a scaffold which can be rinsed to remove the quenching agents and restore PL for subsequent tests.<sup>4-6</sup> Such a system would also be useful to confirm the quenching mechanism as an energy transfer as opposed to an aggregation-induced quenching effect.

The work done in attaching anthraquinones to CND surfaces (Chapter 3) has yielded redox-active, aqueous-compatible CNDs however the kinetics were shown to be less than ideal for redox flow battery applications. An exploration of different anthraquinone ligands, for example those bearing water-solubilizing groups (sulfonates, glycols, etc.) as well as more rigorous pH investigations may prove useful for optimizing the redox characteristics of the final CNDs.<sup>7,8</sup> In the former case, water-solubilized precursor ligands may also allow for a higher rate of surface functionalization which could increase the final concentration of redox centres available per CND (increasing the current density of the respective battery). Of course, this also raises the point that more robust methods of quantifying surface coverage should be established. Finally, beyond the

intended application as a RFB electrolyte material, electrochemically-active (e.g., quinone-modified) CNDs are currently a popular candidate for photocatalytic applications.<sup>9</sup> Once the CNDs are optimized, it would be exceptionally useful to explore the versatility of these materials for other avenues of renewable energy technologies.

### 4.3 References

- (1) Chapman, R.; Stenzel, M. H. All Wrapped up: Stabilization of Enzymes within Single Enzyme Nanoparticles. *J. Am. Chem. Soc.* **2019**, *141* (7), 2754-2769. DOI: 10.1021/jacs.8b10338
- (2) Wang, H.; Wan, K.; Shi, X. Recent Advances in Nanozyme Research. *Adv. Mater.* **2019**, *31*, 1805368. DOI: 10.1002/adma.201805368
- (3) Jiang, D.; Ni, D.; Rosenkrans, Z. T.; Huang, P.; Yan, X.; Cai, W. Nanozyme: New Horizons for Responsive Biomedical Applications. *Chem. Soc. Rev.* **2019**, *48*, 3683-3704. DOI: 10.1039/C8CS00718G
- (4) Nöll, G.; Su, Q.; Heidel, B.; Yu, Y. A Reusable Sensor for the Label-Free Detection of Specific Oligonucleotides by Surface Plasmon Fluorescence Spectroscopy. *Adv. Healthcare Mater.* **2014**, *3*, 42-46. DOI: 10.1002/adhm.201300056
- (5) Chen, L.; Tian, X.; Li, Y.; Yang, C.; Huang, Y.; Nie, Y. Rapid and Sensitive Screening of Multiple Polycyclic Aromatic Hydrocarbons by a Reusable Fluorescent Sensor Array. *J. Hazard. Mater.* **2022**, *424*, 127694. DOI: 10.1016/j.jhazmat.2021.127694
- (6) Bardhan, S.; Roy, S.; Chanda, D. K.; Mondal, D.; Das, S.; Das, S. Flexible and Reusable Carbon Dot Decorated Natural Microcline Membrane: A Futuristic Probe for Multiple Heavy Metal Induced Carcinogen Detection. *Microchimica Acta* **2021**, *188*, 134. DOI: 10.1007/s00604-021-04787-0
- (7) Lee, W.; Permatasari, A.; Kwon, Y. Neutral pH Aqueous Redox Flow Batteries Using an Anthraquinone-Ferrocyanide Redox Couple. *J. Mater. Chem. C* **2020**, *8*, 5727. DOI: 10.1039/d0tc00640h
- (8) Hu, B.; Luo, J.; Hu, M.; Yuan, B.; Liu, T. L. A pH-Neutral, Metal-Free Aqueous Organic Redox Flow Battery Employing an Ammonium Anthraquinone Anolyte. *Angew. Chem.* **2019**, *131*, 16782-16789. DOI: 10.1002/anie.201907934
- (9) Rigodanza, F.; Đorđević, L.; Arcudi, F.; Prato, M. Customizing the Electrochemical Properties of Carbon Nanodots by Using Quinones in Bottom-Up Synthesis. *Angew. Chem.* **2018**, *130*, 5156-5161. DOI: 10.1002/ange.201801707

## Works Cited

Achilleos, D. S.; Kasap, H.; Reisner, E. Photocatalytic Hydrogen Generation Coupled to Pollutant Utilization Using Carbon Dots Produced from Biomass. *Green Chem.* **2020**, *22*, 2831. DOI: 10.1039/d0gc00318b

Achilleos, D. S.; Yang, W.; Kasap, H.; Savateev, A.; Markushyna, Y.; Durrant, J. R.; Reisner, E. Solar Reforming of Biomass with Homogeneous Carbon Dots. *Angew. Chem. Int. Ed.* **2020**, *59*, 18184-18188. DOI: 10.1002/anie.202008217

Alivisatos, A. P. Semiconductor Clusters, Nanocrystals, and Quantum Dots. *Science* **1996**, *271*, 933-937. DOI: 10.1126/science.271.5251.933

Anderson, S. L.; Lubner, E. J.; Olsen, B. C.; Buriak, J. M. Substance over Subjectivity: Moving Beyond the Histogram. *Chem. Mater.* **2016**, *28*, 5973-5975. DOI: 10.1021/acs.chemmater.6b03430

Arcudi, F.; Đorđević, L.; Prato, M. Synthesis, Separation, and Characterization of Small and Highly Fluorescent Nitrogen-Doped Carbon NanoDots. *Angew. Chem.* **2016**, *128*, 2147-2152. DOI: 10.1002/anie.201510158

Ashe, K. The Steps to Sustainability. *Nat. Chem.* **2022**, *14*, 243-244. DOI: 10.1038/s41557-022-00903-6

Askim, J. R.; Mahmoudi, M.; Suslick, K. S. Optical Sensor Arrays for Chemical Sensing: The Optoelectronic Nose. *Chem. Soc. Rev.* **2013**, *42*, 8649. DOI: 10.1039/C3CS60179J

Baig, N.; Kammakam, I.; Falath, W. Nanomaterials: A Review of Synthesis Methods, Properties, Recent Progress, and Challenges. *Mater. Adv.* **2021**, *2*, 1821-1871. DOI: 10.1039/D0MA00807A

Ban, R.; Zheng, F.; Zhang, J. A Highly Sensitive Fluorescence Assay for 2,4,6-Trinitrotoluene Using Amine-Capped Silicon Quantum Dots as a Probe. *Anal. Methods* **2015**, *7*, 1732-1737. DOI: 10.1039/C4AY02729A

Baran, M. J.; Braten, M. N.; Montoto, E. C.; Gossage, Z. T.; Ma L.; Chénard, E.; Moore, J. S.; Rodríguez-López, J.; Helms, B. A. Designing Redox-Active Oligomers for Crossover-Free, Nonaqueous Redox-Flow Batteries with High Volumetric Energy Density. *Chem. Mater.* **2018**, *30* (11), 3861-3866. DOI: 10.1021/acs/chemmater.8b01318

Bardhan, S.; Roy, S.; Chanda, D. K.; Mondal, D.; Das, S.; Das, S. Flexible and Reusable Carbon Dot Decorated Natural Microcline Membrane: A Futuristic Probe for Multiple Heavy Metal Induced Carcinogen Detection. *Microchimica Acta* **2021**, *188*, 134. DOI: 10.1007/s00604-021-04787-0

Bartolomei, B.; Bogo, A.; Amato, F.; Ragazzon, G.; Prato, M. Nuclear Magnetic Resonance Reveals Molecular Species in Carbon Nanodot Samples Disclosing Flaws. *Angew. Chem. Int. Ed.* **2022**, *61*, e202200038. DOI: 10.1002/anie.202200038

Behera, P.; Mohanty, A.; De, M. Functionalized Fluorescent Nanodots for Discrimination of Nitroaromatic Compounds. *ACS Appl. Nano Mater.* **2020**, *3*, 2846-2856. DOI: 10.1021/acsnm.0c00132

Bhattacharjee, S.; Rietjens, I. M. C. M.; Singh, M. P.; Atkins, T. M.; Purkait, T. K.; Xu, Z.; Regli, S.; Shukaiak, A.; Clark, R. J.; Mitchell, B. S.; Alink, G. M.; Marcelis, A. T. M.; Fink, M. J.; Veinot, J. G. C.; Kauzlarich, S. M.; Zuilhof, H. Cytotoxicity of Surface-Functionalized Silicon and Germanium Nanoparticles: The Dominant Role of Surface Charges. *Nanoscale* **2013**, *5*, 4870-4883. DOI: 10.1039/C3NR34266B

Borowik, Ł.; Nguyen-Tran, T.; Roca I Cabarrocas, P.; Mélin, T. Doped Semiconductor Nanocrystal Junctions. *J. Appl. Phys.* **2013**, *114*, 204305. DOI: 10.1063/1.4834516

Bourlinos, A. B; Stassinopoulos, A.; Anglos, D; Zboril, R.; Karakassides, M.; Giannelis, E. P. Surface Functionalized Carbogenic Quantum Dots. *Small* **2008**, *4*, 455-458. DOI: 10.1002/sml.200700578

Cademartiri, L.; Ozin, G. A. *Concepts of Nanochemistry*. WILEY-VCH Verlag GmbH & Co. KGaA, Weinheim; 2009.

Callister, W. D.; Rethwisch, D. G. *Materials Science and Engineering: An Introduction*. 9<sup>th</sup> ed.; John Wiley & Sons, Inc.; 2014.

Camata, R. P.; Atwater, H. A.; Vahala, K. J.; Flagan, R. C. Size Classification of Silicon Nanocrystals. *Appl. Phys. Lett.* **1996**, *68*, 3162. DOI: 10.1063/1.115811

Canham, L. T. Silicon Quantum Wire Array Fabrication by Electrochemical and Chemical Dissolution of Wafers. *Appl. Phys. Lett.* **1990**, *57*, 1046. DOI: 10.1063/1.103561

Wang, K.; Gao, Z.; Gao, G.; Wng, Y.; Shen, G.; Cui, D. Systematic Safety Evaluation on Photoluminescent Carbon Dots. *Nanoscale Res Lett* **2013**, *8*, 122. DOI: 10.1186/1556-276X-8-122

Cao, L.; Mezziani, M. J.; Sahu, S.; Sun, Y.-P. Photoluminescence Properties of Graphene Versus Other Carbon Nanomaterials. *Accounts of Chemical Research* **2013**, *46(1)*, 171-180. DOI: 10.1021/ar300128j

Cao, Z.; Peng, F.; Hu, Z.; Chu, B.; Zhong, Y.; Su, Y.; He, S.; He, Y. *In Vitro* Cellular Behaviours and Toxicity Assays of Small-Sized Fluorescent Silicon Nanoparticles. *Nanoscale* **2017**, *9*, 7602-7611. DOI: 10.1039/C7NR00530J

Capobianco, N.; Hunault, M. O. J. Y.; Balcon-Berry, S.; Galois, L.; Sandron, D.; Calas, G. The *Grande Rose* of the Reims Cathedral: An Eight-Century Perspective on the Colour Management of Medieval Stained Glass. *Sci. Rep.* **2019**, *9*, 3287. DOI: 10.1038/s41598-019-39740-y

Carney, T. J.; Collins, S. J.; Moore, J. S.; Brushett, F. R. Concentration-Dependent Dimerization of Anthraquinone Disulfonic Acid and Its Impact on Charge Storage. *Chem. Mater.* **2017**, *29*, 4801-4810. DOI: 10.1021/acs.chemmater.7b00616

Chan, T.-L.; Zhang, S. B.; Chelikowsky, J. R. An Effective One-Particle Theory for Formation Energies in Doping Si Nanostructures. *Appl. Phys Lett.* **2011**, *98*, 133116. DOI: 10.1063/1.3571552

Chapman, R.; Stenzel, M. H. All Wrapped up: Stabilization of Enzymes within Single Enzyme Nanoparticles. *J. Am. Chem. Soc.* **2019**, *141* (7), 2754-2769. DOI: 10.1021/jacs.8b10338

Chen, J.; Jiang, Z.; Ackerman, J. D.; Yazdani, M.; Hou, S.; Nugen, S. R.; Rotello, V. M. Electrochemical Nanoparticle-Enzyme Sensors for Screening Bacterial Contamination in Drinking Water. *Analyst* **2015**, *140*, 4991-4996. DOI: 10.1039/C5AN00637F

Chen, L.; Tian, X.; Li, Y.; Yang, C.; Huang, Y.; Nie, Y. Rapid and Sensitive Screening of Multiple Polycyclic Aromatic Hydrocarbons by a Reusable Fluorescent Sensor Array. *J. Hazard. Mater.* **2022**, *424*, 127694. DOI: 10.1016/j.jhazmat.2021.127694

Chen, T.; Pan, L.; Loh, T. A. J.; Chua, D. H. C.; Yao, Y.; Chen, Q.; Li, D.; Qin, W.; Sun, Z. Porous Nitrogen- Doped Carbon Microspheres as Anode Materials for Lithium Ion Batteries. *Dalton Trans.* **2014**, *43*, 14931. DOI: 10.1039/c4dt01223b

Choi, Y.; Kang, B.; Lee, J.; Kim, S.; Kim, G. T.; Kang, H.; Lee, B. R.; Kim, H.; Shim, S.-H.; Lee, G.; Kwon, O.-H.; Kim, B.-S. Integrative Approach toward Uncovering the Origin of Photoluminescence in Dual Heteroatom-Doped Carbon Nanodots. *Chem. Mater.* **2016**, *28* (19), 6840-6847. DOI: 10.1021/acs.chemmater.6b0171

Clark, R. J.; Aghajamali, M.; Gonzalez, C. M.; Hadidi, L.; Islam, M. A.; Javadi, M.; Mobarok, M. H.; Purkait, T. K.; Robidillo, C. J. T.; Sinelnikov, R.; Thiessen, A. N.; Washington, J.; Yu, H.; Veinot, J. G. C. From Hydrogen Silsesquioxane to Functionalized Silicon Nanocrystals. *Chem. Mater.* **2017**, *29*, 80-89. DOI: 10.1021/acs.chemmater.6b02667

Content, S.; Trogler, W. C.; Sailor, M. J. Detection of Nitrobenzene, DNT, and TNT Vapors by Quenching of Porous Silicon Photoluminescence. *Chem. - Eur. J.* **2000**, *6*, 2205-2213. DOI: 10.1002/1521-3765(20000616)6:12<2205::AID-CHEM2205>3.0.CO;2-A

Cotta, M. A. Quantum Dots and Their Applications: What Lies Ahead? *ACS Appl. Nano Mater.* **2020**, *3*, 4920-4924. DOI 10.1021/acsanm.0c01386

Derfus, A. M.; Chan, W. C. W.; Bhatia, S. N. Probing the Cytotoxicity of Semiconductor Quantum Dots. *Nano Letters* **2004**, *4* (1), 11-18. DOI: 10.1021/nl0347334

Darling, R. M.; Weber, A. Z.; Tucker, M. C.; Perry, M. L. The Influence of Electric Field on Crossover in Redox-Flow Batteries. *J. Electrochem. Soc.* **2016**, *163* (1), A5014. DOI: 10.1149/2.0031601jes

Dasog, M.; Yang, Z.; Regli, S.; Atkins, T. M.; Faramus, A.; Singh, M. P.; Muthuswamy, E.; Kauzlarich, S. M.; Tilley, R. D.; Veinot, J. G.C. Chemical Insight into the Origin of Red and Blue Photoluminescence Arising from Freestanding Silicon Nanocrystals. *ACS Nano* **2013**, *7*, 2676–2685. DOI: 10.1021/nn4000644

Ding, Y.; A, H.-W.; Hoi, H.; Campbell, R. E. Förster Resonance Energy Transfer-Based Biosensors for Multiparameter Ratiometric Imaging of Ca<sup>2+</sup> Dynamics and Caspase-3 Activity in Single Cells. *Anal. Chem.* **2011**, *83* (24), 9687-9693. DOI: 10.1021/ac202595g

Ding, Y.; Zhang, C.; Zhang, L.; Zhou, Y.; Yu, G. Pathways to Widespread Applications: Development of Redox Flow Batteries Based on New Chemistries. *Chem* **2019**, *5* (8), 1964–1987. DOI: 10.1016/j.chempr.2019.05.010

Dohnalová, K. ; Gregorkiewicz, T. ; Kůsová, K. Silicon Quantum Dots: Surface Matters. *J. Phys.: Condens. Matter* **2014**, *26*, 173201. DOI : 10.1088/0953-8984/26/17/173201

Dorđević, L.; Arcudi, F.; Cacioppo, M.; Prato, M. A Multifunctional Chemical Toolbox to Engineer Carbon Dots for Biomedical and Energy Applications. *Nature Nanotechnology* **2022**, *17*, 112-130. DOI: 10.1038/s41565-021-01051-7

Dorđević, L.; Arcudi, F.; Prato, M. Preparation, Functionalization and Characterization of Engineered Carbon Nanodots. *Nat Protoc* **2019**, *14*, 2931-2953. DOI: 10.1038/s41596-019-0207-x

Duncan, B.; Le, N. D. B.; Alexander, C.; Gupta, A.; Tonga, G. Y.; Yazdani, M.; Landis, R. F.; Rossi, L. M.; Quach, A. D.; Rosenzweig, Z. Glucose Oxidase-Magnetite Nanoparticle Bioconjugate for Glucose Sensing. *Anal. Bioanal. Chem.* **2004**, *380*, 606-613. DOI: 10.1007/s00216-004-2770-3

Efros, A. L.; Brus, L. E. Nanocrystal Quantum Dots: From Discovery to Modern Development. *ACS Nano* **2021**, *15* (4), 6192-6210. DOI: 10.1021/acsnano.1c01399

Ekimov, A. I.; Efros, A. L.; Onushchenko, A. A. Quantum Size Effect in Semiconductor Microcrystals. *Solid State Commun.* **1985**, *56* (11), 921-924. DOI: 10.1016/S0038-1098(85)80025-9

Ekimov, A. Growth and Optical Properties of Semiconductor Nanocrystals in a Glassy Matrix. *J. Lumin.* **1996**, *70*, 1-20. DOI: 10.1016/0022-2313(96)00040-3

Elbersen, R.; Vijselaar, W.; Tiggelaar, R. M.; Gardeniers, H.; Huskens, J. Fabrication and Doping Methods for Silicon Nano- and Micropillar Arrays for Solar-Cell Applications: A Review. *Adv. Mater.* **2015**, *27*, 6781-6796. DOI: 10.1002/pip.2726

Eletsii, A. V.; Smirnov, B. M. Fullerenes and Carbon Structures. *Phys.-Usp.* **1995**, *38*, 935.

Feng, T.; Tao, S.; Yue, D.; Zeng, Q.; Chen, W.; Yang, B. Recent Advanced in Energy Conversion Application of Carbon Dots: From Optoelectronic Devices to Electrocatalysis. *Small* **2020**, *16*, 2001295. DOI: 10.1002/sml.202001295

Feynman, R. P. There's Plenty of Room at the Bottom. *Engineering and Science* **1960**, *23* (5), 22-36.

Freestone, I.; Meeks, N.; Sax, M.; Higgitt, C. The Lycurgus Cup – A Roman Nanotechnology. *Gold Bull* **2007**, *40*, 270-277. DOI: 10.1007/BF03215599

Gengenbach, T. R.; Major, G. H.; Linford, M. R.; Easton, C. D. Practical Guides for X-Ray Photoelectron Spectroscopy (XPS): Interpreting the Carbon 1s Spectrum. *J. Vac. Sci. Technol. A* **2021**, *39*, 013204. DOI: 10.1116/6.0000682

Geim, A. K. Graphene: Status and Prospects. *Science* **2009**, *324* (5934), 1530-1534. DOI: 10.1126/science.1158877

Geoffrion, L. D.; Guisbiers, G. Quantum Confinement: Size on the Grill! *J. Phys. Chem. Solids* **2020**, *140*, 109320. DOI: 10.1016/j.jpcs.2019.109320

Germain, M. E.; Knapp, M. J. Optical Explosives Detection: From Color Changes to Fluorescence Turn-On. *Chem. Soc. Rev.* **2009**, *38*, 2543-2555. DOI: 10.1039/B809631G

Germanenko, I. N.; Li, S.; Samy El-Shall, M. Decay Dynamics and Quenching of Photoluminescence from Silicon Nanocrystals by Aromatic Nitro Compounds. *J. Phys. Chem. B* **2001**, *105*, 59-66. DOI: 10.1021/jp002340c

Gonzalez, C. M.; Iqbal, M.; Dasog, M.; Piercey, D. G.; Lockwood, R.; Klapoetke, T. M.; Veinot, J. G. C. Detection of High-Energy Compounds Using Photoluminescent Silicon Nanocrystal Paper Based Sensors. *Nanoscale* **2014**, *6*, 2608-2612. DOI: 10.1039/C3NR06271F

Gonzalez, C. M.; Veinot, J. G. C. Silicon Nanocrystals for the Development of Sensing Platforms. *J. Mater. Chem. C* **2016**, *4*, 4863. DOI: 10.1039/C6TC01159D

Guo, R.; Li, L.; Wang, B.; Xiang, Y.; Zou, G.; Zhu, Y.; Hou, H.; Ji, X. Functionalized Carbon Dots for Advanced Batteries. *Energy Storage Materials* **2021**, *37*, 8-39. DOI: 10.1016/j.ensm.2021.01.020

Gür, T. M. Review of Electrical Energy Storage Technologies, Materials and Systems: Challenges and Prospects for Large-Scale Grid Storage. *Energy Environ. Sci.* **2018**, *11*, 2696. DOI: 10.1039/c8ee01419a

Hagemann, T.; Winsberg, J.; Grube, M.; Nischang, I.; Janoschka, T.; Martin, N.; Hager, M. D.; Schubert, U. S. An Aqueous All-Organic Redox-Flow Battery Employing a (2,2,6,6,-Tetramethylpiperidin-1-yl)oxyl-Containing Polymer as Catholyte and Dimethyl Viologen Dichloride as Anolyte. *J. Power Sources* **2018**, *379*, 546–554. DOI: 10.1016/j.jpowsour.2017.09.007

Haque, M. A.; Rahman, M. M.; Susan, M. A. B. H.; Aqueous Electrochemistry of Anthraquinone and Its Correlation with the Dissolved States of a Cationic Surfactant. *J. Solution Chem* **2011**, *40*, 861-875. DOI: 10.1007/s10953-011-9690-6

Hatakeyama-Sato, K.; Nagano, T.; Noguchi, S.; Sugai, Y.; Du, J.; Nishide, H.; Oyaizu, K. Hydrophilic Organic Redox-Active Polymer Nanoparticles for Higher Energy Density Flow Batteries. *ACS Appl. Polym. Mater.* **2019**, *1*, 188–196. DOI: 10.1021/acsapm.8b00074

Haufler, R. E.; Conceicao, J.; Chibante, L. P. F.; Chai, Y.; Byrne, N. E.; Flanagan, S.; Haley, M. M.; O'Brien, S. C.; Pan, C.; Xiao, Z.; Billups, W. E.; Ciufolini M. A.; Hauge, R. H.; Margrave, J. L.; Wilson, L. J.; Curl, R. F.; Smalley, R. E. Efficient Production of C<sub>60</sub> (Buckminsterfullerene), C<sub>60</sub>H<sub>36</sub>, and the Solvated Buckide Ion. *Phys. Chem.* **1990**, *94*, 8634. DOI: 10.1021/j100387a005

Havrdova, M.; Hola, K.; Skopalik, J.; Tomankova, K.; Petr, M.; Cepe, K.; Polakova, K.; Tucek, J.; Bourlinoe, A. B.; Zboril, R. Toxicity of Carbon Dots- Effect of Surface Functionalization on the Cell Viability, Reactive Oxygen Species Generation and Cell Cycle. *Carbon* **2016**, *99*, 238-248. DOI: 10.1016/j.carbon.2015.12.027

Heath, J. R. A Liquid-Solution-Phase Synthesis of Crystalline Silicon. *Science* **1999**, *258*, 1131-1133. DOI : 10.1126/science.258.5085.1131

Henderson, E. J.; Kelly, J. A.; Veinot, J. G. C. Influence of HSiO<sub>1.5</sub> Sol–Gel Polymer Structure and Composition on the Size and Luminescent Properties of Silicon Nanocrystals. *Chem. Mater.* **2009**, *21*, 5426–5434. DOI: 10.1021/cm902028q

Heitmann, J.; Müller, F.; Zacharias, M.; Gösele, U. Silicon Nanocrystals: Size Matters. *Adv. Mater.* **2005**, *17*, 795-803. DOI : 10.1002/adma.200401126

Hendriks, K. H.; Robinson, S. G.; Braten, M. N.; Sevov, C. S.; Helms, B. A.; Sigman, M. S.; Minter, S. D.; Sanford, M. S. High-Performance Oligomeric Catholytes for Effective

Macromolecular Separation in Nonaqueous Redox Flow Batteries. *ACS Cent. Sci.* **2018**, *4*, 189–196. DOI: 10.1021/acs.chemmater.8b01318

Hessel, C. M.; Henderson, E. J.; Veinot, J. G. C. Hydrogen Silsesquioxane: A Molecular Precursor for Nanocrystalline Si–SiO<sub>2</sub> Composites and Freestanding Hydride-Surface-Terminated Silicon Nanoparticles. *Chem. Mater.* **2006**, *18*, 6139–6146. DOI: 10.1021/cm0602803

Hochella, M. F.; Mogk, D. W.; Ranville, J.; Allen, I. C.; Luther, G. W.; Marr, L. C.; McGrail, B. P.; Murayama, M.; Qafoku, N. P.; Posso, K. M.; Sahai, N.; Schroeder, P. A.; Vikesland, P.; Westerhoff, P.; Yang, Y. Natural, Incidental, and Engineered Nanomaterials and Their Impacts on the Earth System. *Science* **2019**, *363*, 1414. DOI: 10.1126/science.aau8299

Hu, B.; Luo, J.; Hu, M.; Yuan, B.; Liu, T. L. A pH-Neutral, Metal-Free Aqueous Organic Redox Flow Battery Employing an Ammonium Anthraquinone Anolyte. *Angew. Chem.* **2019**, *131*, 16782–16789. DOI: 10.1002/anie.201907934

Huang, X.; Yang, L.; Hao, S.; Zheng, B.; Yan, L.; Qu, F.; Asiri, A. M.; Sun, X. N-Doped Carbon Dots: A Metal-Free Co-Catalyst on Hematite Nanorod Arrays Toward Efficient Photoelectrochemical Water Oxidation. *Inorg. Chem. Front.* **2017**, *4*, 537. DOI: 10.1039/C6QI00517A

Hughes, A. D.; Glenn, I. C.; Patrick, A. D.; Ellington, A.; Anslyn, E. V. A Pattern Recognition Based Fluorescence Quenching Assay for the Detection and Identification of Explosive Analytes. *Chem. - Eur. J.* **2008**, *14*, 1822–1827. DOI: 10.1002/chem.200701546

Huskinson, B.; Marshak, M. P.; Suh, C.; Er, S.; Gerhardt, M. R.; Galvin, C. J.; Chen, X.; Aspuru-Guzik, A.; Gordon, R. G.; Aziz, M. J. A Metal-Free Organic-Inorganic Aqueous Flow Battery. *Nature* **2014**, *505*, 195–198. DOI: 10.1038/nature12909

Hutton, G. A. M.; Martindale, B. C. M.; Reisner, E. Carbon Dots as Photosensitizers for Solar-Driven Catalysis. *Chem. Soc. Rev.* **2017**, *46*, 6111. DOI: 10.1039/c7cs00235a

Huisken, F.; Ledoux, G.; Guillois, O.; Reynaud, C. Light-Emitting Silicon Nanocrystals from Laser Pyrolysis. *Adv. Mater.* **2002**, *14*, 1861–1865. DOI : 10.1002/adma.200290021

International Union of Pure and Applied Chemistry. Chapter 18.4.3.7: Detection and quantification capabilities. In *Compendium of Analytical Nomenclature, Definitive Rules 1997*, 4<sup>th</sup> ed.; Lengyel, T., Inczédy, J., Ure, A.M., Eds. [https://media.iupac.org/publications/analytical\\_compendium/](https://media.iupac.org/publications/analytical_compendium/) (accessed 07-02-2019)

Hu, T.; Sang, W.; Chen, K.; Gu, H.; Ni, Z.; Liu, S. Simple and Sensitive Colorimetric Detection of a Trace Amount of 2,4,6-Trinitrotoluene (TNT) with QD Multilayer-Modified Microchannel Assays. *Mater. Chem. Front.* **2019**, *3*, 193. DOI: 10.1039/C8QM00430G

Janoschka, T.; Martin, N.; Martin, U.; Friebe, C.; Morgenstern, S.; Hiller, H.; Hager, M. D.; Schubert, U. S. An Aqueous, Polymer-Based Redox-Flow Battery Using Non-Corrosive, Safe, Low-Cost materials. *Nature* **2015**, *527*, 78–81. DOI: 10.1038/nature15746

Jian, H.-J.; Wu, R.-S.; Lin, T.Y.; Li, Y.-J.; Lin, H.-J.; Harroun, S. G.; Lai, J.-Y.; Huang, C.-C. Super-Cationic Carbon Quantum Dots Synthesized from Spermidine as an Eye Drop Formulation for Topical Treatment of Bacterial Keratitis. *ACS Nano* **2017**, *11*, 6703–6716. DOI: 10.1021/acsnano.7b01023

Jiang, D.; Ni, D.; Rosenkrans, Z. T.; Huang, P.; Yan, X.; Cai, W. Nanozyme: New Horizons for Responsive Biomedical Applications. *Chem. Soc. Rev.* **2019**, *48*, 3683-3704. DOI: 10.1039/C8CS00718G

Jing, Y.; Fell, E. M.; Wu, M.; Jin, S.; Ji, Y.; Pollack, D. A.; Tang, Z.; Ding, D.; Bahari, M.; Goulet, M.-A.; Tsukamoto, T.; Gordon, R. G.; Aziz, M. J. Anthraquinone Flow Battery Reactants with Nonhydrolyzable Water-Solubilizing Chains Introduced via a Generic Cross-Coupling Method. *ACS Energy Lett.* **2022**, *7* (1), 226-235. DOI: 10.1021/acsenergylett.1c02504

Kahn, A. Fermi Level, Work Function and Vacuum Level. *Mater. Horiz.* **2016**, *3*, 7-10. DOI: 10.1039/C5MH00160A

Kalyanasundaram, K.; Borgarello, E.; Duonghong, D.; Grätzle, M. Cleavage of Water by Visible-Light Irradiation of Colloidal CdS Solutions; Inhibition of Photocorrosion by RuO<sub>2</sub>. *Angew. Chem. Int. Ed. Engl.* **1981**, *20*, 987-988. DOI: 10.1002/anie.198109871

Kang, H. R.; Kang, K. C.; Newby, J. G.; Lee, J. H. Fieldable Flow Injection Analysis System with 1,1'-Oxalyldiimidazole Chemiluminescence Detection Capable of Quantifying Acetylcholine. *Anal. Methods* **2011**, *3*, 374-379. DOI: 10.1039/C0AY00440E

Kim, K. J.; Park, M.-S.; Kim, Y.-J.; Kim, J. H.; Dou, S. X.; Skyllas-Kazacos, M. A Technology Review of Electrodes and Reaction Mechanisms in Vanadium Redox Flow Batteries. *J. Mater. Chem. A* **2015**, *3*, 16913-16933. DOI: 10.1039/c5ta02613j

Kou, X.; Jiang, S.; Park, S.-J.; Meng, L.-Y. A Review: Recent Advances in Preparations and Applications of Heteroatom-Doped Carbon Quantum Dots. *Dalton Trans* **2020**, *49*, 6915-6938. DOI: 10.1039/D0DT01004A

Kovalev, D.; Heckler, H.; Polisski, G.; Koch, F. Optical Properties of Si Nanocrystals. *Phys. Stat. Sol.* **1999**, *215*, 871. DOI: [https://doi.org/10.1002/\(SICI\)1521-3951\(199910\)215:2<871::AID-PSSB871>3.0.CO;2-9](https://doi.org/10.1002/(SICI)1521-3951(199910)215:2<871::AID-PSSB871>3.0.CO;2-9)

Kroto, H. W.; Heath, J. R.; O'Brien, S. C.; Curl, R. F.; Smalley, R. E. C<sub>60</sub>: Buckminsterfullerene. *Nature* **1985**, *318*, 162-163. DOI: 10.1038/318162a0

Kustov, L. M.; Mashkin, P. V.; Zakharov, V. N.; Abramenko, N. B.; Krysanov, E. Y.; Aslanov, L. A.; Peijnenburg, W. Silicon Nanoparticles: Characterization and Toxicity Studies. *Environ. Sci.: Nano* **2018**, *5*, 2945-2951. DOI: 10.1039/C8EN00934A

Ledoux, G.; Gong, J.; Huisken, F.; Guillois, O.; Reynaud, C. Photoluminescence of Size-Separated Silicon Nanocrystals: Confirmation of Quantum Confinement. *Appl. Phys. Lett.* **2002**, *80*, 4834. DOI: 10.1063/1.1485302

Lee, W.; Permatasari, A.; Kwon, Y. Neutral pH Aqueous Redox Flow Batteries Using an Anthraquinone-Ferrocyanide Redox Couple. *J. Mater. Chem. C* **2020**, *8*, 5727. DOI: 10.1039/d0tc00640h

Li, Y.-J.; Harroun, S. G.; Su, Y.-C.; Huang, C.-F.; Unnikrishnan, B.; Lin, H.-J.; Lin, C.-H.; Huang, C.-C. Synthesis of Self-Assembled Spermidine-Carbon Quantum Dots Effective against Multidrug-Resistant Bacteria. *Advanced Healthcare Materials* **2016**, *5* (19), 2545-2554. DOI: 10.1002/adhm.201600297

Li, Y.; Li, W.; Zhang, H.; Liu, Y.; Ma, L.; Lei, B. Amplified Light Harvesting for Enhancing Italian Lettuce Photosynthesis Using Water Soluble Silicon Quantum Dots as Artificial Antennas. *Nanoscale* **2020**, *12*, 155-166. DOI: 10.1039/C9NR08187A

Li, Z. Q.; Lu, C.J.; Xia, Z. P.; Zhou, Y.; Luo, Z. X-Ray Diffraction Patterns of Graphitic and Turbostratic Carbon. *Carbon* **2007**, *45* (8), 1686-1695. DOI: 10.1016/j.carbon.2007.03.038

Littau, K. A.; Szajowski, P. J.; Muller, A. J.; Kortan, A. R.; Brus, L. E. A Luminescent Silicon Nanocrystal Colloid via a High-Temperature Aerosol Reaction. *J. Phys. Chem.* **1993**, *97*, 1224-1230. DOI: 10.1021/j100108a019

Luckham, R. E.; Brennan, J. D. Bioactive Paper Dipstick Sensors for Acetylcholinesterase Inhibitors Based on Sol-gel/enzyme/Gold Nanoparticle Composites. *Analyst* **2010**, *135*, 2028-2035. DOI: 10.1039/C0AN00283F

Makkar, M.; Viswanatha, R. Frontier Challenges in Doping quantum Dots: Synthesis and Characterization. *RSC Adv.* **2018**, *8*, 22103-22112. DOI: 10.1039/C8RA03530J

Markwardt, M. L.; Kremers, G.-J.; Kraft, C. A.; Ray, K.; Cranfill, P. J. C.; Wilson, K. A.; Day, R. N.; Wachter, R. M.; Davidson, M. W.; Rizzo, M. A. An Improved Cerulean Fluorescent Protein with Enhanced Brightness and Reduced Reversible Photoswitching. *PLoS ONE* **2011**, *6* (3), e17896. DOI: 10.1371/journal.pone.0017896

Martindale, B. C.; Hutton, G. A. M.; Caputo, C. A.; Reisner, E. Solar Hydrogen Production Using Carbon Quantum Dots and a Molecular Nickel Catalyst. *J. Am. Chem. Soc.* **2015**, *137*, 6018-6025. DOI: 10.1021/jacs.5b01650

McVey, B. F. P.; Tilley, R. D. Solution Synthesis, Optical Properties, and Bioimaging Applications of Silicon Nanocrystals. *Acc. Chem. Res.* **2014**, *47*, 3045-3051. DOI: 10.1021/ar500215v

Meier, M. A. R.; Tam, M. K. C. Shaping Effective Practices for Incorporating Sustainability Assessment in Manuscripts Submitted to *ACS Sustainable Chemistry & Engineering: Biomaterials*. *ACS Sustainable Chem. Eng.* **2021**, *9*, 7400-7042. DOI: 10.1021/acssuschemeng.1c03382

Milligan, K.; Shand, N. C.; Graham, D.; Faulds, K. Detection of Multiple Nitroaromatic Explosives via Formation of a Janowsky Complex and SERS. *Anal. Chem.* **2020**, *92*, 3253-3261. DOI: 10.1021/acs.analchem.9b05062

Milliken, S.; Thiessen, A. N.; Cheong, I. T.; O'Connor, K. M.; Li, Z.; Hooper, R. W.; Robidillo, C. J. T.; Veinot, J. G.C. "Turning the Dials": Controlling Synthesis, Structure, Composition, and Surface Chemistry to Tailor Silicon Nanoparticle Properties. *Nanoscale* **2021**, *13*, 16379-16404. DOI: 10.1039/D1NR04701A

Mintz, K. J.; Zhou, Y.; Leblanc, R. M. Recent Developments of Carbon Quantum Dots Regarding Their Optical Properties, Photoluminescence Mechanism, and Core Structure. *Nanoscale* **2019**, *11*, 4634-4652. DOI: 10.1039/C8NR10059D

Miranda, O. R.; Li, X.; Garcia-Gonzalez, L.; Zhu, Z. J.; Bunz, U. H. F.; Rotello, V. M. Colorimetric Bacteria Sensing using a Supramolecular Enzyme-Nanoparticle Biosensor. *J. Am. Chem. Soc.* **2011**, *133* (25), 9650-9653. DOI: 10.1021/ja2021729

Mittemeijer, E. J. *Fundamentals of Materials Science: The Microstructure-Property Relationship Using Metals as Model Systems*, 2<sup>nd</sup> ed.; Springer Nature Switzerland AG; 2021.

Mocatta, D.; Cohen, G.; Schnattner, J.; Millo, O.; Rabani, E.; Banin, U. Heavily Doped Semiconductor Nanocrystal Quantum Dots. *Science* **2011**, *332*, 77-81. DOI: 10.1126/science.1196321

Montoto, E. C.; Nagarjuna, G.; Hui, J.; Burgess, M.; Sekerak, N. M.; Hernández-Burgos, K.; Wei, T.-S.; Kneer, M.; Grolman, J.; Cheng, K. J.; Lewis, J. A.; Moore, J. S. Rodríguez-López, J. Redox Active Colloids as Discrete Energy Storage Carriers. *J. Am. Chem. Soc.* **2016**, *138* (40), 13230–13237. DOI: 10.1021/jacs.6b06365

Moore, D. S. Instrumentation for Trace Detection of High Explosives. *Rev. Sci. Instrum.* **2004**, *75*, 2499-2512. DOI: 10.1063/1.1771493

Morgan, D. J. Comments on the XPS Analysis of Carbon Materials. *C* **2021**, *7*, 51. DOI: 10.3390/c7030051

Murphy, C. J. Sustainability as an Emerging Design Criterion in Nanoparticle Synthesis and Applications. *J. Mater. Chem.* **2008**, *18*, 2173-2176. DOI: 10.1039/b717456j

Obodovskiy, I. Chapter 27. Radiation-Chemical Nanotechnologies. In *Radiation: Fundamentals, Applications, Risks, and Safety*; Elsevier B. V. ; 2019.

Nöll, G.; Su, Q.; Heidel, B.; Yu, Y. A Reusable Sensor for the Label-Free Detection of Specific Oligonucleotides by Surface Plasmon Fluorescence Spectroscopy. *Adv. Healthcare Mater.* **2014**, *3*, 42-46. DOI: 10.1002/adhm.201300056

Oliva-Chatelain, B. L.; Ticich, T. M.; Barron, A. R. Doping Silicon Nanocrystals and Quantum Dots. *Nanoscale* **2016**, *8*, 1733-1745. DOI: 10.1039/C5NR04978D

Özbilgin, I. N. G.; Yamazaki, T.; Watanabe, J.; Sun, H.-T.; Hanagata, N.; Shirahata, N. Water-Soluble Silicon Quantum Dots towards Fluorescence-Guided Photothermal Nanotherapy. *Langmuir* **2022**, *38* (17), 5188-5196. DOI: 10.1021/acs.langmuir.1c02326

Pain, S. Power through the ages. *Nature* **2017**, *551*, S134-S137. DOI: 10.1038/d41586-017-07506-z

Palewska, K. ; Sworakowski, J. ; Chojnacki, H. A Photoluminescence Study in Fullerenes: Total Luminescence Spectroscopy of C<sub>60</sub> and C<sub>70</sub>. *J. Phys. Chem.* **1993**, *97*, 12167-12172. DOI: 10.1021/j100149a011

Pardo-Yissar, V.; Katz, E.; Wasserman, J.; Willner, I. Acetylcholine Esterase-Labeled CdS Nanoparticles on Electrodes: Photoelectrochemical Sensing of the Enzyme Inhibitors. *J. Am. Chem. Soc.* **2003**, *125* (3), 622-623. DOI: 10.1021/ja028922k

Quan, M.; Sanchez, D.; Wasylkiw, M. F.; Smith, D. K. Voltammetry of Quinones in Unbuffered Aqueous Solution: Reassessing the Roles of Proton Transfer and Hydrogen Bonding in the Aqueous Electrochemistry of Quinones. *J. Am. Chem. Soc.* **2007**, *129*, 12847-12856. DOI: 10.1021/ja0743083

Rigodanza, F.; Đorđević, L.; Arcudi, F.; Prato, M. Customizing the Electrochemical Properties of Carbon Nanodots by Using Quinones in Bottom-Up Synthesis. *Angew. Chem.* **2018**, *57* (18), 5062-5067. DOI: 10.1002/anie.201801707

Robidillo, C. J. T.; Wandelt, S.; Dalangin, R.; Zhang, L.; Yu, H.; Meldrum, A.; Campbell, R. E.; Veinot, J. G. C. Ratiometric Detection of Nerve Agents by Coupling Complementary Properties of Silicon-Based Quantum Dots and Green Fluorescent Protein. *ACS Appl. Mater. Interfaces* **2019**, *11*, 33478-33488. DOI: 10.1021/acsami.9b10996

Robidillo, C. J. T.; Islam, M. A.; Aghajamali, M.; Faramus, A.; Sinelnikov, R.; Zhang, X.; Boekhoven, J.; Veinot, J. G. C. Functional Bioinorganic Hybrids from Enzymes and Luminescent Silicon-Based Nanoparticles. *Langmuir* **2018**, *34*, 6556-6569. DOI: 10.1021/acs.langmuir.8b01119

Rossetti, R.; Brus, L. Electron-Hole Recombination Emission as a Probe of Surface Chemistry in Aqueous CdS Colloids. *J. Phys. Chem.* **1982**, *86*, 4470-4472. DOI: 10.1021/j100220a003

Rossetti, R.; Nakahara, S.; Brus, L. E. Quantum Size Effects in the Redox Potentials, Resonance Raman Spectra, and Electronic Spectra of CdS Crystallites in Aqueous Solution. *J. Chem. Phys.* **1983**, *79* (2), 1086-1088. DOI: 10.1063/1.445834

Rowe, D. J.; Jeong, J. S.; Mkhoyan, K. A.; Kortshagen, U. R. Phosphorous-Doped Silicon Nanocrystals Exhibiting Mid-Infrared Localized Surface Plasmon Resonance. *Nano Lett.* **2013**, *13* (3), 1317-1322. DOI: 10.1021/nl4001184

Sailor, M. J.; Wu, E. C. Photoluminescence-Based Sensing with Porous Silicon Films, Microparticles, and Nanoparticles. *Adv. Funct. Mater.* **2009**, *19*, 3195-3208. DOI: 10.1002/adfm.200900535

Sass, S. L. *The Substance of Civilization: Materials and Human History from the Stone Age to the Age of Silicon*, 1<sup>st</sup> ed.; Arcade Publishing, Inc.; 1998.

Saunders, W. A.; Sercel, P. C.; Lee, R. B.; Atwater, H. A.; Vahala, K. J.; Flagan, R. C.; Escorcia-Aparicio, E. J. Synthesis of Luminescent Silicon Clusters by Spark Ablation. *Appl. Phys. Lett.* **1993**, *63*, 1549. DOI: 10.1063/1.110745

Schneider, J.; Reckmeier, C. J.; Xiong, Y.; von Seckendorff, M.; Susha, A. S.; Kasák, P.; Rogach, A. L. Molecular Fluorescence in Citric Acid-Based Carbon Dots. *J. Phys. Chem. C* **2107**, *121* (3), 2014-2022. DOI: 10.1021/acs.jpcc.6b12519

Schubert, U.; Hüsing, N. *Synthesis of Inorganic Materials*, 2<sup>nd</sup> ed.; Wiley-VCH Verlag GmbH & Co. KGaA, Weinheim; 2005.

Siddique, A. B.; Pramanick, A. K.; Chatterjee, S.; Ray, M. Amorphous Carbon Dots and their Remarkable Ability to Detect 2,4,6-Trinitrophenol. *Scientific Reports* **2018**, *8*, 9770. DOI: 10.1038/s41598-018-28021-9

*Silicon*. <https://www.rsc.org/periodic-table/element/14/silicon> (accessed 2022-05-26)

Simonian, A. L.; Good, T. A.; Wang, S. S.; Wild, J. R. Nanoparticle-Based Optical Biosensors for the Direct Detection of Organophosphate Chemical Warfare Agents and Pesticides. *Anal. Chim. Acta* **2005**, *534* (1), 69-77. DOI: 10.1016/j.aca.2004.06.056

Singh, M. P.; Atkins, T. M.; Muthuswamy, E.; Kamali, S.; Tu, C.; Louie, A. Y.; Kauzlarich, S. M. Development of Iron-Doped Silicon Nanoparticles As Bimodal Imaging Agents. *ACS Nano* **2012**, *6*, 5596-5604. DOI: 10.1021/nm301536n

Smedskjaer, M. M.; Mauro, J. C.; Youngman, R. E.; Hogue, C. L.; Potuzak, M.; Yue, Y. Topological Principles of Borosilicate Glass Chemistry. *J. Phys. Chem. B* **2011**, *115*, 12930-12946. DOI: 10.1021/jp208796b

Soref, R. Mid-Infrared Photonics in Silicon and Germanium. *Nature Photon* **2010**, *4*, 495-497. DOI: 10.1038/nphoton.2010.171

Strehlow, W. H.; Cook, E. L. Compilation of Energy Band Gaps in Elemental and Binary Compound Semiconductors and Insulators. *J. Phys. Chem. Ref. Data* **1973**, *2*, 163. DOI: 10.1063/1.3253115

Sugimoto, H.; Zhou, H.; Takada, M.; Fushimi, J.; Fujii, M. Visible-Light Driven Photocatalytic Hydrogen Generation by Water-Soluble All-Inorganic Core-Shell Silicon Quantum Dots. *J. Mater. Chem. A* **2020**, *8*, 15789-15794. DOI: 10.1039/D0TA01071E

Tilley, R. D.; Yamamoto, K. The Microemulsion Synthesis of Hydrophobic and Hydrophilic Silicon Nanocrystals. *Adv. Mater.* **2006**, *18*, 2053–2056. DOI: 10.1002/adma.200600118

Titirici, M.-M.; White, R. J.; Brun, N.; Budarin, V. L.; Su, D. S.; del Monte, F.; Clark, J. H.; MacLachlan, M. J. Sustainable Carbon Materials. *Chem. Soc. Rev.* **2015**, *44*, 250-290. DOI: 10.1039/C4CS00232F

Tan, C.; Nasir, M. Z. M.; Ambrosi, A.; Pumera, M. 3D Printed Electrodes for Detection of Nitroaromatic Explosives and Nerve Agents. *Anal. Chem.* **2017**, *89* (17), 8995-9001. DOI: 10.1021/acs.analchem.7b01614

Tu, C.; Ma, X.; Pantazis, P.; Kauzlarich, S. M.; Louie, A. Y. Paramagnetic, Silicon Quantum Dots for Magnetic Resonance and Two-Photon Imaging of Macrophages. *J. Am. Chem. Soc.* **2010**, *132*, 2016–2023. DOI: 10.1021/ja909303g

Tiwari, J.; Tarale, P.; Sivanesan, S.; Bafana, A. Environmental Persistence, Hazard, and Mitigation Challenges of Nitroaromatic Compounds. *Environ. Sci. Pollut. Res.* **2019**, *26*, 28650-28667. DOI: 10.1007/s11356-019-06043-8

Tian, K.; Siegel, G.; Tiwari, A. Enzymatic Glucose Sensor Based on Au Nanoparticle and Plant-Like ZnO Film Modified Electrode. *Mat. Sci. Eng. C* **2015**, *46*, 548-552. DOI: 10.1016/j.msec.2014.10.064

Uhlir, A. Electrolytic Shaping of Germanium and Silicon. *Bell Syst. Tech. J.* **1956**, *35*, 333. DOI : 10.1002/j.1538-7305.1956.tb02385.x

United Nations Sustainable Development Goal 7. <https://unstats.un.org/sdgs/report/2021/goal-07/> (accessed 2021-09-21)

Valiulis, A. V. *A History of Materials and Technologies Development*; VGTU Press TECHNIKA; 2014.

Wang, H.; Sayed, S. Y.; Lubner, E. J.; Olsen, B. C.; Shirurkar, S. M.; Venkatakrishnan, S.; Tefashe, U. M.; Farquhar, A. K.; Smotkin, E. S.; McCreery, R. L.; Buriak, J. M. Redox Flow Batteries: How to Determine Electrochemical Kinetic Parameters. *ACS Nano* **2020**, *14*, 2575–2584. DOI: 10.1021/acsnano.0c01281

Wang, H.; Wan, K.; Shi, X. Recent Advances in Nanozyme Research. *Adv. Mater.* **2019**, *31*, 1805368. DOI: 10.1002/adma.201805368

Wang, J.; Zhang, P.; Huang, C.; Liu, G.; Leung, K. C.-F.; Wang, Y. X. J. High Performance Photoluminescent Carbon Dots for In Vitro and In Vivo Bioimaging: Effect of Nitrogen Doping Ratios. *Langmuir* **2015**, *31*, 8063-8073. DOI: 10.1021/acs.langmuir.5b01875

Wang, L. S.; Yan, B.; Burmaoglu, S.; Li, X.; Rotello, V. M. Sensing by Smell: Nanoparticle-Enzyme Sensors for Rapid and Sensitive Detection of Bacteria with Olfactory Output. *ACS Nano* **2017**, *11*, 5339-5343. DOI: 10.1021/acsnano.7b00822

Wareing, T. C.; Gentile, P.; Phan, A. N. Biomass-Based Carbon Dots: Current Development and Future Perspectives. *ACS Nano* **2021**, *15*, 15471-15501. DOI: 10.1021/acsnano.1c03886

Wilcoxon, J. P.; Samara, G. A.; Provencio, P. N. Optical and Electronic Properties of Si Nanoclusters Synthesized in Inverse Micelles. *Phys. Rev. B* **1999**, *60*, 2704-2714. DOI: 10.1103/PhysRevB.60.2704

Wilson, W. L.; Szajowski, P. F.; Brus, L. E. Quantum Confinement in Size-Selected, Surface-Oxidized Silicon Nanocrystals. *Science* **1993**, *262*, 1242-1244. DOI: 10.1126/science.262.5137.1242

Winsberg, J.; Hagemann, T.; Janoschka, T.; Hager, M. D.; Schubert, U. S. Redox-Flow Batteries: From Metals to Organic Redox-Active Materials. *Angew. Chem. Int. Ed.* **2017**, *56* (3), 686-711. DOI: 10.1002/anie.201604925

Wu, M.; Bahari, M.; Fell, E. M.; Gordon, R. G.; Aziz, M. J. High-Performance Anthraquinone with Potentially Low Cost for Aqueous Redox Flow Batteries. *J. Mater. Chem. A* **2021**, *9*, 26709-26716. DOI: 10.1039/D1TA08900E

Xiao, L.; Sun, H. Novel Properties and Applications of Carbon Nanodots. *Nanoscale Horiz.* **2018**, *3*, 565. DOI: 10.1039/c8nh00106e

Xie, X.; Xu, W.; Liu, X. Improving Colorimetric Assays through Protein Enzyme-Assisted Gold Nanoparticle Amplification. *Acc. Chem. Rev.* **2012**, *45* (9), 1511-1520. DOI: 10.1021/ar300044j

Xu, X.; Ma, S.; Xiao, X.; Zhao, D. The Preparation of High-Quality Water-Soluble Silicon Quantum Dots and Their Application in the Detection of Formaldehyde. *RSC Adv.* **2016**, *6*, 98899-98907. DOI: 10.1039/C6RA24654K

Xu, X.; Ray, R.; Gu, Y.; Ploehn, H. J.; Gearheart, L.; Raker, K.; Scrivens, W. A. Electrophoretic Analysis and Purification of Fluorescent Single-Walled Carbon Nanotube Fragments. *J. Am. Chem. Soc.* **2004**, *126*, 12736-12737. DOI 10.1021/ja040082

Yadav, R. M.; Li, Z.; Zhang, T.; Sahin, O.; Roy, S.; Gao, G.; Guo, H.; Vajtai, R.; Wang, L.; Ajayan, P. M.; Wu, J. Amine-Functionalized Carbon Nanodot Electrocatalysts Converting Carbon Dioxide to Methane. *Adv. Mater.* **2022**, *34*, 2105690. DOI: 10.1002/adma.202105690

Yan, F.; Jiang, Y.; Sun, X.; Bai, Z.; Zhang, Y.; Zhou, X. Surface Modification and Chemical Functionalization of Carbon Dots: A Review. *Microchimica Acta* **2018**, *185*, 424. DOI: 10.1007/s00604-018-2953-9

Yang, C.-S.; Bley, R. A.; Kauzlarich, S. M.; Lee, H. W. H.; Delgado, G. R. Synthesis of Alkyl-Terminated Silicon Nanoclusters by a Solution Route. *J. Am. Chem. Soc.* **1999**, *121* (22), 5191-5195. DOI: 10.1021/ja828509

Yuan, Y. H.; Liu, Z. X.; Li, R. S.; Zou, H. Z.; Lin, M.; Liu, H.; Huang, C. Z. Synthesis of Nitrogen-Doping Carbon Dots with Different Photoluminescence Properties by Controlling the Surface States. *Nanoscale* **2016**, *8*, 6770-6776. DOI: 10.1039/C6NR00402C

Zhang, L.; Han, Y.; Zhu, J.; Zhai, Y.; Dong, S. Simple and Sensitive Fluorescent and Electrochemical Trinitrotoluene Sensors Based on Aqueous Carbon Dots. *Anal. Chem.* **2015**, *87* (4), 2033-2036. DOI: 10.1021/ac5043686

Zhou, Y.; Liu, L. ; Shen, L.; Wu, L.; Yu, L.; Liang, F.; Xi, J. Carbon Dots Promoted Vanadium Flow Batteries for All-Climate Energy Storage. *Chem. Commun.* **2017**, *52*, 7565-7568. DOI: 10.1039/c7cc00691h

Zhou, S.; Pi, X.; Ni, Z.; Jiang, Y.; Jin, C.; Delerue, C.; Yang, D.; Nozaki, T. Comparative Study on the Localized Surface Plasmon Resonance of Boron- and Phosphorous-Doped Silicon Nanocrystals. *ACS Nano* **2015**, *9* (1), 378-386. DOI: 10.1021/nn505416r

Zhou, Y.; Mintz, K. J.; Sharma, S. K.; Leblanc, R. M. Carbon Dots: Diverse Preparation, Application, and Perspective in Surface Chemistry. *Langmuir* **2019**, *35*, 9115-9132. DOI: 10.1021/acs.langmuir.9b00595